

# Recurrent Rossby waves: drivers and links to persistent weather

Inaugural dissertation  
of the Faculty of Science,  
University of Bern

presented by  
**Syed Mubashshir Ali**  
from India

Supervisor of the doctoral thesis:  
Prof. Dr. Olivia Romppainen-Martius  
Institute of Geography, University of Bern

Co-supervisors of the doctoral thesis:  
Prof. Dr. John Methven  
Department of Meteorology, University of Reading  
Dr. Matthias Röthlisberger  
Institute for Atmospheric and Climate Science, ETH Zürich





# Recurrent Rossby waves: drivers and links to persistent weather

Inaugural dissertation  
of the Faculty of Science,  
University of Bern

presented by  
**Syed Mubashshir Ali**  
from India

Supervisor of the doctoral thesis:  
Prof. Dr. Olivia Romppainen-Martius  
Institute of Geography, University of Bern

Co-supervisors of the doctoral thesis:  
Prof. Dr. John Methven  
Department of Meteorology, University of Reading  
Dr. Matthias Röthlisberger  
Institute for Atmospheric and Climate Science, ETH Zürich

Accepted by the Faculty of Science.

Bern, 01 September 2022

The Dean:  
Prof. Dr. Marco Herwegh



**Supervisors and advisors:**

**Prof. Dr. Olivia Romppainen-Martius**

Institute of Geography

University of Bern

**Prof. Dr. John Methven**

Department of Meteorology

University of Reading

**Dr. Matthias Röthlisberger**

Institute for Atmospheric and Climate Science

ETH Zürich

**External examiner:**

**Asst. Prof. Dr. Rachel H. White**

Department of Earth, Ocean and Atmospheric Sciences

University of British Columbia, Vancouver



This work is licensed under a Creative Commons Attribution 4.0 International License  
<https://creativecommons.org/licenses/by/4.0/>



## Abstract

Upper-level Rossby wave packets (RWPs) are one of the key drivers of surface weather. RWPs can lead to extreme surface weather events. However, extreme impacts can also arise from long spells of persistent weather. Recurrence of synoptic-scale RWPs, termed RRWPs, where RWPs recur in the same phase over a short period, can also lead to persistent weather. The importance of RRWPs has only been identified recently. This thesis aims to explore the role of RRWPs in modulating persistent weather events and discover the atmospheric processes driving RRWPs.

First, the thesis quantifies the significance of RRWPs for dry and wet spells across the globe. Persistent dry spells can lead to droughts, make heatwaves more extreme, and increase the risk of forest fires. The thesis finds that RRWPs are significantly associated with longer dry and wet spells across the globe. The case studies further demonstrate the role of RRWPs during episodes of dry and wet spells, respectively.

Next, the thesis explores the role of RRWPs for hot spells in the SH. For the hot spells, RRWPs are significantly associated with longer hot spells over several regions, including south-eastern Australia (SEA), a region that has seen increasingly extreme heatwaves in recent decades. Motivated by that, the importance of RRWPs for the set of most persistent and extreme SEA heatwaves is explored further. The role of RRWPs during SEA heatwaves is demonstrated by two case studies of 2004 and 2009 SEA heatwaves, where RRWPs help to build recurrent ridges over SEA. Furthermore, days with RRWP conditions over SEA are associated with an increased probability of SEA heatwaves.

Given the vital role of RRWPs for SEA heatwaves, the thesis sets out to find the association of RRWPs with other atmospheric drivers of persistent weather, namely, atmospheric blocks and quasi-resonance amplification (QRA). QRA conditions were also detected during some episodes of the most persistent and extreme SEA heatwaves. We find that RRWPs and QRA are closely associated in the SH, with 40% of QRA days also featuring RRWP conditions. We study their close association with upper-level composite maps and discuss the similarities and differences in the algorithm used to identify them. For the link of RRWPs and QRA with blocks in SH, we find an insignificant increase in the median area of blocks for days with RRWP than without and a slight decrease for QRA days than non-QRA days. We also find substantial differences in the spatial distribution of blocks between QRA days and RRWP days.

Motivated by the vital role of the RRWPs, the latter part of this thesis investigates the causal drivers of RRWPs in the North Atlantic for the winter and summer seasons. RRWP episodes for summer and winter are used to identify possible causal drivers of RRWPs, whose relevance is subsequently examined in a causal network (CN) framework. The CNs reveal that local changes over the Atlantic in atmospheric blocking and low wavenumber background flow primarily drive

RRWPs for both seasons. RRWPs also have feedback on background flow and blocks. In winter, tropical forcing has an indirect link with RRWPs, which drives background flow changes over the Pacific, and subsequently modifies background flow over the Atlantic. In summer, a direct link from background flow over the Pacific to RRWPs exists. CNs also reveal a robust link from extratropics to tropics in the summer, where background flow over North Atlantic drives changes in the background flow over the Pacific.

# Contents

<b>Abstract</b>	<b>i</b>
<b>Contents</b>	<b>iii</b>
<b>List of Figures</b>	<b>vii</b>
<b>List of Tables</b>	<b>ix</b>
<b>1 Introduction</b>	<b>1</b>
1.1 Motivation . . . . .	1
1.2 Aims and Outline . . . . .	4
<b>2 Recurrent Rossby wave packets modulate the persistence of dry and wet spells across the globe</b>	<b>7</b>
2.1 Key Points . . . . .	7
2.2 Abstract . . . . .	7
2.3 Introduction . . . . .	8
2.4 Data and Method . . . . .	9
2.5 Results . . . . .	12
2.5.1 Examples of persistent wet and dry spells during RRWPs . . . . .	12
2.5.2 Rossby wave recurrence associated with dry spells . . . . .	12
2.5.3 Rossby wave recurrence associated with wet spells . . . . .	13
2.6 Discussion . . . . .	19
2.7 Conclusion . . . . .	20
2.8 Acknowledgments and Data availability . . . . .	21
<b>3 Recurrent Rossby waves and South-eastern Australian heatwaves</b>	<b>23</b>
3.1 Abstract . . . . .	23
3.2 Introduction . . . . .	24
3.3 Methods . . . . .	26
3.3.1 Data . . . . .	26
3.3.2 Recurrent Rossby waves . . . . .	26
3.3.3 Atmospheric Blocks . . . . .	27

3.3.4	South-eastern Australian heatwaves . . . . .	27
3.3.5	Hot spells in the SH . . . . .	28
3.3.6	Weibull regression model to assess the effect of RRWPs in the SH hot spells . . . . .	29
3.4	Results . . . . .	30
3.4.1	RRWPs and hot spell durations . . . . .	30
3.4.2	RRWPs and Blocks during two extreme and persistent SEA heatwaves . . . . .	31
3.4.3	RRWP conditions during SEA heatwave . . . . .	33
3.5	Discussion . . . . .	41
3.6	Conclusion . . . . .	42
3.7	Acknowledgments and data availability . . . . .	43
<b>4</b>	<b>Association between RRWPs, QRA, and blocks in the Southern Hemisphere</b>	<b>45</b>
4.1	Introduction . . . . .	46
4.2	Method . . . . .	47
4.3	Data . . . . .	47
4.3.1	QRA data . . . . .	48
4.4	Results . . . . .	48
4.4.1	Are RRWPs and QRA events independent? . . . . .	48
4.4.2	How similar or different are upper-level flow conditions during RRWPs vs QRA days? . . . . .	49
4.4.3	Does blocking area increase during high $R$ or QRA conditions? . . . . .	51
4.4.4	How are blocks spatially distributed for high $R$ and QRA days? . . . . .	52
4.5	Discussion . . . . .	53
4.6	Conclusions and Outlook . . . . .	55
<b>5</b>	<b>Drivers of Recurrent Rossby Waves in the North Atlantic using Causal Networks</b>	<b>57</b>
5.1	Introduction . . . . .	57
5.2	Method . . . . .	59
5.2.1	Dataset . . . . .	59
5.2.2	Selecting high $R$ events . . . . .	61
5.2.3	Causal Networks . . . . .	61
5.3	Results . . . . .	64
5.3.1	Example high $R$ event: January 2018 . . . . .	64
5.3.2	Example high $R$ event: June 2003 . . . . .	67
5.3.3	North Atlantic DJF . . . . .	68
5.3.4	North Atlantic JJA . . . . .	71
5.4	Discussion . . . . .	83
5.5	Conclusions . . . . .	84
5.6	Acknowledgments . . . . .	85



<b>6</b>	<b>Conclusions and Outlook</b>	<b>87</b>
6.1	Summary and conclusions . . . . .	87
6.2	Outlook . . . . .	89
	<b>Bibliography</b>	<b>91</b>
<b>A</b>	<b>Supporting Information for Recurrent Rossby wave packets modulate the persistence of dry and wet spells across the globe</b>	<b>105</b>
A.1	Spell count and median for Dry Spells and Wet Spells . . . . .	105
A.2	Additional examples of RRWPs and persistent dry and wet spells . . . . .	110
A.2.1	A dry spell in North America . . . . .	110
A.2.2	A wet spell in South America . . . . .	111
<b>B</b>	<b>Supporting Information for Recurrent Rossby waves and South-eastern Australian heatwaves</b>	<b>115</b>
B.1	Comparison of $R$ anomalies for Southern Hemisphere and Northern Hemisphere . .	115
B.2	Co-occurrence of High $R_{SEA}$ on SEA heatwave days . . . . .	116
B.3	RRWPs during 2014 Heatwaves . . . . .	117
B.4	Relationship between blocks and RRWPs in the south Pacific and the Indian Ocean	118
<b>C</b>	<b>Additional Information for drivers of Recurrent Rossby Waves in the North Atlantic using Causal Networks</b>	<b>121</b>
C.1	Model Output DJF . . . . .	121
C.2	Model Output JJA . . . . .	123
C.3	Sensitivity tests for DJF . . . . .	123
C.4	Sensitivity tests for JJA . . . . .	125
<b>D</b>	<b>A novel method to identify sub-seasonal clustering episodes of extreme precipitation events and their contributions to large accumulation periods</b>	<b>127</b>
D.1	Abstract . . . . .	128
<b>E</b>	<b>Large-scale drivers of persistent extreme weather during early summer 2021 in Europe</b>	<b>129</b>
E.1	Abstract . . . . .	130
<b>F</b>	<b>On the temporal clustering of European extreme precipitation events and its relationship to persistent and transient large-scale atmospheric drivers</b>	<b>131</b>
F.1	Abstract . . . . .	132



# List of Figures

1.1	The metric $R$ . . . . .	2
1.2	Theme of the thesis . . . . .	4
2.1	Computation steps for the metric $R$ . . . . .	10
2.2	An example wet spell over Iberia in 1983 . . . . .	14
2.3	An example dry spell over Brazil in 1985 . . . . .	15
2.4	PV composite for wet and dry spells . . . . .	16
2.5	Statistically significant acceleration factors for (a) MJJASO and (b) NDJFMA dry spells. . . . .	17
2.6	Statistically significant acceleration factors for (a) MJJASO and (b) NDJFMA wet spells. . . . .	18
3.1	Map of Australia showing the states of South-eastern Australia (SEA) . . . . .	25
3.2	Total number of SH hot spells . . . . .	28
3.3	Significant acceleration factors for SH hot spells . . . . .	30
3.4	RRWPs, and blocks during 2004 SEA heatwave . . . . .	35
3.5	PV composite for 2004 SEA heatwave . . . . .	36
3.6	RRWPs, and blocks during 2009 SEA heatwave . . . . .	37
3.7	Same as in Fig. 3.5 except for 2009 SEA heatwave. . . . .	38
3.8	PV anomalies for High $R_{SEA}$ days and SEA heatwave days . . . . .	39
3.9	Wavenumber distribution for high $R_{SEA}$ and SEA HD and high $R_{SEA}$ and non-SEA HD . . . . .	40
4.1	Links between QRA conditions, blocking, and RRWPs with heatwaves. . . . .	47
4.2	Links between QRA conditions, blocking, and RRWPs with heatwaves. . . . .	50
4.3	Area of blocks for high $R$ and QRA days . . . . .	51
4.4	Blocking frequencies for QRA and high $R$ days . . . . .	52
5.1	Illustration of the time series used for the CNs . . . . .	63
5.2	Two example high $R$ events . . . . .	64
5.3	BU and blocks for the high $R$ event in winter 2018 . . . . .	65
5.4	Rossby wave sources for the 2018 high $R$ event . . . . .	66
5.5	BU and blocks for the high $R$ event in June 2003 . . . . .	67

5.6	Composite maps prior to winter high $R$ events . . . . .	74
5.7	Composites maps after the onset winter high $R$ events . . . . .	75
5.8	Rossby wave sources prior to winter high $R$ events . . . . .	76
5.9	Areas used to select actors for the winter CNs . . . . .	77
5.10	Drivers of RRWPs over the North Atlantic for DJF . . . . .	78
5.11	Composite maps prior to summer high $R$ events . . . . .	79
5.12	Composite maps after the onset of summer high $R$ events . . . . .	80
5.13	Area used to select actors for the summer CNs . . . . .	81
5.14	Drivers of RRWPs over the North Atlantic for JJA . . . . .	82
A.1	Dry spell count for MJJASO and NDJFMA . . . . .	106
A.2	Median MJJASO and NDJFMA dry spell length . . . . .	107
A.3	Wet spell count for MJJASO and NDJFMA . . . . .	108
A.4	Median MJJASO and NDJFMA dry spell length . . . . .	109
A.5	Dry spell over Canada and Northern US in 1990 . . . . .	110
A.6	PV composite for the 1990 dry spell over Canada and Northern US . . . . .	111
A.7	Wet spell over Brazil in 2005 . . . . .	112
A.8	PV composite for the 1990 dry spell over Brazil . . . . .	113
B.1	$R$ anomalies for Southern and Northern hemispheres . . . . .	116
B.2	January 2014 SEA heatwave . . . . .	118
B.3	RRWPs and blocks in the south Pacific and the Indian Ocean . . . . .	119

# List of Tables

4.1	Contingency table for high $R$ and QRA events in DJF . . . . .	49
4.2	Comparison of blocks, RRWPs, and QRA identification schemes . . . . .	53
5.1	Summary of the one dimensional time series used in the CN for DJF. . . . .	70
5.2	Variables used in the CN for JJA . . . . .	73
B.1	Conditional probablity for SEA heatwaves . . . . .	117
C.1	Drivers of R-NAt from the main model (k=1) for DJF . . . . .	124
C.2	Drivers of R-NAt from the model k=0 for DJF . . . . .	124
C.3	Drivers of R-NAt from the model k=1 for DJF . . . . .	124
C.4	Drivers of R-NAt from the main model (k=1) for JJA . . . . .	125
C.5	Drivers of R-NAt from the model k=0 for JJA . . . . .	125
C.6	Drivers of R-NAt from the model k=2 for JJA . . . . .	125



# Chapter 1

## Introduction

### 1.1 Motivation

Severe impacts can not only occur from extreme weather events but also less-than-extreme but persistent periods of anomalous weather, termed persistent weather (Handmer et al., 2012). Persistent weather can intensify droughts, forest fires, and floods, and have cascading impacts on increase in mortality, agriculture and food security, increase in electricity demand, and increased insurance losses. Therefore, understanding atmospheric drivers behind persistent weather is essential to improve their prediction and estimate how these events will change with climate change.

In the past, stationary upper-level anticyclones have been identified as an essential driver of persistent weather (e.g., Barriopedro et al., 2011; Drouard and Woollings, 2018; Kautz et al., 2022). However, propagating synoptic-scale Rossby wave packets, repeating in the same phase over a short period, have been observed during several persistent weather events in the Northern Hemisphere (NH) mid-latitudes (Davies, 2015; Hoskins and Sardeshmukh, 1987; Fragkoulidis et al., 2018; Barton et al., 2016). Röthlisberger et al. (2019) identified such propagating Rossby wave packets and termed them Recurrent Rossby wave packets (RRWPs).

To study the association of RRWPs with persistent hot spells in the NH, Röthlisberger et al. (2019) developed a metric  $R$  to quantify RRWPs. The metric  $R$  quantifies the strength of RRWPs by extracting the envelope of the synoptic-scale wavenumbers ( $k=4-15$ ) recurring in a short period. As shown in Figure 1.1,  $R$  attains high values when synoptic-scale Rossby waves amplify and recur in the same phase on a weekly scale. Subsequently, using  $R$  as a measure of RRWP strength, Röthlisberger et al. (2019) showed that RRWPs significantly increase the duration of hot spells over several regions in the NH, thus, leading to persistent weather.

Barton et al. (2016) showed that RRWPs were associated with several episodes of temporal clustering of extreme precipitation events over southern Switzerland. Such events could cause large-scale flood events. Similarly, long periods of dry spells can lead to droughts and impact agriculture. They can also increase the risk of forest fires. Therefore, it is crucial to identify

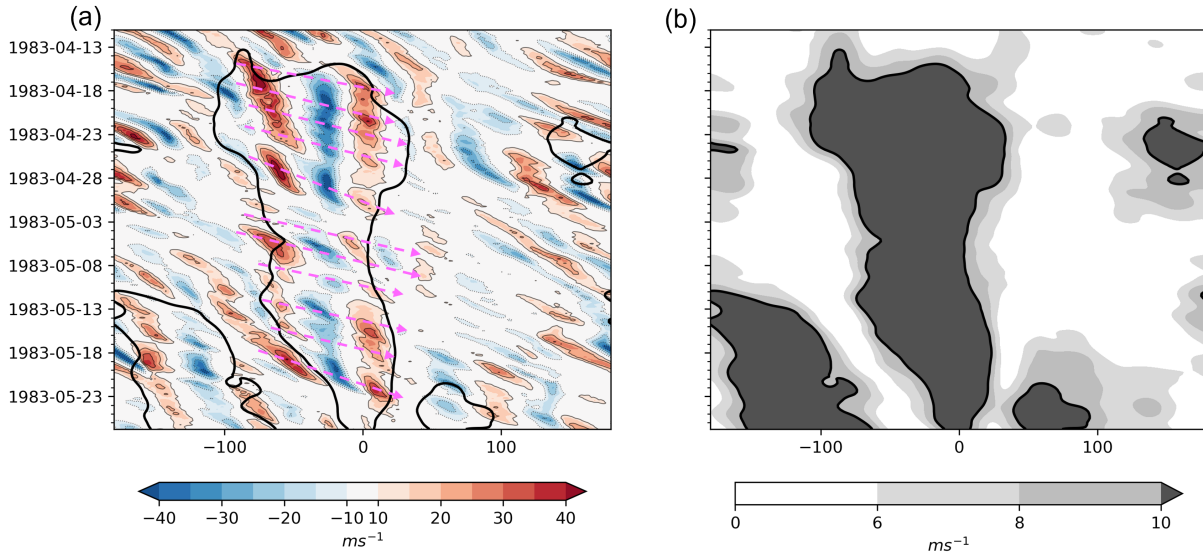


Figure 1.1: The metric  $R$  for the 1983 event discussed in Chapter 2. All panels show longitude vs time Hovmöller diagrams. (a) shows meridional wind at 250 hPa,  $V_{250}$  averaged between  $35^\circ$  and  $65^\circ$  N, (b) the metric  $R$  in  $\text{ms}^{-1}$ . Black contours in the panels show  $R = 10 \text{ ms}^{-1}$ . Dashed arrows show approximate longitude-time propagation of the respective Rossby wave packets comprising the RRWP.

whether RRWPs can be an essential atmospheric driver for dry and wet spells.

Given the significance of RRWPs for hot spells in the NH, one may ponder if RRWPs are also observed in the Southern Hemisphere (SH), or is it a feature unique to the NH due to the difference in orography and stationary forcing between the two hemispheres? If RRWPs are observed in the SH, then it is vital to investigate if they can be an essential driver of persistent hot spells in the SH.

Furthermore, several studies have reported amplified quasi-stationary patterns in the upper-level meridional winds during recent NH mid-latitude heatwaves (Wolf et al., 2018). These patterns are diagnosed by taking bi-weekly to monthly mean of meridional winds. Therefore, they can arise by Rossby waves having low phase speeds or fast propagating Rossby waves recurring in the same phase, i.e., RRWPs. RRWPs were observed during several episodes of NH heatwaves displaying a quasi-stationary pattern, e.g., the 2010 Russian heatwave (Fragkoulidis et al., 2018).

Quasi-Resonant Amplification (QRA) has been proposed as another mechanism that can produce amplified quasi-stationary waves (Petoukhov et al., 2013). QRA conditions arise in the presence of a meridional waveguide and suitable thermal and orographic forcings. QRA hypothesis suggests that during suitable conditions identified in (Petoukhov et al., 2013) and discussed in detail in Kornhuber et al. (2017b), synoptic-scale waves are trapped in the waveguide and interact with stationary waves to produce non-linear wave amplification (Petoukhov et al., 2013; Kornhuber et al., 2017a,b). QRA conditions have been diagnosed for several recent heatwave events: the



Russian heatwave of 2010 (Petoukhov et al., 2013), and the heatwaves of summer 2018 in the NH midlatitudes (Kornhuber et al., 2019). Furthermore, QRA periods during several heatwaves were composed of RRWPs, such as the European heatwave in 1994 and the Russian heatwave in 2010 (Fragkoulidis et al., 2018; Röthlisberger et al., 2019). The three drivers of persistent weather, QRA, blocks, and RRWPs, have been studied in isolation so far. Hence, it is of interest to study the association between the three. The climatological frequency of co-occurrence of QRA and RRWPs is unknown, as are the potential interactions between the two.

The findings of the association of RRWPs with persistent weather and the numerous case studies in the thesis establish the importance of the RRWPs for persistent high-impact weather. Hence, the remainder of the thesis is focused on finding the meteorological drivers of RRWPs. Understanding the drivers of RRWPs will also help to better understand how atmospheric flow will change with climate change.

RRWPs require mechanisms that influence both the formation of the waves and their phases. Transient Rossby waves may be triggered by mid-latitude diabatic heating (e.g., Grams et al., 2011; Röthlisberger et al., 2018) or active tropical convection (e.g., Davies, 2015), and subsequently amplified by baroclinic instability (Charney, 1947; Pierrehumbert and Swanson, 1995). Several model and observational studies have shown tropical and mid-latitude teleconnections whereby active tropical convection can act as a Rossby wave source (e.g., Sardeshmukh and Hoskins, 1988; Hoskins and Ambrizzi, 1993; Trenberth et al., 1998; Stan et al., 2017). In the presence of a strong and narrow jet, the resulting Rossby waves are ducted into the jet waveguide and propagate downstream along the jet. Several studies have suggested this teleconnection to be a precursor to North Atlantic weather regimes (e.g., Cassou, 2008; Lin et al., 2009; Straus et al., 2015; Davies, 2015; Stan et al., 2017; Fromang and Rivière, 2020). Active tropical convection can also influence non-linear Rossby wave dynamics in the Pacific with effects downstream over the Atlantic. Furthermore, recurving tropical cyclones undergoing an extratropical transition have been linked to Rossby wave amplification downstream (Quinting and Jones, 2016; Riboldi et al., 2019) and have shown to initiate Rossby waves in case studies (Barton et al., 2016).

RRWPs may have close associations with atmospheric blocks and background flow. Blocks can modulate the phase of Rossby waves and may also initiate Rossby waves downstream (Altenhoff et al., 2008). Feedback may also exist between RRWPs and blocks. RRWPs are composed of transient eddies, which can sustain blocks (e.g., Shutts, 1983; Hoskins and Sardeshmukh, 1987). Furthermore, blocking onset can be forced by transient eddies (e.g., Ma and San Liang, 2017). Background flow may modulate wave propagation, and the meridional displacement of isentropic Potential Vorticity contours may be larger in a weaker zonal flow (Hoskins and Woollings, 2015).

With the possible drivers of RRWPs motivated above, a combination of theory and recent advancements in data-driven tools are used to identify the drivers. Graph-based Bayesian networks are used to test the causality. Such networks output the relevant drivers as a graph-based causal

network (CN) (Pearl, 2009). Several studies have vouched for the use of causal networks in atmospheric sciences as they can help to remove spurious conclusions of association between two variables based on correlation analysis (Runge et al., 2019a; Barnes et al., 2019; Kretschmer et al., 2021). Spurious links can arise: when the two variables are highly auto-correlated, when a common driver is driving the two variables, when the link is indirect and mediated through an intermediate driver (see Fig. 1 Kretschmer et al., 2016). CNs based on conditional independence tests offer to address such spurious links (Pearl, 2009). However, in a system driven by physics, care should be taken while using purely data-driven approaches (Saggioro and Shepherd, 2019). Therefore, a theory-guided approach is adopted to supplement the CNs as in other works (e.g., Di Capua et al., 2020).

## 1.2 Aims and Outline

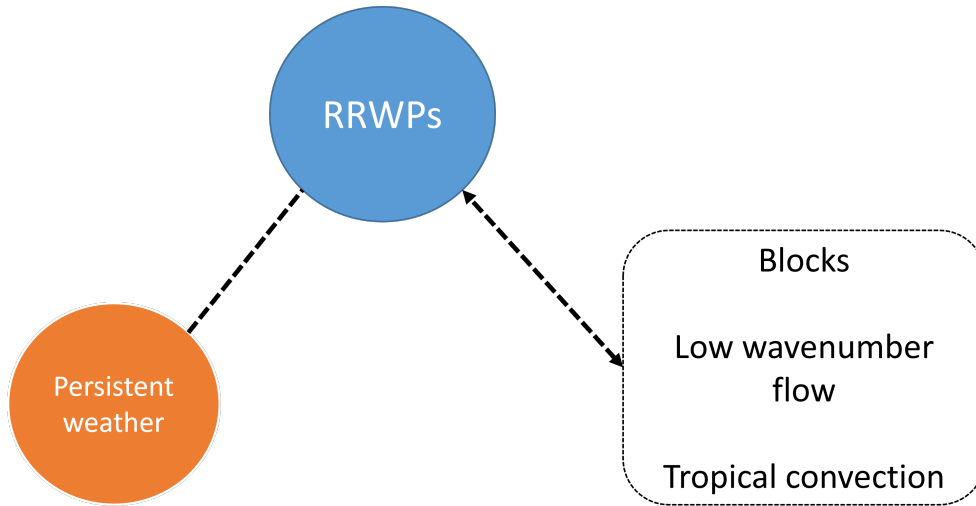


*Figure 1.2: Figure shows theme of this thesis. The box shows potential drivers of RRWPs investigated here. The dashed lines show unexplored links.*

Figure 1.2 illustrates the theme of this thesis, where the dashed arrows show the unknown links. The first part of the thesis explores the importance of RRWPs in driving persistent weather on a climatological scale. The second part of the thesis aims to find out the processes driving RRWPs.

Chapter 2 explores the association of RRWPs with dry and wet spells on a climatological scale. It demonstrates the significance of RRWPs in increasing the persistence of dry and wet spells for both NH and SH. The chapter supports the statistical analysis by presenting case studies demonstrating the key role played by RRWPs for persistent dry and wet spells.

Chapter 3 explores the role of RRWPs for the SH hot spells. Furthermore, it evaluates the importance of RRWPs for the most extreme and persistent heatwaves in south-eastern Australia

(SEA). It shows two case studies of SEA heatwaves demonstrating the role of RRWPs in building up recurrent upper-level ridges over SEA.

Chapter 4 studies the association of RRWPs with other atmospheric drivers of persistent weather, namely, atmospheric blocks and quasi-resonance amplification (QRA). QRA has been suggested as one of the mechanisms that could drive spatially-concurrent blocking episodes. Furthermore, QRA conditions were also detected during some episodes of the most persistent and extreme SEA heatwaves. Therefore, Chapter 4 aims to study the co-occurrence between the three atmospheric features: RRWPs, blocks, and QRA in the SH.

In the last part of the thesis, I aim to discover the drivers of RRWPs. Chapter 5 finds the causal drivers of RRWPs over the North Atlantic during winter and summer. A set of top RRWP events over the Atlantic show the synoptic features before the RRWP events in winter and summer. Furthermore, the chapter discusses the similarities and differences between the winter and summer RRWP events and the implications of the findings of the CNs.



## Chapter 2

# Recurrent Rossby wave packets modulate the persistence of dry and wet spells across the globe

The following chapter was published in the journal *Geophysical Research Letters* titled as "Recurrent Rossby wave packets modulate the persistence of dry and wet spells across the globe" (Ali et al., 2021). The manuscript is co-authored with Olivia Martius and Matthias Röthlisberger.

### 2.1 Key Points

1. Recurrent Rossby wave packets significantly alter (lengthen or shorten) the persistence of both wet and dry spells in the extratropics.
2. They lengthen or shorten dry (wet) spells through the recurrent formation of ridges (troughs) in the same area.
3. Recurrence of transient Rossby waves should be considered as a key dynamical mechanism for fostering persistent surface weather.

### 2.2 Abstract

Persistent dry and wet spells can arise from stationary weather situations or recurrent flow patterns and result in significant socio-economic impacts. Here, we study the effects of recurrent synoptic-scale transient Rossby wave packets (RRWPs) on the persistence of dry and wet spells using the ERA-Interim reanalysis data.

RRWPs significantly alter (decrease and increase) dry and wet spell persistence across the globe. Spatial patterns of statistically significant links between RRWPs and spell durations arise from the superposition of a zonally symmetric component and a wave-like component that is modulated by local factors such as orography and the position relative to major moisture sources.

The zonally symmetric component is apparent during the Northern Hemisphere winter and dominates the Southern Hemisphere signal in winter and summer. The wave-like component appears primarily in the Northern Hemisphere, changes its wavenumber with the season and is thus, conceivably related to stationary wave dynamics.

## 2.3 Introduction

Persistent extreme surface weather events pose a threat to food security, health, livelihood, and property (Kornhuber et al., 2020; Raymond et al., 2020; Rudd et al., 2020; Sivakumar, 2020). Persistent dry conditions can lead to droughts and exacerbate wildfires, whereas persistent wet conditions can lead to flooding. On multi-day to sub-seasonal timescales, persistent conditions may offer windows of high predictability but remain challenging for numerical weather forecast models (Ferranti et al., 2015; Matsueda and Palmer, 2018). Therefore, fundamental process understanding is essential for improving forecasts of such events (Quandt et al., 2017; Webster et al., 2011), and to reduce uncertainties in the future climate projections.

Persistent dry and wet spells are often related to slow-moving or stationary weather systems. Quasi-stationary blocking anticyclones (e.g., Rex, 1950; Pelly and Hoskins, 2003), are associated with subsidence, and thus, they often exhibit clear-sky conditions in their central and downstream part. Subsidence and increased shortwave radiation at the surface leads to hot and dry surface anomalies (e.g., Li et al., 2020; Pfahl and Wernli, 2012; Xu et al., 2020; Zschenderlein et al., 2020; Quinting et al., 2018). The persistence of the blocking anticyclones can then result in long-lasting heatwaves and persistent dry spells (Fang and Lu, 2020; Röthlisberger and Martius, 2019). Persistent wet spells can arise as a result of slow-moving and stalling tropical and extratropical cyclones (e.g., Risser and Wehner, 2017; Rhodes, 2017), persistent monsoon circulation patterns (e.g., Fang et al., 2012), stationary cut-off lows (e.g., Lenggenhager et al., 2019), and as a result of an eastward extension of the jet over the Atlantic (e.g., Blackburn et al., 2008; Schaller et al., 2016). Quasi-stationary waves, in particular those spanning an entire hemisphere, can also be associated with both persistent dry and wet spells around the globe (Coumou et al., 2014; Kornhuber et al., 2017b; Stadtherr et al., 2016; Wolf et al., 2018). However, besides stationary drivers, a number of studies have identified recurrent (rather than stationary) large-scale circulation as a cause for persistent surface weather (e.g., Drouard and Woollings, 2018; Michelangeli et al., 1995).

Recurrence of transient weather systems in the same area on sub-seasonal timescales can be associated with persistent extreme surface temperature conditions. A statistically significant link exists between recurrent Rossby wave packets (RRWPs) and the persistence of winter-cold and summer-hot spells over large areas in the Northern Hemisphere midlatitudes (Röthlisberger et al., 2019). Such RRWP events are characterized by the repeated passage of transient synoptic-scale Rossby wave packets in the same phase at the same longitude. Both recurrent ridging or troughing due to RRWPs can result in persistent hot and cold spells (Röthlisberger et al., 2019). A

few notable examples of RRWPs inducing persistent surface weather are the 1994 Central European heat wave (Röthlisberger et al., 2019), the anomalous Northern Hemisphere 2013-14 winter (Davies, 2015; Wolter et al., 2015), and flooding in the Southern Alpine region in fall 1993 (Barton et al., 2016).

Röthlisberger et al. (2019) quantified the climatological effect of RRWPs on the duration of temperature spells in the Northern Hemisphere, while the other studies cited above present case study-based evidence for a link between RRWPs and persistent wet and dry spells. However, a systematic and global evaluation of the effect of RRWPs on the persistence of dry and wet spells is so far missing. The purpose of this paper is twofold: Firstly, we aim to identify regions where the persistence of these spell types is significantly altered by RRWPs. Secondly, we discuss the physical processes linking the upper-level RRWPs to persistent wet and dry surface conditions based on example cases.

## 2.4 Data and Method

This study uses ERA-Interim (ERA-I) reanalysis data (Dee et al., 2011) on a  $1^\circ$  by  $1^\circ$  spatial resolution for the period 1980–2016. Atmospheric fields are used at 6-hourly temporal resolution. Atmospheric blocking is identified based on upper-level negative potential vorticity (PV) anomalies as in Schwierz et al. (2004), but with slight modifications (Rohrer et al., 2018).

Daily aggregated precipitation data is used for the identification of dry and wet spells at each grid point. Days with accumulations below (exceeding) 1 mm are classified as dry (wet) days. Spells separated by a one-day gap are merged into one continuous spell. From the resulting sets of dry and wet spells, all spells lasting less than 5 days are discarded, as we motivate our study from an impacts point of view. This procedure results in a set of  $n_g$  spells at each grid point  $g$ , each with durations  $D_{g,1}, \dots, D_{g,n_g}$  (Figures A.1 and A.3). We assess the effect of RRWPs on dry (wet) spell durations in both the hemispheres, separately for extended summer (May–October, MJJASO) and extended winter (November–April, NDJFMA), using a Weibull regression model following Röthlisberger et al. (2019). The notation used here is consistent with theirs

The metric  $R$  is a simple measure of RRWP strength derived from Hovmöller (time-longitude) diagrams of instantaneous meridionally averaged ( $35^\circ$  N and  $65^\circ$  N) meridional wind at 250 hPa ( $v_{250}$ ). The R-metric is in essence the envelope of a time (two week running mean) and wavenumber (WN) filtered (WN=4 to WN=15)  $v_{250}$  field (Röthlisberger et al., 2019).

Figure 2.1 illustrates the steps to compute  $R$ . To calculate, first the two-dimensional meridional wind fields are averaged between  $35^\circ$  and  $65^\circ$  N at each time step,  $v_{ma}(\lambda, t)$ . Then, 14.25 day running-mean fields are computed,  $v_{tf}(\lambda, t)$  to smooth out high-frequency transients. Next,  $v_{tf}(\lambda, t)$  is transformed into the frequency domain using a fast Fourier transform over longitude,  $\hat{v}_{tf}(k, t)$ . Finally, an inverse Fourier transform is applied to calculate the envelope of only the

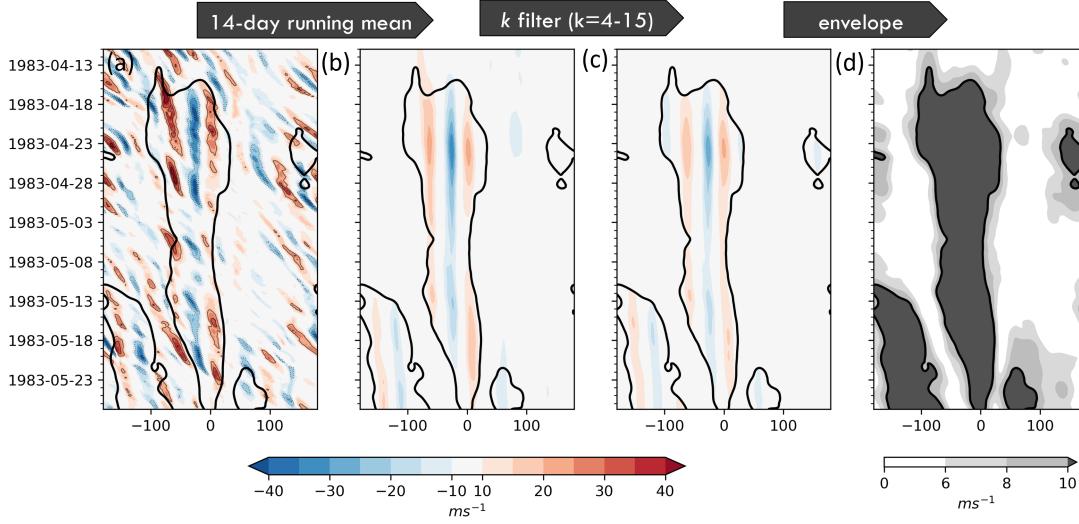


Figure 2.1: Computation steps for the metric  $R$  for the 1983 event. All panels show longitude vs time Hovmöller diagrams. (a) shows meridional wind at 250 hPa,  $v_{250}$  averaged between  $35^\circ$  and  $65^\circ$  N,  $v_{ma}(\lambda, t)$ , (b)  $v_{tf}(\lambda, t)$ , (c)  $v_{tf,wnf}(\lambda, t)$ , and (d)  $R(\lambda, t)$ . Black contours in the panels show  $R = 10 \text{ ms}^{-1}$ .

synoptic scale wavenumbers ( $k = 4\text{--}15$ ),  $v_{tf,wnf}(\lambda, t)$ . Thus,  $R(\lambda, t)$  for each longitude  $\lambda$  and time  $t$  is calculated as:

$$R(l, t) = |2 \sum_{k=4}^{15} \hat{v}_{tf}(k, t) e^{2\pi i k l / N}|, \quad (2.1)$$

We have computed this metric also for the Southern Hemisphere from meridionally averaged ( $35^\circ$  S and  $65^\circ$  S)  $v_{250}$ . We used the respective  $R$  as a covariate in a Weibull regression model fitted separately to dry and wet spell durations at each grid point poleward of  $20^\circ$  N and  $20^\circ$  S, respectively. Only grid-points that have at least 40 spells in the respective season during 1980–2016 are considered.

The Weibull model is more complex compared to the standard Gaussian linear model but, it allows us to assess changes in all quantiles of the modelled spell duration distribution per unit increase in each covariate (Supplementary Material Röthlisberger et al., 2019). Thus, it is possible to assess the effect of RRWPs via the covariate on the entire distribution of spell durations. While the statistical analysis can reveal covariability between and the spell durations, the causality in our statistical arguments is based on the case studies cited above and shown later here and in the Supplementary Material.

The Weibull model is fitted at each grid point and is only briefly introduced here for an arbitrary grid point  $g$ . First, a representative value of  $R \tilde{R}_{lon}(\lambda_g, i)$  is assigned to each spell  $i$  occurring at this grid point (with longitude  $\lambda_g$ ), which quantifies how recurrent the synoptic scale waves are in



the  $60^\circ$  longitudinal sector centred on  $\lambda_g$  during the lifetime of a spell  $i$  (Eq. 1). To calculate the  $\tilde{R}_{lon}(\lambda_g, i)$ , the raw R-metric, which is a function of longitude and time, is longitudinally averaged within the  $60^\circ$  longitudinal sector centred on  $\lambda_g$  for each time step. Then, the representative  $R$  value  $\tilde{R}_{lon}(\lambda_g, i)$  of spell is computed as the median of these longitudinally averaged  $R$  values  $R_{lon}(\lambda, t)$  during the lifetime of the spell (from  $t^{start}$  till  $t^{end}$ ):

$$\tilde{R}_{lon}(\lambda_g, i) = \text{median}\{R_{lon}(\lambda, t), t = t_{g,i}^{start}, \dots, t_{g,i}^{end}\} \quad (2.2)$$

The Weibull model fitted to the spell durations  $D_{g,1}, \dots, D_{g,n_g}$  at each grid point  $g$  is given by:

$$\ln(D_i^{(g)}) = \alpha_{0,g} + \alpha_{1,g}\tilde{R}_{\lambda_g,i} + \sum_{j=2}^6 \alpha_{j,g} m_j(t_{g,i}^{start}) + \sigma_g \varepsilon_{g,i} \quad i = 1, \dots, n_g, \quad (2.3)$$

where  $\alpha_{j,g}, j = 0, \dots, 6$ , are the regression coefficients,  $\varepsilon_{g,i}$  are the error terms following the standard extreme minimum value distribution and  $\sigma_g > 0$  is a scale parameter. Additionally,  $m_2, \dots, m_6$  are covariates representing dummy variables for each month (DJFMA/JJASO) to account for seasonal variations in spell durations and  $R$  (Röthlisberger et al., 2019). The intercept  $\alpha_{0,g}$  represents the starting month (November/May). Fitting the model to spell durations at each grid point then results in maps of regression coefficients  $\alpha_{j,g}, j = 0, \dots, 6$  where  $\alpha_{1,g}$  represents the effect of  $\tilde{R}$  on the spell durations. The null hypothesis examined here is that RRWPs have no effect on the duration of dry and wet spells, which is rejected at a grid point  $g$  if  $\alpha_{1,g}$  is significantly different from zero. Two-sided significant departures of  $\alpha_{1,g}$  from zero are identified as in Zhang (2016) at a significance level of 0.025 and 0.975.

Hereafter, we present the exponentiated regression coefficient  $\exp(\alpha_1)$  called “acceleration factor” (AF) in survival analysis applications (e.g., David W. Hosmer, 2008; Zhang, 2016; Röthlisberger et al., 2019). The AF  $\exp(\alpha_{1,g})$  depicts the factor by which all quantiles of the spell duration  $D_g$  at a grid point  $g$  changes per unit increase in the covariate  $\tilde{R}_{lon}(\lambda_g, i)$  (David W. Hosmer, 2008). Here, we use the AFs to identify statistically significant links between RRWPs and spell durations, and therefore focus on regions where AF is significantly larger or smaller than 1, and not on the AF values themselves. Regions with  $\text{AF} > 1$  ( $\text{AF} < 1$ ) experience significantly increased (decreased) spell durations with an increasing  $R$  value, i.e., during RRWP conditions. We tested the sensitivity of our results to changes in the minimum spell duration and the gap duration parameters. We found consistent AF patterns for the minimum spell durations of 4, 5, 6 days with the respective gap duration of 0 and 1 day. We also test the goodness-of-fit of our model with an Anderson-Darling test at significance level 0.01, exactly as in (Röthlisberger et al., 2019).

## 2.5 Results

### 2.5.1 Examples of persistent wet and dry spells during RRWPs

Two case studies serve to introduce key concepts of this study: a persistent wet episode in Spain, and a persistent dry episode in Brazil. During April-May 1983, persistent wet conditions over the Iberian Peninsula led to a 35-day long wet spell at a grid-point in western Spain (red cross in Figure 2.2a). The daily precipitation accumulation exceeded the local 90<sup>th</sup> percentile for 11 days during this spell. While blocking was present over south Greenland during the first 10 days of the spell (Figures 2.2b and 2.4a), a series of additional (and clearly distinct) transient wave packets moved across the Atlantic during the subsequent three weeks, which resulted in continuously high  $R$  values between 60° W and 30° E (Figure 2.2b). Recurrent flow conditions over the eastern Atlantic (Figure 2.2b) resulted in repeated advection of moist air to north-western Spain. Concurrently, precipitation anomalies were also present upstream over the Atlantic basin and downstream in the Mediterranean, all of which were associated with a wave pattern over the Atlantic basin (Figures 2.2 b and 2.4a), and consequently high  $R$  values. Note that no circumglobal wave pattern was present. The negative precipitation anomalies were co-located with the ridges and the positive precipitation anomalies were located downstream of the trough axes (Figure 2.4a). Interestingly, during this period, atmospheric blocks were also frequent over the Gulf of Alaska (Figure 2.4a).

In November 1985, recurrent Rossby waves were associated with persistent dry conditions over São Paulo, Brazil, and surroundings (Figure 2.3). A series of recurrent and non-stationary Rossby wave packets moved across the Southern Pacific in quick succession. It resulted in recurrent ridging over São Paulo (Hovmöller plot in Figure 2.3b). The wave pattern is also evident in the PV composite for this period (Figure 2.4b). Interestingly, blocking was not present over the São Paulo region, but two blocks appear over the Indian Ocean (south of Australia), one in the beginning and one towards the end of this period. There is an indication of anticyclonic wave breaking happening upstream of Patagonia in the Southern Pacific Ocean (Figure 2.4b).

Two additional case studies are included in the Supplementary material (Figures S5 and S7). These case studies clearly illustrate that besides blocking, recurrent amplification of troughs and ridges in the same geographical areas can also foster persistent dry and wet spells on subseasonal timescales. In the remainder of this study, we, therefore, quantify the effect of RRWPs on the persistence of dry and wet spells.

### 2.5.2 Rossby wave recurrence associated with dry spells

Next, we present AF fields and begin with dry spells in the Northern Hemisphere. Recall that  $AF > 1$  ( $AF < 1$ ) indicates a significant increase (decrease) of spell durations during RRWPs (i.e., for large values of  $R$ ). Figures 2.5a and 2.5b show that RRWPs significantly affect the

Northern Hemisphere dry spell durations during both the extended summer (MJJASO) and the winter (NDJFMA) seasons. However, this effect varies in sign depending on the region and the season. A positive effect of RRWPs on MJJASO dry spell durations is, for example, apparent in North America, central Europe, and eastern China (Figure 2.5a), while a negative effect is evident, for example, over eastern Iberia, western Greenland, and numerous subtropical regions. Moreover, during MJJASO, some indication of a wave-like pattern is evident, in particular between  $120^\circ$  W and  $60^\circ$  E in the extratropics. During the NDJFMA (Figure 2.5b), significant Northern Hemisphere AF patterns have clear latitudinal structure, with widespread  $AF < 1$  in the subtropics and the Arctic. Moreover, the mid-latitudes again feature a rather wave-like AF pattern (approximately WN 4) in the extratropics, in particular over the US and the Atlantic. Note that in both seasons widespread  $AF > 1$  regions are present in the mid-latitudes, but only some parts of the US have  $AFs > 1$  in both seasons (Figures 2.5a and 2.5b).

Moving on to the Southern Hemisphere (SH) dry spells, we find that RRWPs significantly affect dry spell durations during MJJASO and NDJFMA, albeit more strongly during the latter (Figure 2.5). During NDJFMA,  $AFs > 1$  are found over parts of subtropical South America, south-eastern Australia, and New Zealand, and  $AFs < 1$  over parts of Patagonia, southern Africa, and northern and central Australia. Moreover, the majority of the  $AFs > 1$  are present in the mid-latitudes. During MJJASO, however, the AF field shows a patchy structure, with coherent regions of statistically significant  $AFs (<1)$  primarily in the subtropics and along the Antarctic coast.

### 2.5.3 Rossby wave recurrence associated with wet spells

Similarly, for wet spell durations, the effect of RRWPs is dependent on the region and the season (Figure 2.6). In the NH, there are coherent regions with significantly longer wet spells during MJJASO in western Europe (France, Iberia) and western Russia (Figure 2.6a). In contrast to  $AFs$  for dry spells, for wet spells there are only few North American grid points with  $AFs$  significantly different from zero (cf. Figures 2.5a and 2.6a). During NDJFMA, RRWPs are associated with longer wet spells mainly over eastern Europe and the Mediterranean (Figure 2.6b), whereas large and reasonably coherent regions of  $AFs < 1$  appear over the eastern North Atlantic (including Ireland, the UK) as well as over North-western Russia. Furthermore, no latitudinal structure in the wet-spell  $AFs$  is apparent in the Northern Hemisphere. However, note that many high-latitude and subtropical areas are excluded from this analysis due to too few wet spells.

In contrast, in the SH (Figure 2.6), the AF fields exhibit a clear latitudinal structure that is evident in both seasons. The AF patterns indicate an increase of wet spell durations associated with RRWPs between  $30^\circ$  S and  $50^\circ$  S, and a decrease of wet spell durations associated with RRWPs south of  $50^\circ$  S. In particular, positive AF regions are apparent for both seasons over subtropical South America and parts of New Zealand.

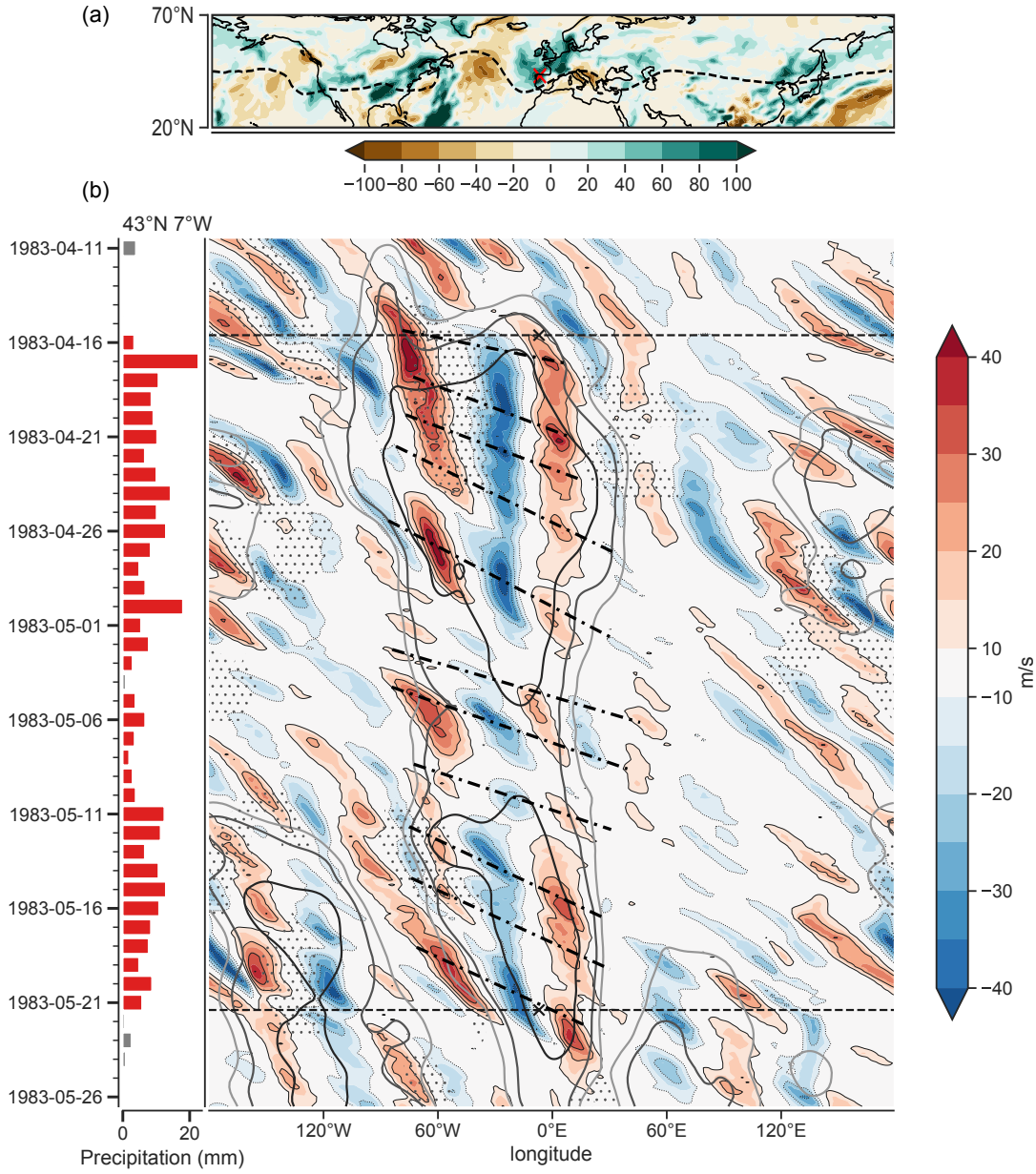


Figure 2.2: An example wet spell during 1983-04-16 till 1983-05-21. (a) Anomalous daily precipitation (mm) compared to ERA-I daily climatology (1979-2018) aggregated for the spell duration. Dashed contour shows 2PVU at the 330 K isentropes averaged for the spell duration. (b) Bars show aggregated daily precipitation at location ‘X’ (43°N, 7°W) in (a), red when precipitation is in the spell period and above 1 mm threshold, else grey. The Hovmöller diagram in (b) shows 35°N–65°N averaged meridional wind at 250 hPa. Black dotted lines in (b) mark the onset and end of the spell at ‘x’ in (a). Grey contours show  $R$  values of 8, 10, 14  $\text{ms}^{-1}$ . Stipplings depicts longitudes at which at least one grid point in 20°N–70°N featured an atmospheric block while the dash-dotted lines indicate the approximate longitude–time trajectory of the Rossby wave packets (i.e., group propagation).

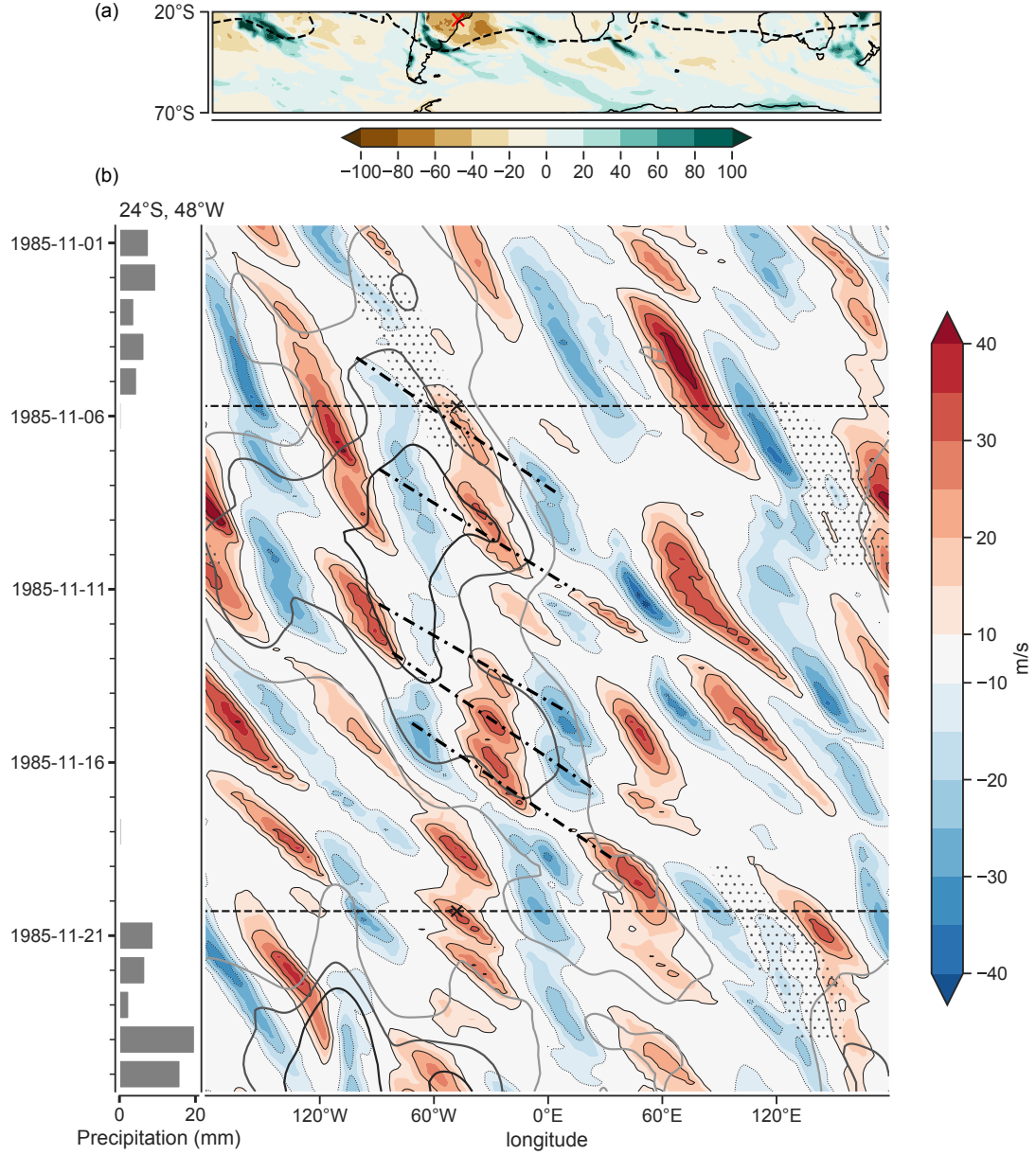


Figure 2.3: (a) and (b) same as Figure 2.2 but for a dry spell event at 24°S, 48°W (Brazil) during 1985-11-06 till 1985-11-20. Dashed contour in (a) shows -2PVU at the 345 K isentropic averaged for the spell duration. The Hovmöller diagram and the R-metric has been computed for 35°S–65°S. Grey contours in (b) show R values of 8, 10, 12 ms<sup>-1</sup>.

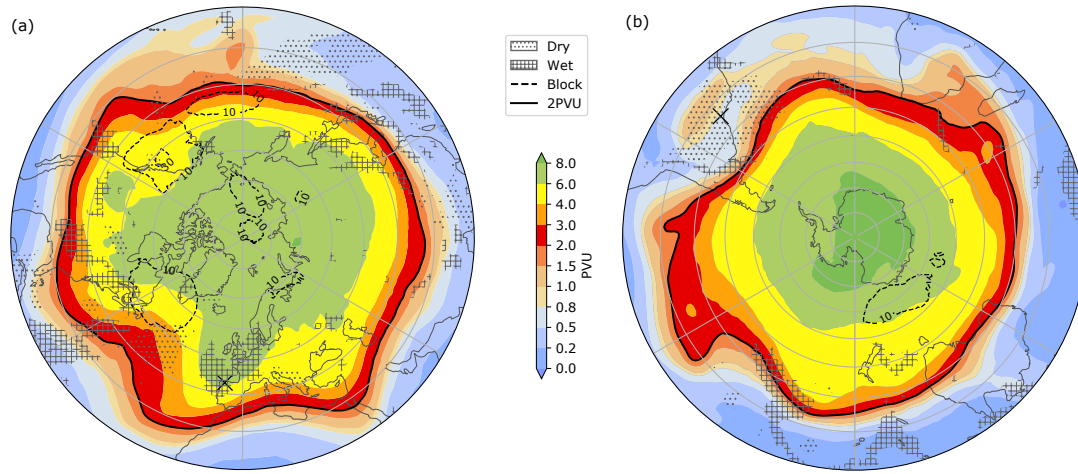


Figure 2.4: (a) PV at the 335K isentropes averaged over the duration of wet spell shown in Figure 2.2. (b) Same as in (a) but at the 345K isentropes for the dry spell examined in Figure 2.3. Daily precipitation anomalies are aggregated for the spell duration having precipitation anomalies greater than 40 mm (less than -40 mm) and are indicated by the corresponding hatches (see legend). Dashed contours show blocking frequencies in percent. The 'X' indicates the grid points for which the precipitation time series are shown in panels (b) of Figures 2.2 and 2.3.

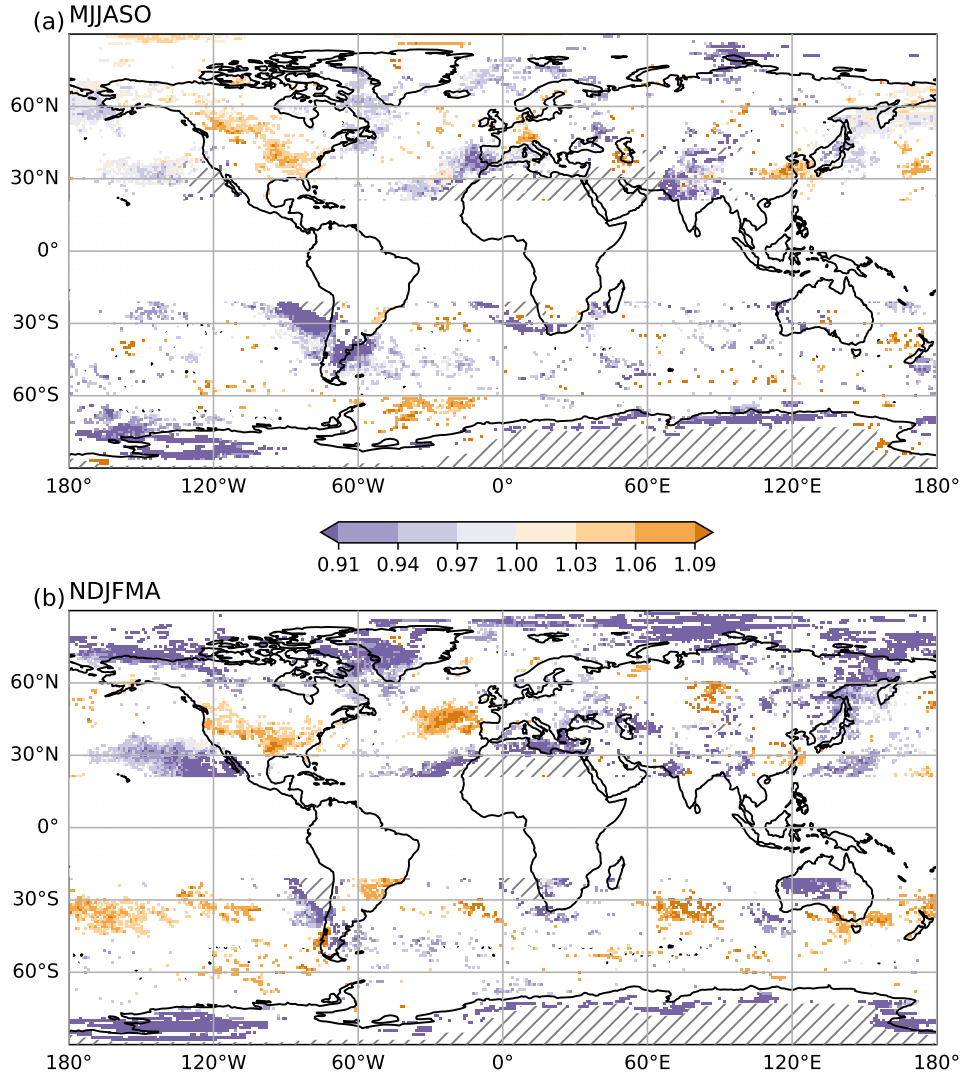


Figure 2.5: Statistically significant acceleration factors for (a) MJJASO and (b) NDJFMA dry spells. Northern Hemisphere (Southern Hemisphere) grid points show AFs from a Weibull model with the NH (SH)  $R$ -metric as a covariate, respectively. AFs between 20°S and 20°N are masked out to visually separate AFs for Northern (Southern) Hemisphere  $R$ . Lined hatches show areas excluded from the regression model due to too few spells. Stippling denotes areas where the spell durations do not fit our Weibull model based on an Anderson-Darling test at significance level 0.01.

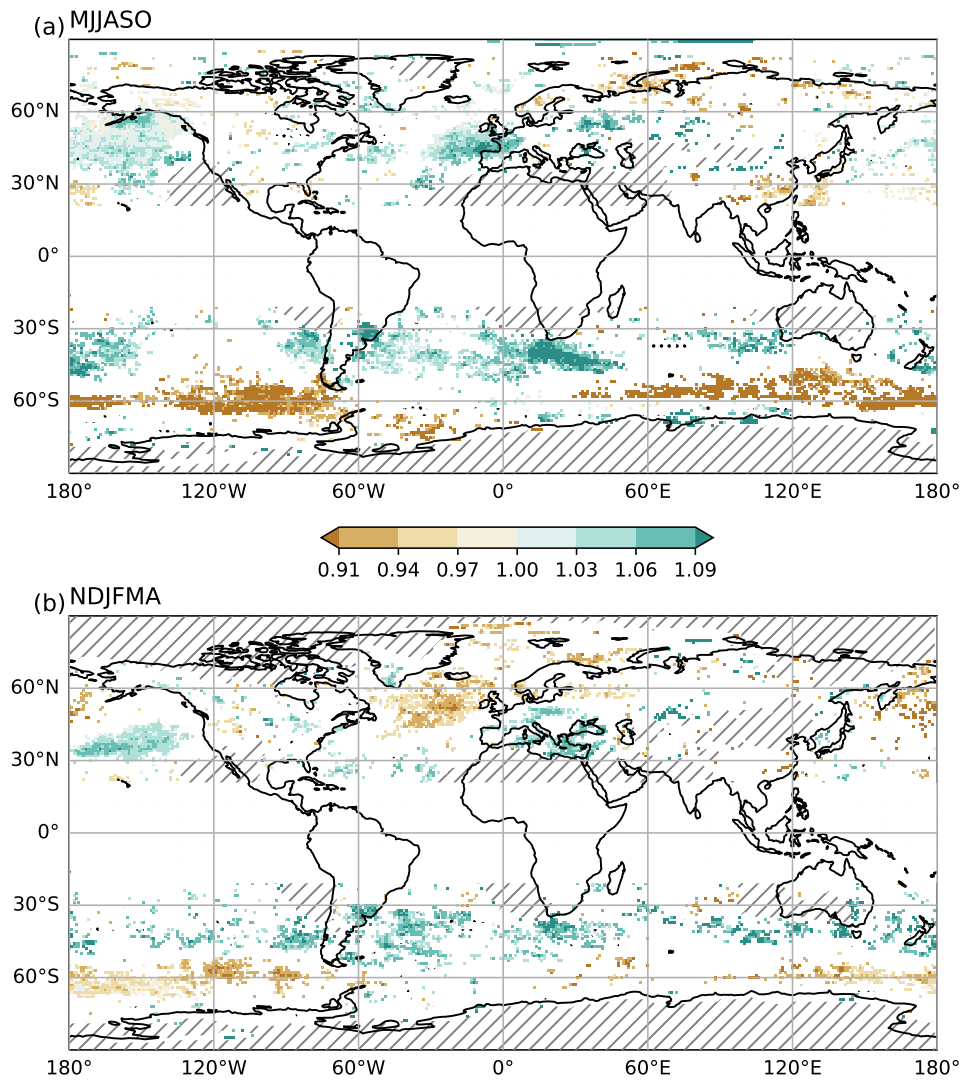


Figure 2.6: Same as Figure 2.5 but for (a) MJJASO and (b) NDJFMA wet spells.



## 2.6 Discussion

Our results demonstrate that recurrence of transient Rossby waves significantly affects the persistence of dry and wet spells. However, its effect can take either sign; it can both increase or decrease wet and dry spells.

Most regions where RRWPs are associated with a decrease in spell durations are regions where persistence is large climatologically, for example, in the subtropics and the Arctic for dry spells, and in the storm track regions for wet spells (for median spell durations see Figures S2 and S4). This implies that the recurrent troughs and ridges can interrupt wet and dry periods in these regions and reduce persistence.

The AF patterns for wet and dry spells arise from a combination of three components: a zonally symmetric component, a wave-like component, and a local component. The zonally symmetric component is most coherent in winter. It is characterized by distinct latitudinal bands in the AFs: with increased wet spell persistence on the equatorward side of the storm tracks (most evident in winter for NH Pacific and SH storm tracks), and reduced wet spell persistence in the central part of the storm tracks (both for NH Pacific and Atlantic, and SH storm tracks in winter). Furthermore, it features increased dry spell persistence in the parts of North Atlantic (NDJFMA) and the South Atlantic (MJJASO) storm tracks and reduced dry spell persistence in the subtropics and Arctic.

The zonally symmetric part can be understood by recalling that RRWPs are highly amplified flow situations. Hence, they lead to increased moisture transport into the polar regions and frequent RWB. The increased polar moisture transport can interrupt dry spells (e.g., Ali and Pithan, 2020; Papritz and Dunn-Sigouin, 2020; Uotila et al., 2013). Similarly, frequent RWB can foster unusually persistent wet conditions on the equatorward flank of the storm tracks (e.g., de Vries et al., 2013; De Vries, 2021) and interrupt dry spells by triggering convection (e.g., Funatsu and Waugh, 2008; McTaggart-Cowan et al., 2008). Recurrent ridging in the central part of the storm tracks (which are climatologically very wet regions) can shorten wet spells there Wernli and Schwierz (2006). The zonally symmetric part has also been discussed in (Röthlisberger et al., 2019) (their Figure 10a), but for persistent cold spells in winter.

The wave-like component in the extratropical AF fields is relevant for dry spells in the NH and is more evident during boreal winter (Figures 2.5b and 2.6b). A similar wave-like component has also been reported by (Röthlisberger et al., 2019) (their Figure 10b) for NH hot spells during summer, having a wavenumber 6-7. However, there is no clear circumglobal wavenumber for the AF patterns of dry and wet spells. The presence of such a wave-like component in the AFs implies that the RRWPs occur in preferred phases, i.e., the formation of troughs/ridges within RRWPs occurs in preferred geographical regions. In areas where RRWPs increase wet spell duration, potentially recurrent highly amplified upper-level troughs contribute to frequent

precipitation along their downstream flank via quasi-geostrophic lifting. For example, the wet spell case in Spain during April-May 1983 described before, where recurrent troughs were present just east of the Iberian west coast (e.g; Figures 2.2 and 2.4a). Similarly, in areas where RRWPs are associated with longer dry spell durations, potentially recurrent upper-level ridges ensure dry and stable conditions (e.g., Figures 2.3 and 2.4b). Moreover, the lack of such a wave signal in the SH extratropics and the wavenumber dependence on the season (change from WN4 in winter to WN6 in summer) suggests that the wave component in the AF fields is related to the stronger planetary waves in the NH that organise the transient eddies in preferred phases. However, note that the wave patterns should not be interpreted as occurring concomitantly and hence, as a circum-hemispheric wave. Although, such Rossby wave packets might exist, but we cannot infer their presence from the AF patterns. It remains to be investigated to what extent this wave-like component in the AF field relates to Quasi Resonance Amplification, etc (Kornhuber et al., 2017b).

Finally, the intricacies of local effects such as orography and moisture availability also affect AF patterns. For example, the case study shown in Figures 2.2 and 2.3 illustrates a long-lasting wet spell that is conceivably also affected by local orography. Furthermore, moisture transport is typically from the ocean towards the land and cannot cross major mountain ranges. This implies that local geography (coastline, mountain ranges, etc) play a role in determining whether a particular flow configuration is conducive to more/less persistent dry or wet spells.

## 2.7 Conclusion

Previously, mainly the stationary flow has been considered as an important driver of persistent weather conditions. Here, we demonstrate the importance of recurrent transient synoptic-scale Rossby wave packets (RRWPs) for persistent dry and wet conditions. RRWPs provide a non-stationary mechanism for modulating persistent surface weather. (Röthlisberger et al., 2019) showed that RRWPs affect Northern Hemisphere temperature spells. Here, we demonstrate that RRWPs also significantly affect the duration of dry and wet spells globally by significantly shortening or extending the persistent dry/wet conditions. Spatial patterns of statistically significant regression coefficients feature superimposed components, a zonally symmetric component, and a wave-like component that are modulated by local effects, presumably arising from the local geography, such as orography or the position relative to major moisture sources. The zonally symmetric component is apparent during the Northern Hemisphere winter and dominates the Southern Hemisphere signal in both the seasons. The wave-like component appears primarily in the Northern Hemisphere, changes its wavenumber with the season, and is possibly related to stationary wave dynamics. Despite the regional variations in modulating wet/dry spell persistence, our results demonstrate that RRWPs significantly alter the persistence of potentially high-impact surface weather; RRWPs should, therefore, be considered as an essential flow feature for understanding and predicting persistent sub-seasonal weather patterns.

## 2.8 Acknowledgments and Data availability

SMA and OM acknowledge the Swiss National Science Foundation grant number 178751. MR acknowledges the European Research Council (ERC) for funding (INTEXseas, grant agreement number 787652). ERA-I reanalysis data (Dee et al., 2011), and open source Python packages (Hoyer and Hamman, 2017; Hunter, 2007; Kluyver et al., 2016) helped us immensely. We are also grateful to the two anonymous reviewers whose comments helped to improve this paper. Datasets created in this study are available from FAIR-aligned repository in the in-text data Ali (2020).



## Chapter 3

# Recurrent Rossby waves and South-eastern Australian heatwaves

The following chapter is part of the manuscript titled as "Recurrent Rossby waves and South-eastern Australian heatwaves" submitted to the Weather and Climate Dynamics Journal and is under peer-review process at the time of writing the thesis (Ali et al., 2022). The manuscript is co-authored with Matthias Röthlisberger, Tess Parker, Kai Kornhuber, and Olivia Martius.

### 3.1 Abstract

In the Northern Hemisphere, recurrence of transient Rossby wave packets over periods of days to weeks, termed RRWPs, may repeatedly create similar surface weather conditions. This recurrence can lead to persistent surface anomalies. Here, we first demonstrate the significance of RRWPs for persistent hot spells in the Southern Hemisphere (SH) using the ERA-I reanalysis dataset and then examine the role of RRWPs and blocks for heatwaves over south-eastern Australia (SEA). A Weibull regression analysis shows that RRWPs are statistically associated with a significant increase in the duration of hot spells over several regions in the SH, including SEA. Two case studies of heatwaves in SEA in the summers of 2004 and 2009 illustrate the role of RRWPs in forming recurrent ridges (anticyclonic potential vorticity, PV anomalies), aiding in the persistence of the heatwaves. Then, using an observation-based dataset to identify SEA heatwaves, we find that SEA heatwaves are more frequent than climatology during days with extreme RRWPs activity. On days with both RRWPs and heatwaves, a circumglobal zonal wavenumber 4 anomaly pattern is present in the upper-level PV field, with an anticyclonic PV anomaly over SEA. In addition, we find positive blocking frequency anomalies over the Indian and the south Pacific Oceans, which may help to modulate the phase of RRWPs during SEA heatwaves.

## 3.2 Introduction

Since 1900, extreme heat has been responsible for more fatalities in Australia than all other natural hazards combined (Coates et al., 2014). Heatwaves also exacerbate the risk of wildfires, cause surges in power demand, and increase insurance costs (Hughes et al., 2020). Increasingly frequent and severe heatwaves in the midlatitudes in the recent years (Coumou et al., 2013; Perkins-Kirkpatrick and Lewis, 2020; Masson-Delmotte et al., 2021) have spurred fruitful research on the atmospheric drivers of heatwaves. Understanding the dynamical mechanisms is particularly important for improving sub-seasonal prediction (Quandt et al., 2017) and for quantifying future changes in heatwaves (Shepherd, 2014; Wehrli et al., 2019). Several large-scale atmospheric mechanisms and phenomena have been identified as potential drivers of heatwaves in the Northern Hemisphere extra-tropics. They include blocking anticyclones (e.g., Barriopedro et al., 2011; Drouard and Woollings, 2018; Kautz et al., 2022), amplified quasi-stationary waves (e.g., Teng et al., 2016; Kornhuber et al., 2017b), amplified Rossby wave patterns (e.g., Fragkoulidis et al., 2018; Kornhuber et al., 2020), and recurrent Rossby wave patterns (Röthlisberger et al., 2019). Fragkoulidis et al. (2018) showed that amplified Rossby waves are correlated with surface temperature extremes over NH and used process-based understanding to establish further association for the 2003 and 2010 NH heatwaves. RRWPs can be considered as a subset of amplified Rossby waves with a condition that the transient eddies recur spatially in the same phase on a short time scale of days to weeks. Here, we focus on recurrent Rossby wave patterns to explore their importance for heatwaves in south-eastern Australia (SEA).

Broadly, heatwaves in SEA (Fig. 3.1), comprising the states of Victoria (VIC), New South Wales (NSW), South Australia (SA), and Tasmania (TAS), are associated with slow-moving transient anticyclonic upper-level potential vorticity (PV) anomalies over the Tasman Sea (e.g., Marshall et al., 2014; Parker et al., 2014a; Quinting and Reeder, 2017; Parker et al., 2020). The anticyclonic PV anomalies and the associated subsidence drive heatwaves over VIC (Parker et al., 2014b; Quinting and Reeder, 2017). These anticyclonic PV anomalies can form as a part of synoptic-scale Rossby wave packet (RWP) (King and Reeder, 2021). These RWPs are often initiated several days before the onset of the heatwaves, but they amplify, and eventually break over SEA as anticyclonic equatorward (LC1-type) Rossby wave breaking (Parker et al., 2014a; O’Brien and Reeder, 2017).

Surface temperature anomalies associated with transient RWPs form, amplify, and decay on synoptic timescales, but the recurrence of RWPs in the same phase on a sub-seasonal timescale can result in persistent surface weather conditions by repeatedly re-enforcing the surface temperature anomalies (e.g., Hoskins and Sardeshmukh, 1987; Davies, 2015). Röthlisberger et al. (2019) termed this phenomenon “Recurrent Rossby wave packets” (RRWPs) and demonstrated a statistically significant connection between RRWPs and the persistence of surface temperature anomalies in the Northern Hemisphere (NH). Ali et al. (2021) found that RRWPs are also associated with increased persistence of dry and wet spells in several regions across the globe.

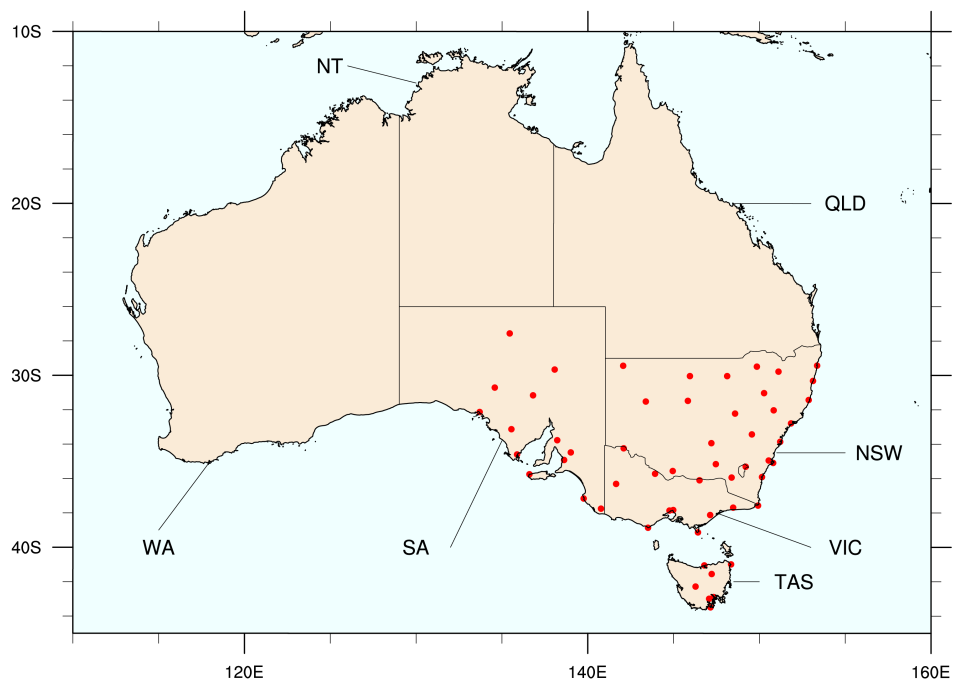


Figure 3.1: Map of Australia showing the states of South-eastern Australia (SEA): South Australia (SA), Tasmania (TAS), Victoria (VIC), and New South Wales (NSW). Other states shown are Queensland (QLD), Northern Territory (NT), and Western Australia (WA). Red dots indicate Australian Bureau of Meteorology's (BoM) monitoring stations used in this study (see Methods).

However, at least for some impacts, it is not only the simple occurrence of an extreme, however one defines an extreme, but also the duration of the extreme event that is important. This study addresses that aspect for the temperature extremes in the SH. More precisely, we evaluate the hypothesis whether an increase in R-metric, a measure of RRWPs (Röthlisberger et al., 2019), is associated with an increase in spell duration of the surface-temperature extremes over SH. Furthermore, we show how SH RRWPs relate to the persistent and extreme SEA heatwaves and demonstrate their association with the help of two case studies for the 2004 and 2009 heatwaves.

### 3.3 Methods

#### 3.3.1 Data

This study uses ERA-Interim (ERA-I) reanalysis data (Dee et al., 2011) provided by the European Centre for Medium-Range Weather Forecasts (ECMWF) on  $1^\circ$  by  $1^\circ$  spatial grid for 1979–2018. Various fields are used including horizontal velocity, meridional velocity, 2 m temperature, PV, and sea surface temperature (SST). The datasets are freely available to download from the ECMWF web server. The PV fields in the SH are multiplied by a factor of -1. The climatological mean is calculated with respect to the period 1980–2010.

#### 3.3.2 Recurrent Rossby waves

The metric  $R$ , developed by Röthlisberger et al., is used to identify recurrence of synoptic-scale Rossby wave patterns. For the SH, we use the same metric as in Ali et al. (2021). First, a 14.25 day running mean of 6-hourly meridional velocity fields  $v_{250}$ , averaged between  $35^\circ$  S and  $65^\circ$  S, are calculated to isolate signals with timescales longer than the synoptic timescale for each longitude  $\lambda$  and time  $t$ ,  $v_{tf}(\lambda, t)$ . The envelope of the synoptic wavenumber contribution to the time-filtered  $v$  is extracted following Zimin et al. (2003). To do this, the time-filtered  $v$  fields are transformed into the frequency domain using a fast Fourier transform over longitude,  $\hat{v}_{tf}(k, t)$ . Finally, an inverse Fourier transform is applied to calculate the envelope of the wave while only considering contributions from a selected band of synoptic wavenumbers  $k = 4$ –15. Thus,  $R(\lambda, t)$  for each longitude  $\lambda$  and time  $t$  is calculated as

$$R(l, t) = \left| 2 \sum_{k=4}^{15} \hat{v}_{tf}(k, t) e^{2\pi i k l / N} \right|, \quad (3.1)$$

where  $k$  is the wavenumber,  $l_\lambda$  denotes the longitudinal grid point index for longitude  $\lambda$  and  $N = 360$  denotes the number of longitudinal grid points. In most cases, large values of  $R$  reliably identify situations in which amplified waves (of distinct wave packets) recur in the same phase. However, the definition of  $R$  does not contain criterion for recurrence of distinct wave packets. Thus, in a few cases, high values of  $R$  over a few days may result from stationary synoptic-



scale troughs or ridges (see Röthlisberger et al. (2019) for discussion on metric  $R$ ). Fig. B.1 shows day-of-year climatology of the R-metric in the Southern Hemisphere and compares it to that of the Northern Hemisphere. The code for calculating R-metric is freely available (Ali and Röthlisberger, 2021). Phase and amplitude information of a particular wavenumber  $k$  can also be extracted using the same technique as in (1) and presented by Zimin et al. (2003). After applying the inverse Fourier transform, a complex number of the form  $a+ib$  is obtained. For extracting the wave packet or envelop, the amplitude of the complex number is taken as shown in equation 3.1. Instead of that, plotting the complex number on a complex plain provides information on the phase and amplitude at a given time step  $t$  for a particular wavenumber  $k$ . This is used to obtain a phase-amplitude distribution shown later.

### 3.3.3 Atmospheric Blocks

Atmospheric blocks are identified from persistent anticyclonic PV anomalies averaged between 500 hPa and 150 hPa vertical levels with the detection scheme described in (Schwierz et al., 2004) as updated by Rohrer et al. (2020). The detection scheme uses a 1.3 PVU threshold, a persistence criterion of 5 days, and a minimum overlap of 0.7 between two timesteps. Blocking fields identified with this algorithm are available at 6 hourly temporal resolution and  $1^\circ$  by  $1^\circ$  spatial resolution. We tested the sensitivity of the blocking fields with a 1.0 PVU threshold for the two case studies and did not find blocking directly over SEA.

### 3.3.4 South-eastern Australian heatwaves

A station-based heatwave dataset is used to focus on extreme and persistent heatwaves in SEA to study the links between RRWPs, blocks, and QRA conditions. Following the methods developed in (Parker et al., 2014b) and refined in (Quinting and Reeder, 2017), heatwaves in SEA in December–February (DJF) are detected from temperatures observed at the Australian Bureau of Meteorology’s (BoM) monitoring stations (Fig. 3.1). The BoM’s Australian Climate Observations Reference Network – Surface Air Temperature (ACORN-SAT) is a high-quality temperature dataset used to monitor long-term temperature trends. The dataset provides a daily maximum temperature (TMAX) for each station. These TMAXs are extracted for stations in SEA as defined here, for DJF from 1979 to 2019. The 90<sup>th</sup> percentile TMAX (T90) is then calculated for each station for each month in DJF. A heatwave is defined as any period of at least four consecutive days for which the TMAXs at three or more of these stations equal or exceed the T90 for that station and month. From here on, the term “heatwave” refers to heatwave in SEA. This criterion results in 57 heatwaves, which were on an average 8 days long with the longest heatwave lasting 22 days. Note that the purpose of the heatwave identification scheme is to identify the most intense and most persistent heatwaves in SEA, and thus serves a different purpose than the hot spell identification scheme described in the next section. Following Parker et al. (2014b), a day part of the SEA heatwaves is termed as SEA heat day. For evaluating the co-occurrence of SEA HD with RRWP conditions, high  $R_{SEA}$  days are defined as days exceeding the 90<sup>th</sup> percentile of

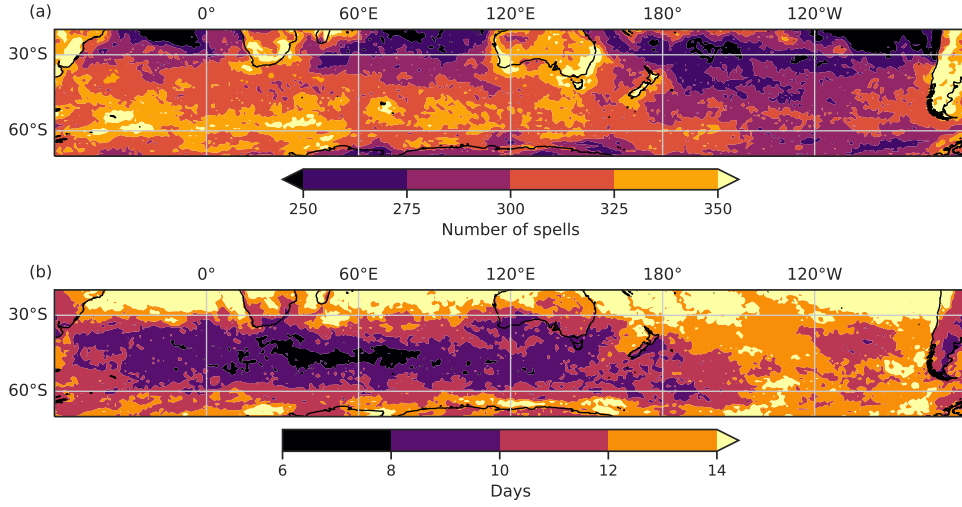


Figure 3.2: (a) Total number of hot spells in November–April identified at each grid point between 20° S and 70° S. (b) The 95<sup>th</sup> percentile of hot spell durations.

the daily mean  $R$  averaged over SEA (between 130° E and 153° E). The 90<sup>th</sup> percentile threshold is a subjectively chosen threshold consistent with the threshold for TMAX. Sensitivity test with a threshold of 85<sup>th</sup> percentile did not change the conditional probability shown in section 3.3.

### 3.3.5 Hot spells in the SH

Hot spells are identified for all SH grid points between 20° S and 70° S for 1980–2016 using 2 metre temperatures (T2M) from the ERA-I fields at 6 hourly temporal resolution and 1-degree spatial resolution. The hot spells definition follows that of Röthlisberger et al. (2019), in which a hot spell is calculated for each grid point as consecutive values exceeding the 85th percentile from the linearly detrended T2M fields. Spells separated by less than a day are merged to form a single uninterrupted spell. Spell durations of less than 36 hours are excluded from further analysis. Contrary to the SEA heatwave identification scheme, the purpose of the hot spell identification scheme is to identify many (not necessarily overly extreme) warm periods at each grid point, which can then be used for statistical analyses of the factors that determine the duration of these events. This statistical analysis (see next section) will be used to quantify the effect of RRWPs on the persistence of warm surface weather. To ensure a large sample size for robust statistical results, we identify hot spells for the period of November to April. Figure 2a shows the spatial distribution of the number of hot spells at each grid point between 20° S and 70° S. Higher number of hot spells are seen over land where parts of SEA, South Africa, and South America show 350 or more spells. The 95<sup>th</sup> percentile for hot spell duration varies from 6 days to more than 2 weeks (Fig. 2b). Over SEA, the 95<sup>th</sup> percentile duration varies from a week to roughly 2 weeks.

### 3.3.6 Weibull regression model to assess the effect of RRWPs in the SH hot spells

To quantify the effect of RRWPs on the persistence of hot surface weather, we extend an analysis from Röthlisberger et al. (2019) to the SH, including SEA, using the same statistical model setup, a Weibull regression model. This model allows us to model the distribution of the duration of hot spells at each grid point. An advantage of Röthlisberger et al. (2019) model is that we do not need to subjectively define the duration of a significant spell because the model accounts for the assessment of changes in all quantiles of the spell duration modelled. The null hypothesis tested here is that RRWPs have no effect on the duration of hot spells, which is tested at each grid point. The Weibull model is only briefly introduced here. Please refer to Röthlisberger et al. (2019) for further details and their Supporting Information for a detailed introduction to the Weibull model.

To fit the Weibull model to the observed spell duration, a representative value of the R-metric needs to be assigned to each hot spell. This is achieved in the following way: for each hot spell  $i$  at grid point  $g$  with a duration  $D(g, i)$ , the raw R-metric  $R(\lambda, t)$  is longitudinally averaged within a  $60^\circ$  longitudinal sector centred at the grid point  $g$  with longitude  $\lambda_g$  to yield  $R_{lon}(\lambda, t)$ . Then, a median of  $R_{lon}(\lambda, t)$  is calculated for the lifetime of the hot spell to assign a representative value of  $\tilde{R}_{lon}(\lambda_g, i)$  for each spell  $i$ . Thus, our model is given as:

$$\ln(D_i^{(g)}) = \alpha_{0,g} + \alpha_{1,g}\tilde{R}_{\lambda_g,i} + \sum_{j=2}^6 \alpha_{j,g} m_j(t_{g,i}^{start}) + \sigma_g \varepsilon_{g,i} \quad i = 1, \dots, n_g, \quad (3.2)$$

This model is fitted to duration of hot spells at each grid point  $g$  and results in a spatial field of regression coefficients  $\alpha_{j,g}$ ,  $j = 0, \dots, 6$  together with their  $p$  values. Here,  $\alpha_{0,g}$  is the intercept and  $\alpha_{1,g}$  represents the effect of  $\tilde{R}$  on the hot spell duration.  $\alpha_{j,g}$  are regression coefficients for dummy variables  $m_j(t_{g,i}^{start})$  that take the value 1 if spell  $i$  starts in month  $m_j$ , and zero otherwise. The coefficients  $\alpha_{j,g}$ , therefore, account for possible seasonality in the spell duration distribution at grid point  $g$  (e.g., longer hot spells in May compared to, e.g., September), while  $\sigma_g$  is a scale parameter and the  $\varepsilon_{g,i}$  are error terms.

The quantity  $\exp(\alpha_1)$  is usually referred to as acceleration factor (AF) and is of particular interest here, as it quantifies the factor of change in all quantiles of the distribution of spell duration at grid point  $g$  per unit increase in  $\tilde{R}$  (David W. Hosmer, 2008; Röthlisberger et al., 2019; Zhang, 2016). An AF  $> 1$  implies an increase in all spell duration quantiles with increasing  $R$  (i.e., during RRWPs), and conversely for an AF  $< 1$ .

Furthermore, fitting the model 3.2 to spell duration at all grid points results in a spatial field of AF. The statistical significance of the AF values is evaluated in a two-step approach. First, a p-value for the above null hypothesis is computed exactly as in Zhang (2016). Then, the false-discovery-rate (FDR) test of Benjamini and Hochberg (1995) is applied to the resulting field of p-values. The FDR test controls for type I errors, i.e., falsely rejecting null hypothesis that can

occur substantially in analyses like this one where multiple tests are being performed independently from each other at each grid point (e.g., Wilks, 2016). Here we follow the recommendation of Wilks (2016) and allow for a maximum false-discovery-rate  $\alpha_{FDR}$  of 0.1.

## 3.4 Results

### 3.4.1 RRWPs and hot spell durations

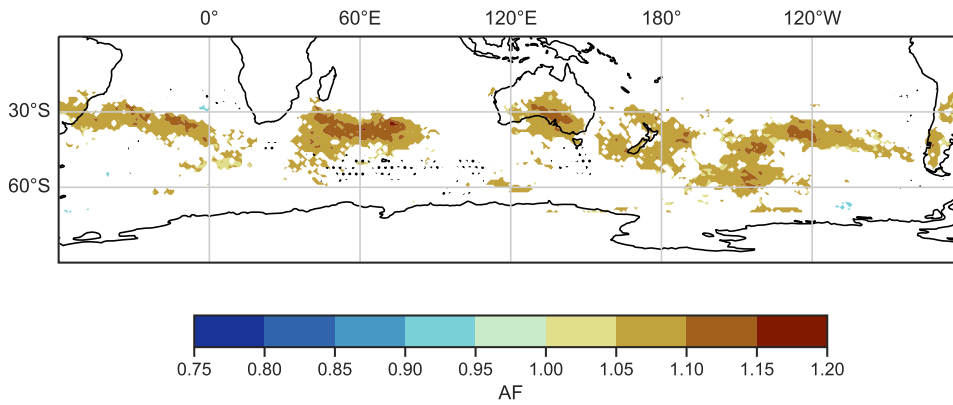


Figure 3.3: Statistically significant acceleration factors (AF) for hot spells in November–April between  $20^{\circ}$  S and  $70^{\circ}$  S. Colours show AFs from a Weibull model with  $R$ -metric as a covariate. Stippling indicates grid points where spell durations do not follow the Weibull model based on the Anderson–Darling test at a significance level of 0.01.

The Weibull analysis reveals that RRWPs are significantly correlated with the duration of hot spells in several regions within the SH and including over SEA (Fig. 3.3). Recall that AF larger than 1 means that an increase in  $R$  is related to an increase in hot spell duration and conversely for AF smaller than 1. Thus, several parts of central and southern Australia, including the states of SA, VIC, NSW, and TAS, experience longer hot spells during periods when RRWPs occur. Northern Australia, however, does not show such a correlation with RRWPs, which agrees with previous studies showing different dynamical pathways for Northern and Southern Australian heatwaves (Risbey et al., 2018; Quinting and Reeder, 2017; Parker et al., 2020). Other statistically significant areas over land include parts of South America: southern Brazil, Bolivia, and parts of Argentina and Chile. For Northern Hemisphere summer half-year, the significant AFs, larger than 1, form a wavenumber 7 pattern Röthlisberger et al. (2019). In contrast, no clear wave pattern emerges for the SH in the significant AFs in Fig. 3.3. The difference in AF patterns between the two hemispheres is consistent with different climatological stationary wave patterns. The spatial pattern in Figure 3.3 highlights areas where the transient waves building up the RRWPs have a predominant phasing in summer. In summary, the regression analysis shows that RRWPs are significantly associated with the duration of hot spells in several SH regions over land, including SEA. However, the Weibull analysis does not provide any information about the

processes and hence potential causal link between RRWPs and the most intense SEA heatwaves. Accordingly, we next focus on SEA heatwaves and elucidate the role of RRWPs and blocks for two selected cases studies of SEA heatwaves and investigate further co-occurrence of SEA heatwaves and days with high  $R$  activity.

### 3.4.2 RRWPs and Blocks during two extreme and persistent SEA heatwaves

#### 3.4.2.1 Case 1: 2004 Heatwave

The February 2004 heatwave (7–22 February) lasted for 16 days. More than 60 % of continental Australia recorded temperatures above 39°C during this event (National Climate Centre, 2004). At the time, this event was the most severe February heatwave on record in both spatial and temporal extent and ranked in the top five Australian heatwaves for any month (National Climate Centre, 2004). More than 100 stations in SA, NSW, and northern VIC experienced record temperatures for February, and in some regions all-time records were set for consecutive days of heat (BoM, 2004). Previous studies have shown that the upper-level anticyclonic PV anomalies over SEA during the heatwaves are associated with subsidence and is the major process causing the high surface temperature anomalies (e.g., Quinting and Reeder, 2017; Parker et al., 2020). The surface flow associated with anticyclonic anomalies may also advect warm continental air due to the north westerly flow at lower levels (e.g., Parker et al., 2014a). Here, we show how RRWPs contribute to persistent anticyclonic PV anomalies over SEA.

During this event, several Rossby wave packets were observed, recurrently amplifying in the same phase forming a ridge over SEA. The upper-level flow over SEA was zonal prior to the heatwave (Fig. 3.5a). An upper-level ridge forms over SEA around 5 February prior to the heatwave (Fig. 3.5b). The flow becomes more amplified in the subsequent days with a circumglobal amplified wave pattern apparent around 9 February (Fig. 3.5c). The amplified wave, part of a transient and non-stationary Rossby wave packet, RWP (P1 in Fig. 3.4b), arrived over the southern Indian Ocean, and an upper-level ridge began to form over Australia which amplified further around 13 February (Fig 3.5d). Two further ridges formed over SEA on 16 and 18 February (Fig. 3.5e, 3.5f), each ridge being part of a transient non-stationary RWP initiated upstream of Australia (P3, P4 in Fig 3.5b). These series of upper-level recurrent ridges were part of the RRWPs and contributed to the persistence of the heatwave. These recurrent ridges associated with RRWPs were also detected by the metric  $R$  (grey contours in Fig. 3.4b).

No blocks were identified directly over SEA during the heatwave, but blocks were present south of SEA and further downstream (Fig. 3.4, 3.5). The RWP labelled as P1 in Figure 3.4b formed downstream of a block B1 downstream of Australia where the block moved from south of Australia a few days earlier (Fig. 3.5b). Another block B2 was simultaneously present in the vicinity of South America around 7 February. In the next few days, simultaneous wave breaking was observed in the central Pacific Ocean and south of Africa in the Indian Ocean. Another set of

RWPs (P3 and P4 in Fig. 3.4b) seems to have been set off by a block over the Pacific Ocean (B3 in Fig. 3.5b). Simultaneously, another block was present south of South America (B4 in Fig. 3.4b, 3.5d), and seem to initiate another RWP (P3 in Fig. 3.4b). Block B4 was also associated with amplified Rossby waves downstream over the Indian Ocean on 16 February (Fig. 3.5e). Thus, we argue that blocks could have played a key role in the initiating, phasing, and meridional amplification of the four Rossby wave packets (P1–P4) that reached Australia between 13 and 18 February. In summary, we saw recurring RWPs that passed over Australia during this period (Fig. 3.4b). These waves were not stationary, they were not triggered in the same area, and not over Australia, and were initially not in phase upstream of Australia.

### 3.4.2.2 Case 2: 2009 Heatwave

The 2009 heatwave (27 January–9 February), although extensively covered in literature (e.g., Engel et al., 2013; Parker et al., 2014a), has been chosen because it is one of the most severe heatwaves in SEA. It lasted for 14 days. Between 28–31 January and 6–8 February, temperatures in SEA were exceptionally high. On Black Saturday, 7 February, the hot, dry, and windy conditions worsened many catastrophic fires in VIC, which recorded 173 fatalities, and more than 2133 houses were destroyed (Karoly, 2009; Parker et al., 2014a; Commission, 2010). During this heatwave, an anticyclone over SEA and the associated north-westerly flow at the surface advected hot continental air into SEA leading to extreme surface temperatures (Parker et al., 2014a).

Prior to the onset of the heatwave, the flow was already amplified with a wave breaking over SEA (Fig. 3.7a). Several RRWPs were observed prior to and during this event (P1 and P2 in Fig. 3.6b). The RRWPs prior to the heatwave were not in the same phase as those during the heatwave (Fig. 3.6b). Around 26 January, a Rossby wave packet (P2 in Fig 3.6b) was observed forming an upper-level ridge over Australia (Fig. 3.6b, 3.7b). In the subsequent days, the amplified wave broke anticyclonically over SEA (Fig. 3.7c), resulting in an anticyclonic PV anomaly over SEA (see Parker et al., 2014 for a detailed analysis of this event). On 2 February, a new ridge started forming over southern Australia (Fig. 3.7d) as part of Rossby wave packet (P3 in Fig 3.6b) and reached over SEA on 5 February (Fig. 3.7e). However, the upper-level ridge was transient and was replaced by another ridge around 7 February as part of another amplified wave (P4 in Fig. 3.6, Fig. 3.7f).

No blocks were identified directly over SEA during the heatwave (Fig. 3.6, 3.7). However, blocks were frequent upstream of SEA from 50° E to 70° E in the Indian Ocean (B2 in Fig. 3.6b, Fig. 3.7), and downstream of SEA from 200° E to 250° E (B1 in Fig. 3.6b, 3.7). Block B2 over the Indian ocean was particularly persistent and interacted with several amplified Rossby wave packets (P2, P4, in Fig. 3.6). B2 began to weaken around 2 February (Fig. 3.7d) but restrengthened again on 5 February (Fig. 3.7e) due to injection of low PV from a smaller southward moving block in the Indian Ocean (not shown). Therefore, B2 remained persistent throughout the heatwave. Rossby wave packet P1 formed downstream of the block B0 over the Pacific Ocean prior to the

heatwave (Fig 3.6b, 3.7a).

So far, we have investigated the association of RRWPs with duration of hot spells. We also presented two cases of extreme and persistent SEA heatwaves to show how RRWPs can lead to the formation or replenish the anticyclonic PV anomalies over SEA. Figure B1 shows another case of SEA heatwave associated with RRWPs. In the next section, we extend the analysis to a climatological period (1979–2018) and explore high  $R_{SEA}$  conditions for all the SEA heatwaves.

### 3.4.3 RRWP conditions during SEA heatwave

First, a note on the co-occurrence of high  $R_{SEA}$  days and SEA heatwave days (SEA HD) as defined in section 2.3. Out of 352 days with high  $R_{SEA}$ , 67 co-occur with SEA HD and 285 do not co-occur (Appendix B.2). Thus, the conditional probability of a SEA HD given high  $R_{SEA}$  is 0.19 ( $67/352=0.19$ ), which is higher than the climatology ( $457/3520=0.13$ ). Many high  $R_{SEA}$  days do not co-occur with SEA HD, which clearly indicates that R is not a sufficient condition for SEA heatwaves on its own. We, therefore, further explore that why some high  $R_{SEA}$  days co-occur with SEA HD while others do not.

High  $R_{SEA}$  days co-occurring with SEA HD feature a large anticyclonic PV anomaly over SEA (Fig. 3.8a) on the 350 K isentropic surface. The 2 PVU isoline on the 350 K isentropic surface, indicating the dynamic tropopause, is also located over SEA, thereby indicating a suitable choice of the isentropic surface. Upstream and downstream of the anticyclonic PV anomaly over SEA feature cyclonic PV anomalies that are also located equatorward of the highest blocking frequencies (black contours in Fig. 3.8a). These may correspond to the cyclonic PV anomalies surrounding omega-type blocking or the cyclonic PV anomalies of the dipole blocks. Since blocking is a binary dataset, the blocking frequency in Figures 3.8a and 3.8b indicates the percentage of days on which a grid point features a block. Thus, for high  $R_{SEA}$  days co-occurring with SEA HD, blocks are more frequent over the Indian and the south Pacific Oceans close to the Antarctic coast compared to high  $R_{SEA}$  days without co-occurring SEA HD (Fig. 3.8a, 3.8c) and less frequent over the 60° S latitude, the latitudinal band featuring high blocking frequency in the DJF climatology (Fig. 3.8c, 3.8f). In contrast, on high  $R_{SEA}$  days not co-occurring with SEA HD there is no spatial preference for the anticyclonic PV anomalies. Weak zonally elongated PV anomalies are present over the ocean basins, that are co-located with the blocking frequency fields (black contours in Fig. 3.8b). Near Australia, the centroid of the contour of anticyclonic PV anomaly appears around 30° downstream of SEA over New Zealand (Fig. 3.8b) compared to over SEA in Figure 3.8a. The difference in the spatial distribution of PV anomalies on the high  $R_{SEA}$  days not co-occurring with SEA HD and the high  $R_{SEA}$  days co-occurring on SEA HD suggests that only the RRWPs whose phase is conducive to forming ridges over SEA are important for SEA heatwaves.

In addition to the ridge over SEA, a circum-hemispheric zonal wavenumber 4 (WN4) pattern

is present in the composite mean PV fields for high  $R_{SEA}$  days co-occurring on SEA HD (Fig. 3.8a). This WN4 pattern does not have the same distribution of PV anomalies as the WN4 extracted from the Fourier decomposition of the climatological mean PV field for DJF: the WN4 climatology features the anticyclonic PV anomaly node roughly  $30^\circ$  west of SEA (Fig 3.8d, 3.8e).

A high fraction of WN4 flow during high  $R_{SEA}$  days co-occurring on SEA HD is in phase (Fig. 3.9). Figure 3.9 shows the phase and amplitude density distribution of the WN4 component of the meridional winds averaged between  $35^\circ$  S and  $65^\circ$  S. Phase and amplitude information for each wavenumber can be extracted using a Fourier decomposition as shown in methods. On high  $R_{SEA}$  and SEA HD, the density distribution in the complex plane is unimodal point to a preferred phasing of the wave that is reflected in WN4 pattern visible in the PV composite (Fig. 3.8a). On high  $R_{SEA}$  and non SEA HD, density distribution in the complex plane is bimodal and generally much broader, that agrees with the PV composite that shows no clear WN4 pattern (Fig. 3.8b). The phase distribution for wavenumber 4 is shown here because it emerges as the dominant pattern in the composite mean (Fig. 3.8a), whereas density distributions for other wavenumbers do not exhibit a clear difference (not shown). Overall, our results agree with the understanding of SEA heatwaves featuring upper-level anticyclonic PV anomalies over SEA (Marshall et al., 2014; Parker et al., 2014a; Quinting and Reeder, 2017), and we show how RRWPs in a particular phase are conducive to forming anticyclones over SEA.



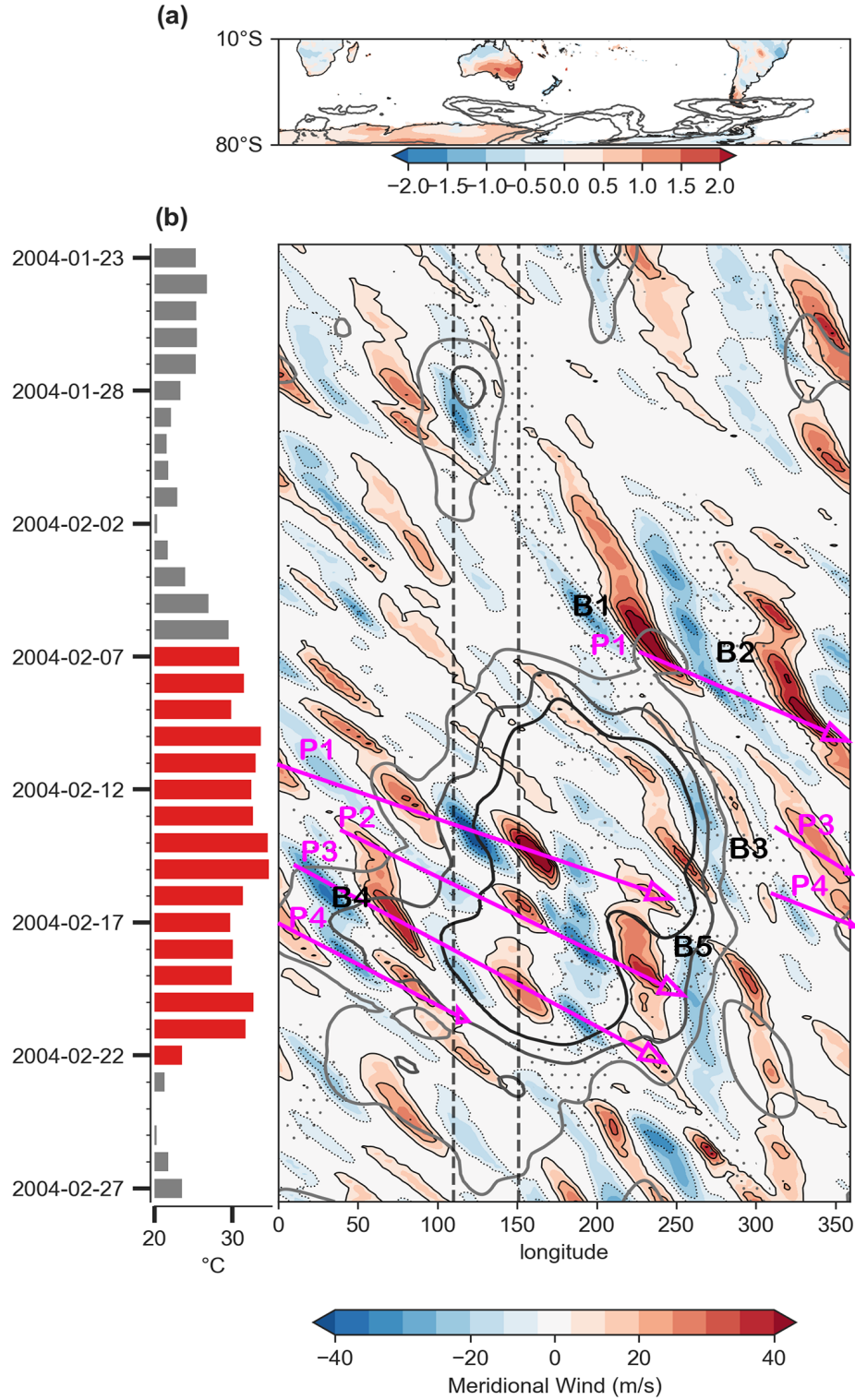


Figure 3.4: RRWPs, and blocks during 2004 SEA heatwave. (a) Filled contours depict the time-mean standardized anomalies of daily maximum 2 m temperature over land for the duration of the heatwave. Contours show the mean blocking frequency during the heatwave (5, 10, 20 %). (b) Bars show daily maximum 2 m temperature averaged over SEA ( $^{\circ}\text{C}$ ); red marks the heatwave period. The Hovmöller diagram shows the meridional wind at 250 hPa averaged between 35° S and 65° S (filled contours,  $\text{ms}^{-1}$ ), R values (grey contours, 6, 8, 10  $\text{ms}^{-1}$ ), and longitudes at which at least one grid point between 40° S and 70° S featured an atmospheric block (stippling). Rossby wave packets (blocks) are labelled in magenta (black).

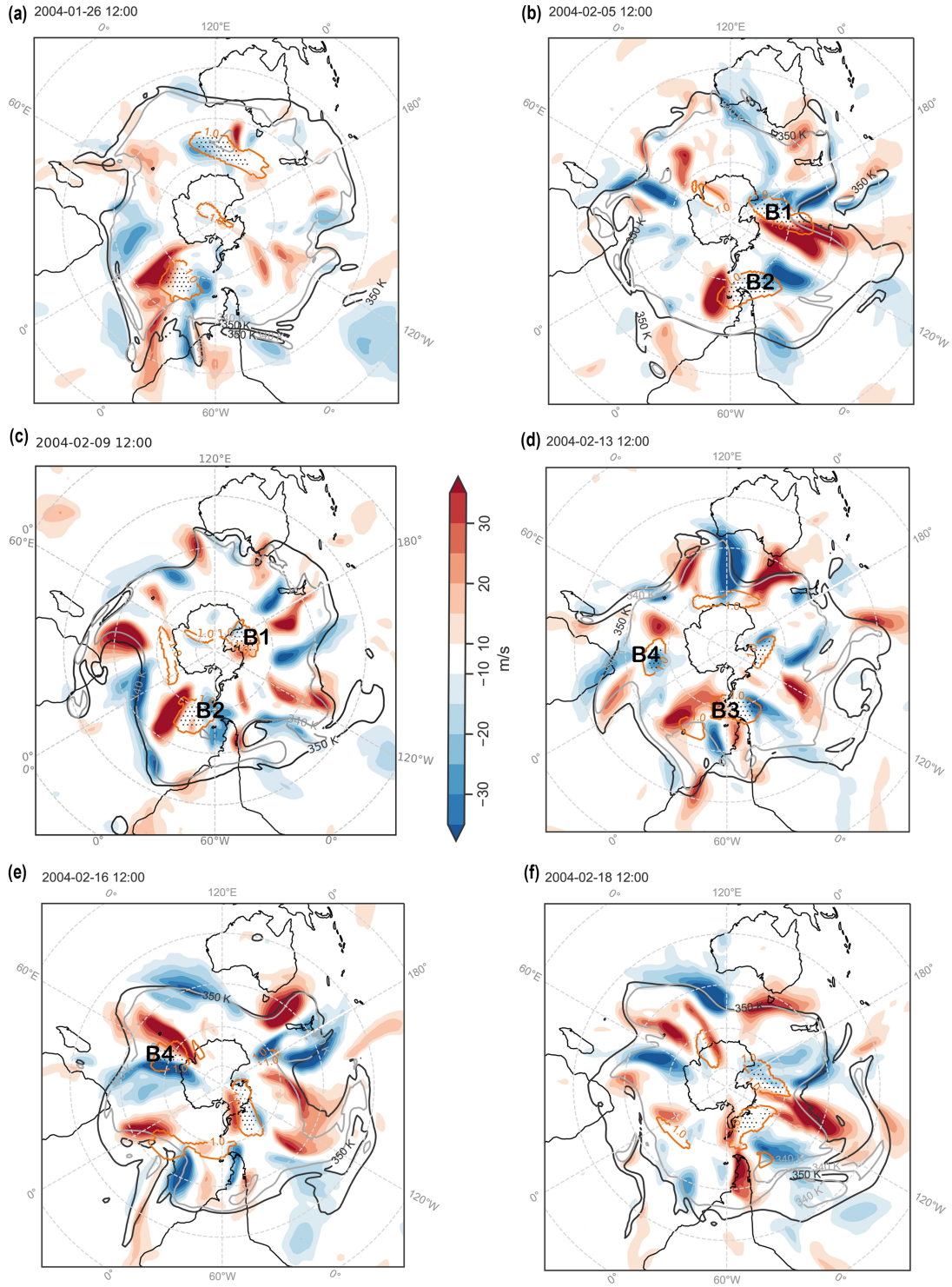


Figure 3.5: (a), (b), (c), (d), (e), and (f) show meridional velocity at 250 hPa (colour shading), 2 PVU contours at isentropes 340 K (black line) and 350 K (grey line) at various time steps. Stippling and orange contours show blocks identified using a 1.3 and 1.0 PVU threshold, respectively.

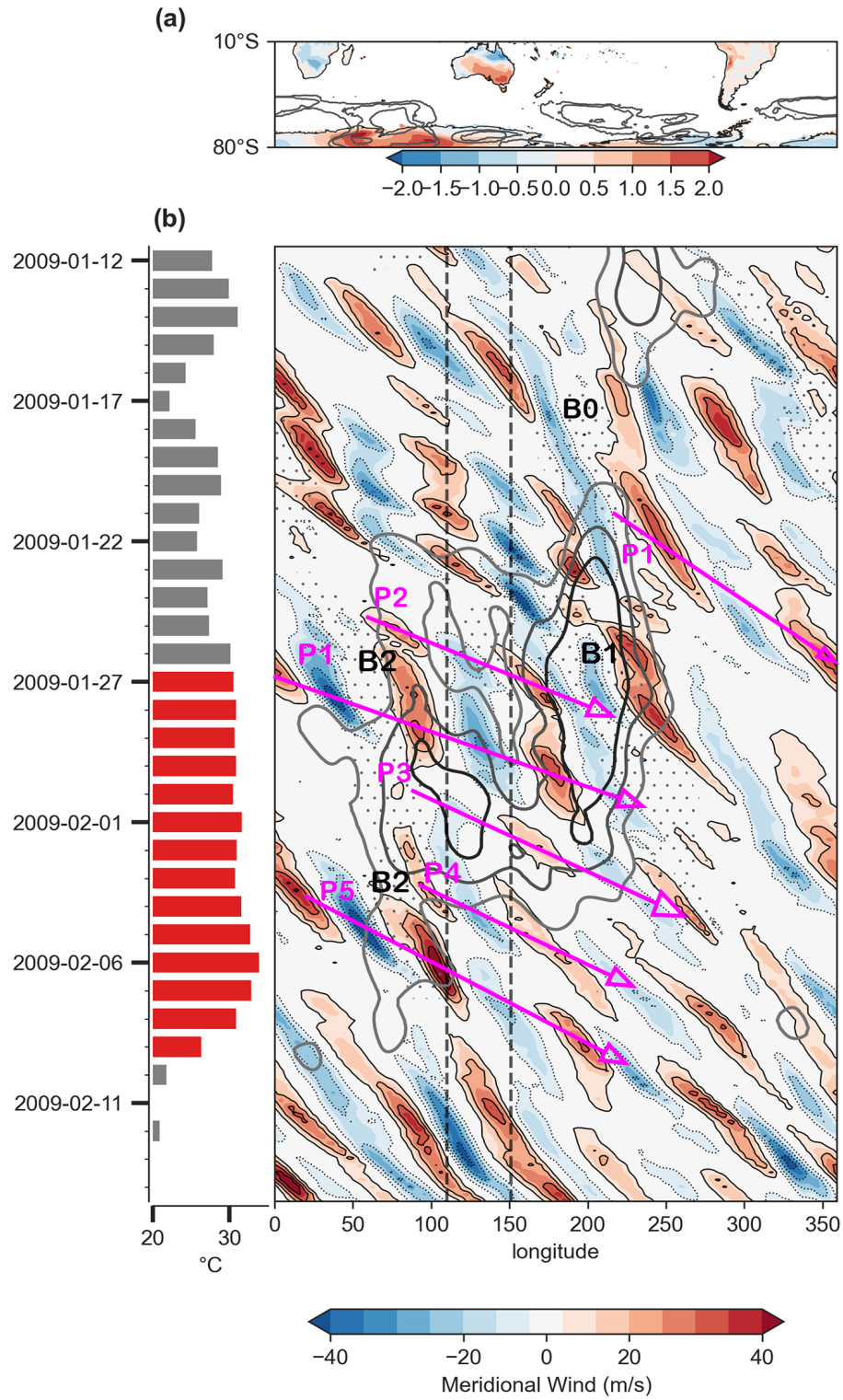


Figure 3.6: Same as in Fig. 3.4 but for February 2009 SEA heatwave.



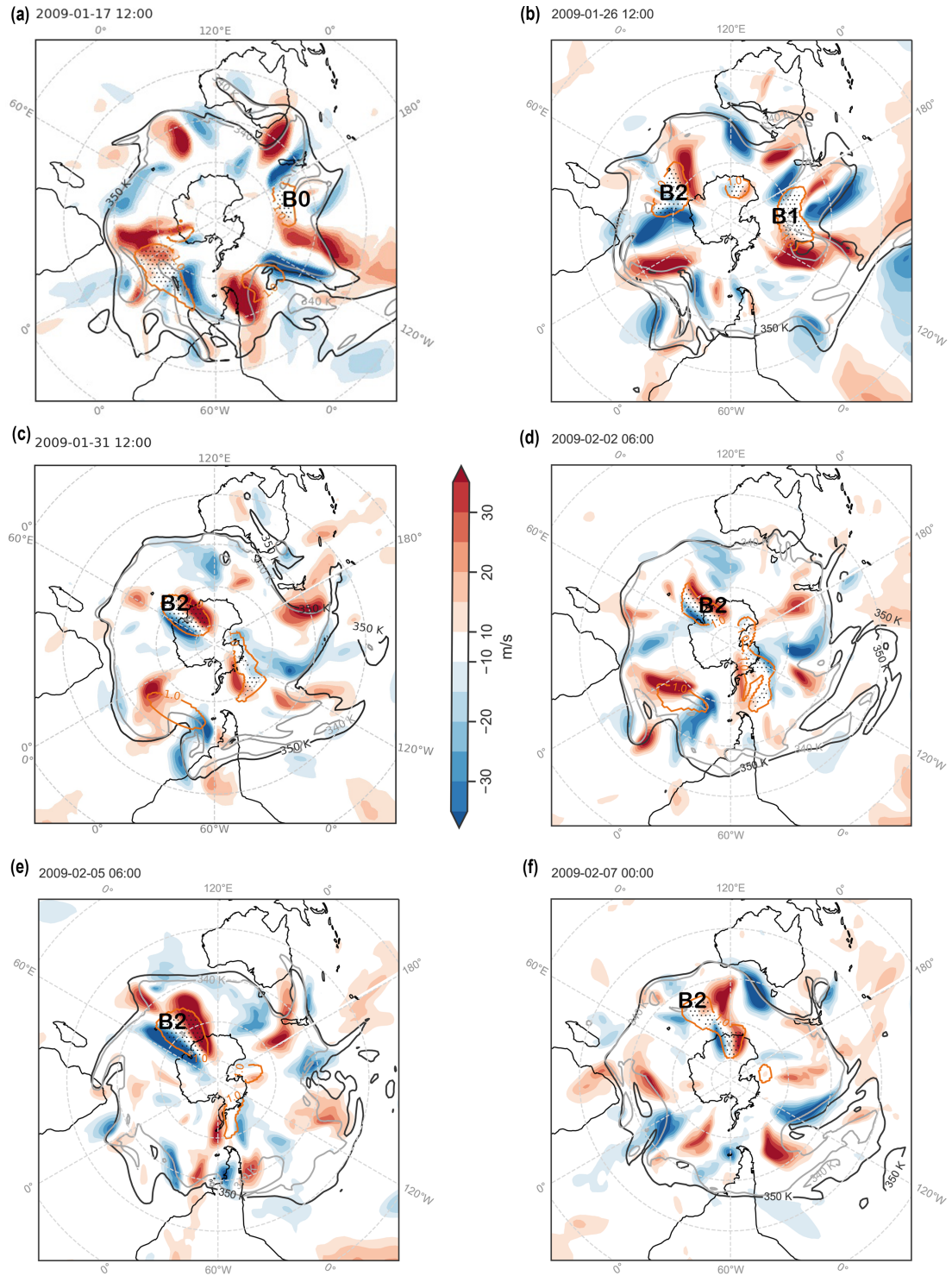


Figure 3.7: Same as in Fig. 3.5 except for 2009 SEA heatwave.

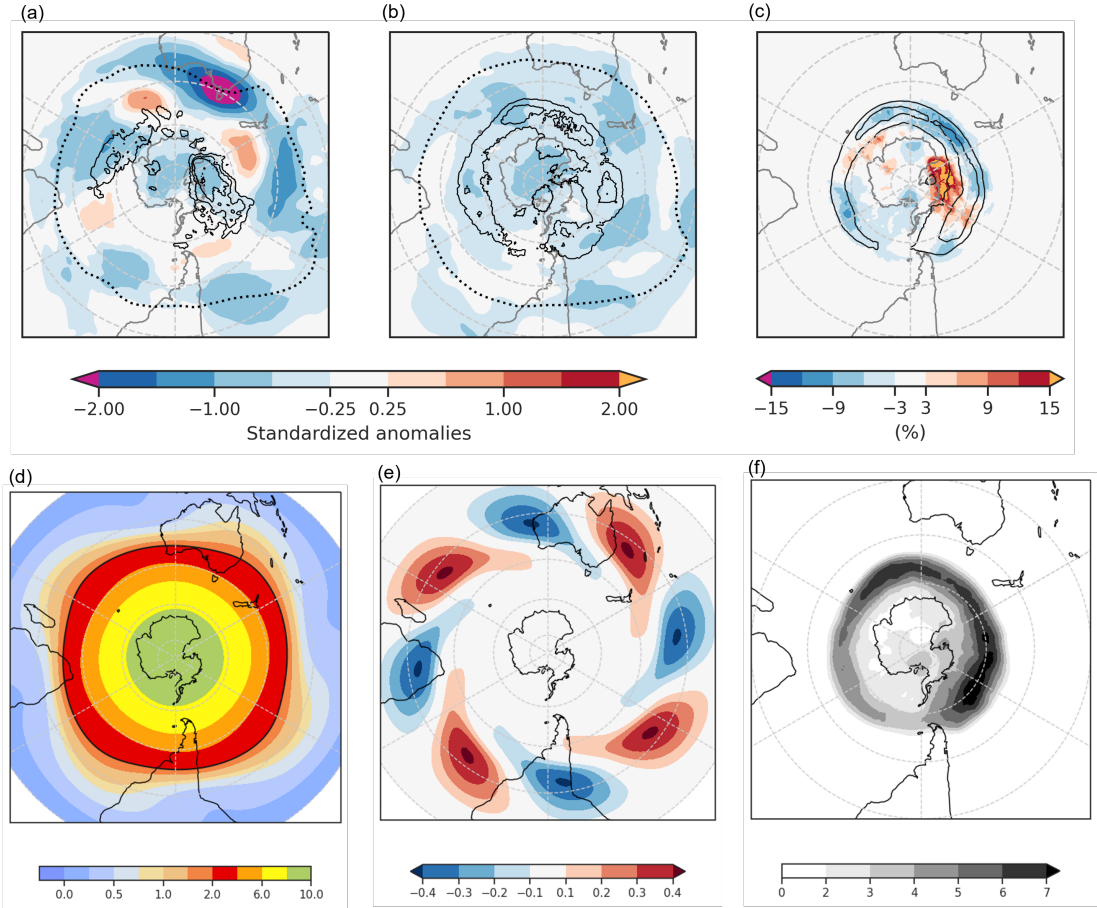


Figure 3.8: Standardized PV anomalies on the 350 K isentrope with respect to the DJF climatology (1979–2018) for (a) High  $R_{SEA}$  days and SEA heatwave days (HD), (b) High  $R_{SEA}$  days and non-SEA HD. Dotted black lines show 2 PVU contour in the mean PV fields for (a) and (b), and black contours show mean blocking frequency contours at 5, 10, 15 % for the same. (c) Shows the difference in blocking frequency between (a) and (b). (d) shows the sum of PV (in PVU) from the zonal wavenumber,  $k=4$  component of the DJF climatology at 350 K (shown in e) and the  $k=0$  (the DC) component. (f) shows the climatological mean blocking frequency (%) for DJF, and black contours in (c) show the same at 4, 6 %.

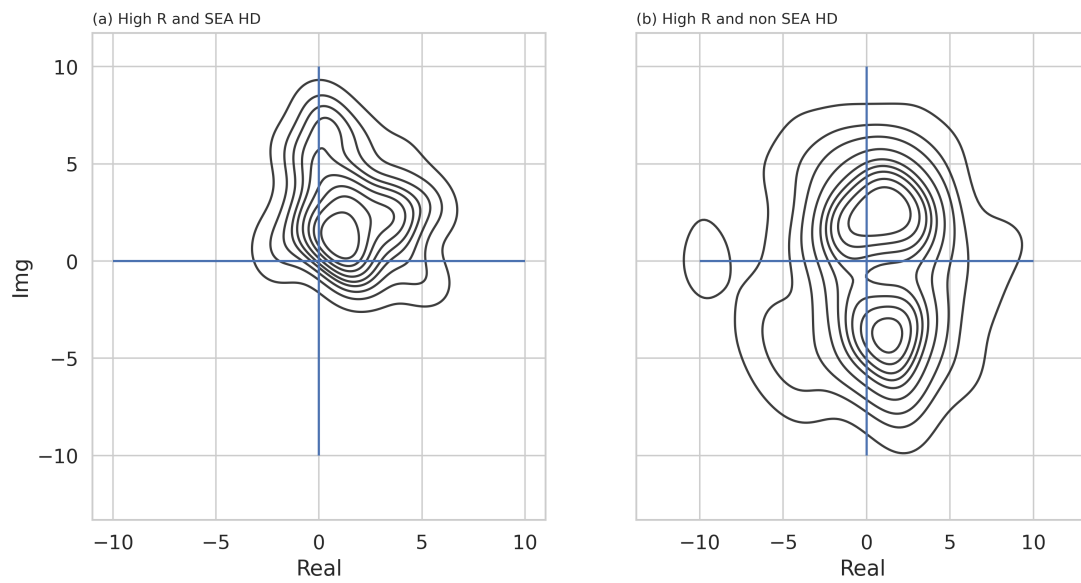


Figure 3.9: Bivariate kernel density estimate using Gaussian kernels in the complex plane of the Fourier decomposed meridional wind at 250 hPa averaged between  $35^{\circ}$  S and  $65^{\circ}$  S. Only zonal wavenumber 4 is shown for days belonging to (a) high  $R_{SEA}$  and SEA HD, and (b) high  $R_{SEA}$  and non-SEA HD.

### 3.5 Discussion

During the 2004 and 2009 SEA heatwaves, we find transient and fast-moving Rossby waves organized in wave packets, recurring in the same phase to form a ridge over SEA, thereby contributing to the persistence of the heatwave conditions. This persistence arises by recurrence, in contrast to the persistence arising from stationary weather features such as slow-moving Rossby waves (e.g., Wolf et al., 2018) or blocking anticyclones (e.g., Kautz et al., 2022). The Rossby wave packets observed during the two SEA heatwaves were not always initiated in the same area. In the 2004 case, these waves were mostly not in phase upstream of Australia, whereas in the 2009 case, they were also in phase upstream over the Indian Ocean. Blocks were observed upstream and downstream during the two heatwaves and suggests that blocks could play a role in initiating the RWPs and/or in modulating their phase. Figure B.3 presents relationship between  $R$  anomalies and the blocks in the Indian and south Pacific Oceans for DJF. Overall, our results agree with (Risbey et al., 2018) and King and Reeder (2021), who reported transient waves in the Indian Ocean preceding SEA heatwaves and transient circulation anomalies during SEA heatwaves. More specifically, we show how recurrent Rossby waves aid in the persistence of the well-known upper-level anticyclonic PV anomalies during SEA heatwaves by forming recurrent upper-level ridges.

The relevance of RRWPs for persistent SEA heatwaves documented in these two case studies is consistent with the results of the Weibull regression analysis, which reveals a significant positive statistical link between the duration of hot spells over SEA and RRWPs. PV composite for high  $R_{SEA}$  days co-occurring with SEA heatwaves shows an anticyclonic PV anomaly over SEA (Fig. 3.8), which is a typical feature of SEA heatwaves (Parker et al., 2014a; Quinting and Reeder, 2017). The PV composite also shows a wavenumber 4 pattern, where the anticyclonic PV anomalies are located upstream and downstream of blocking frequency maxima. Furthermore, the distribution of the zonal wavenumber in the complex plain indicates a preferred phasing for high  $R_{SEA}$  days part of SEA heatwaves (Fig. 3.9). The results from the Weibull regression analysis also suggests preferred phasing of the transient eddies not only over SEA but also upstream and downstream of it. Therefore, recurrent Rossby wave packets in the right phase could help to foster the anticyclonic anomalies over SEA for time periods exceeding the lifespan of an individual wave packet. Hence, the combined evidence from the literature summarized above, together with the observations from the two case studies and the results from the regression analysis, suggest a causal link between RRWPs and persistent SEA heatwaves. The proposed link works as follows: heatwaves over SEA are forced by subsidence occurring in anticyclones of SEA (e.g., Quinting and Reeder, 2017). RRWPs result in the repeated formation of these ridges over SEA and thereby contribute to the persistence of the ridges and thus, the heatwaves. However, not all SEA HD are associated with RRWPs, and hence other dynamical pathways for SEA heatwaves exist. In addition, local negative soil moisture anomalies strengthen positive temperature anomalies through increased surface sensible heat fluxes and may thereby extend the duration of heat waves (e.g., Green, 1977; Seneviratne et al., 2010; Martius et al., 2021).

A reverse causal link between surface temperature anomalies during SEA heatwaves and  $R_{SEA}$  is theoretically possible, namely that the positive surface temperature anomaly contributes substantially to the upper-level ridge and that this ridge amplification increases  $R_{SEA}$ . This causal link cannot be distinguished in our Weibull model set-up. However, model experiments from Martius et al. (2021) suggest that the influence of surface temperature anomalies over Australia on the upper-level (250 hPa) geopotential height and wind anomalies is quite small; therefore, the imprint on R-metric after the latitudinal averaging is even smaller.

### 3.6 Conclusion

We find that RRWPs are associated with a significant increase in the persistence of hot spells in the SH. In several parts of SEA, including the states of South Australia, New South Wales, Victoria, and Tasmania, longer hot spells coincide with high amplitude RRWPs (Fig. 3.3). Other regions over land where RRWPs are statistically associated with hot spell duration include South America: southern Brazil, Bolivia, and parts of Argentina and Chile.

We have demonstrated the role of RRWPs in building persistent ridges during two cases of SEA heatwaves: the 2004 and 2009 heatwaves. Both heatwaves featured RRWPs comprised of transient Rossby waves, which were in phase regionally but not hemisphere wide. Blocks were not directly observed over SEA, but the case studies suggest that blocks upstream and downstream played an important role in initiating the Rossby wave packets and modulating their phase. We further investigated the co-occurrence of RRWPs during the most persistent and extreme SEA heatwaves using the R-metric.

We find that days with  $R$  exceeding the 90<sub>th</sub> percentile, high  $R_{SEA}$  days, are associated with increased probabilities of being part of a heatwave compared to climatology. These conditional probabilities have similar magnitudes as those with remote drivers, e.g., Madden Julian oscillation (MJO), El Niño–Southern Oscillation (ENSO) (Parker et al., 2014b). However, not all high  $R_{SEA}$  days are associated with heatwaves. Further investigations suggest that those high  $R_{SEA}$  days, that are relevant for the SEA heatwaves, play a role in forming or sustaining the ridges over SEA. Such high  $R_{SEA}$  days exhibit a circumglobal zonal wavenumber 4 pattern in the PV composite and indicate a preferred phasing of the waves. The high  $R_{SEA}$  days that do not coincide with SEA heatwave days do not show preferred phasing (a ridge or a trough) over SEA. Therefore,  $R$  accompanied with information on the phasing of the wave packets could be used as a diagnostic metric for SEA heatwaves.

The following open questions remain: what is the role of blocks in initiating RRWPs and modulating their phase? The case studies and the PV composites suggest that blocking might play an important role. What is the role of background flow in setting up RRWPs and modulating their phase? The interaction of RRWPs with other well-known climate oscillation patterns such as the



ENSO and the Southern Annular Mode also needs to be investigated further. Better understanding of the interplay between these features might offer an opportunity to improve sub-seasonal forecasts during RRWP events.

### 3.7 Acknowledgments and data availability

SMA is grateful for discussions with Alexandre Tuel and for the text editing by Simon Milligan. OM and SMA acknowledge Marco Rohrer for the blocking algorithm. The authors acknowledge the European Centre for Medium-Range Forecasts (ECMWF) for producing the ERA-I dataset and the Australian Bureau of Meteorology for producing ACORN-SAT dataset. The code for blocking algorithm is available here: <https://github.com/marco-rohrer/TM2D>. The code used to calculate R-metric is available from the following in-text citation Ali and Röthlisberger (2021).



## Chapter 4

# Association between RRWPs, QRA, and blocks in the Southern Hemisphere

This chapter formed a part of the initial submission of Ali et al. (2022). The revised submission at the time of writing of this thesis was streamlined to focus on the link of RRWPs with SH hot spells and the association of RRWPs with south-eastern Australian (SEA) heatwaves (Chapter 3). Thus, the remaining study examining the association of RRWPs, QRA, and blocks in the Southern hemisphere is presented separately in this chapter. This chapter was co-authored with valuable inputs from Kai Kornhuber, Matthias Röthlisberger, Tess Parker, and Olivia Martius.

## 4.1 Introduction

Quasi-stationary anticyclones, linked to amplified and longitudinally elongated Rossby waves, have been observed in association with quasi-resonant wave amplification (QRA) events (Petoukhov et al., 2013). QRA is a hypothesized mechanism to explain non-linear wave amplification. During QRA conditions, synoptic-scale free waves are trapped in a latitudinal waveguide. In the presence of suitable thermal and orographic forcing, synoptic-scale free waves and forced waves interact, which non-linearly amplifies the wave amplitude (see Kornhuber et al. (2017b) for more details on QRA). Based on the approximations of linear Rossby wave theory, the QRA framework has so far been tested with reanalysis data and currently awaits further validation from more idealized modelling frameworks (e.g., Mooring and Linz, 2020). Quasi-stationary anticyclones, linked to amplified and longitudinally elongated Rossby waves, have been observed in association with quasi-resonant wave amplification (QRA) events.

QRA conditions have been diagnosed for several recent heatwave events: the Russian heatwave of 2010 ((Petoukhov et al., 2013)); the heatwaves of summer 2018 in the Northern Hemisphere (NH) midlatitudes Kornhuber et al. (2019). Kornhuber et al. (2017a) presented evidence from reanalysis data for QRA of wavenumbers 4 and 5 in the Southern Hemisphere (SH). QRA is one of the mechanisms suggested to foster multiple simultaneous blocking events that are linked to slow-moving amplified Rossby waves of synoptic wavenumber ( $k \geq 5$ ) (Kornhuber et al., 2017b; Petoukhov et al., 2013). However, Wirth and Polster (2021) suggest an inverse causal link by which blocking could create the waveguide structures required to identify QRA conditions. The links and potential causality between QRA and blocking remain an open question.

Transient high-frequency recurrent Rossby wave packets (RRWPs) have also been observed for some heatwave events linked to the QRA mechanism in the NH: The 1994 European heatwave identified as a QRA event in Kornhuber et al. (2017b) has also been identified as an RRWP event in Röthlisberger et al. (2019). The Russian heatwave of 2010, identified as a QRA event, is composed of RRWPs (Fig. 10 in Fragkoulidis et al., 2018). Furthermore, RRWPs linked to south-eastern Australian heatwaves SEA heatwaves, e.g., the 2004 and 2014 heatwaves (cf. Fig. 3, Fig. B.2), also had QRA conditions.

RRWPs and QRA have been studied in isolation so far. Therefore, the climatological frequency of co-occurrence of QRA and RRWPs is unknown, as are potential interactions between the two. The examples above highlight the need to assess how the transient features captured by the RRWP framework interact with stationary features, such as blocking and amplified Rossby waves that occur regionally or at a hemispheric scale. Studying the dynamical processes acting on weather timescales during QRA conditions is beneficial to uncover the potential interactions with RRWPs. Thus, this chapter addresses the following research questions:

- How do RRWP conditions relate to QRA conditions in the SH?
- How do RRWP and QRA conditions relate to blocks in the SH?

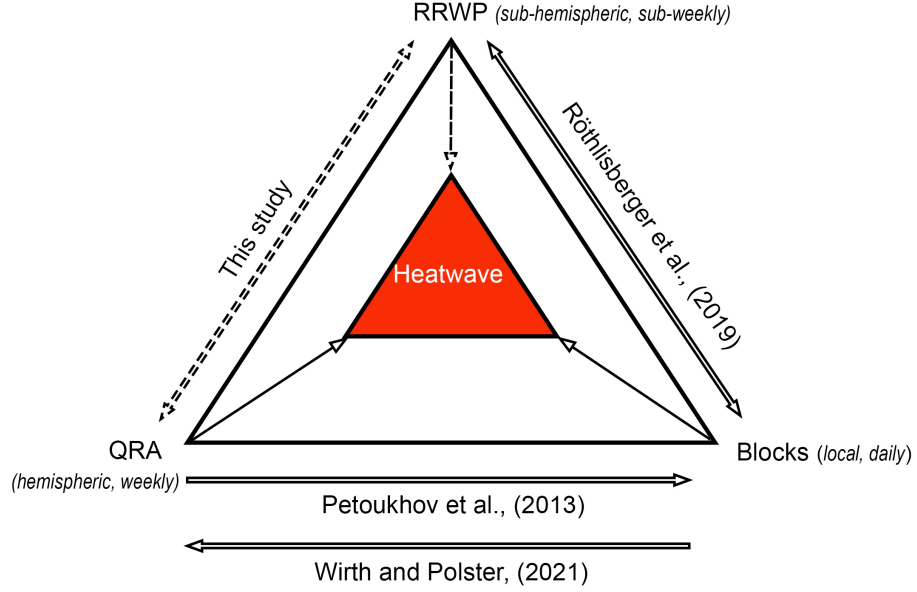


Figure 4.1: Schematic summary of the links between QRA conditions, blocking, and RRWPs with heatwaves. Solid arrows indicate links reported in the literature, and dashed lines indicate unexplored links.

We investigate the link between these dynamical frameworks from a primary RRWP standpoint in the Southern Hemisphere. We use climatological datasets for blocking anticyclones (Schwierz et al., 2004; Rohrer et al., 2018), QRA conditions (Petoukhov et al., 2013; Kornhuber et al., 2017a), and RRWPs (Röthlisberger et al., 2019; Ali et al., 2021). The data sets also allow us to investigate some of the proposed causal links discussed above and summarized in figure 4.1.

## 4.2 Method

## 4.3 Data

This study uses ERA-I Interim reanalysis data Dee et al. (2011)  $1^\circ \times 1^\circ$  spatial grid for 1979–2018 as in chapter 3. The metric  $R$  is used as calculated in Ch. 3. The blocking dataset is used as described in Ch. 3. Absolute values of isentropic Potential Vorticity (PV) are used for the composites.

### 4.3.1 QRA data

QRA events are identified using the QRA detection scheme described in Kornhuber et al. (2017b), based on ERA-I daily fields for December to February 1979–2018 at a spatial resolution of  $2.5^\circ \times 2.5^\circ$ , smoothened using a 15 day running mean. The detection scheme tests climate data for the resonance conditions defined by Petoukhov et al. (2013): the formation of a wave guide in the zonally averaged zonal wind field for a wavenumber  $k$  and the emergence of a forcing pattern of wavenumber  $m \approx k$ . Please refer to Kornhuber et al. (2017b) and Kornhuber et al. (2017a) for more details. For the co-occurrence analysis and the composites, we use the period of December to February 1979–2018, for which QRA data is available. For simplicity, days with QRA conditions are referred to as QRA days and those without as non-QRA days. 819 days out of 3520 days show QRA conditions, 576 of which show QRA with wavenumber 4. Note: Here, QRA implies that the condition of waveguide and forcing is fulfilled and a high amplitude wave is observed.

## 4.4 Results

### 4.4.1 Are RRWPs and QRA events independent?

The co-occurrence between RRWPs and QRA for several SEA heatwaves discussed in the introduction section raises the question as to what degree the two phenomena are exclusive or whether the metrics capture essentially the same flow structures but interpret them differently. Therefore, we examine the co-occurrence of high  $R$  events and QRA events on a climatological scale (December 1979–February 2018). Because QRA is a hemispheric-scale metric, we consider a zonal mean  $R$  for a representation of hemisphere-wide recurrence. However, since RRWPs can occur locally, we performed sensitivity tests using zonal max  $R$  to define high  $R$  days. The zonal max approach did not change our conclusions.

We find that 331 of 528 high  $R$  days (63%) correspond to QRA days. Conversely, 331 of 819 QRA days (40%) correspond to high  $R$  days. However, these two metrics are highly auto correlated as they use 15-day running mean fields. Thus, to test the association between the two metrics, we use every 15<sup>th</sup> observation to have independent events. The co-occurrences of the two metrics are summarized in a contingency table (Table 4.1). We test the association between high  $R$  and QRA events using a chi-square test at 99% threshold, where the null hypothesis is: there is no association between high  $R$  and QRA events. The odds ratio is used to quantify the strength of association between QRA and high  $R$  events.

The odds of a QRA event given high  $R$  is 25/11. The odds of a QRA event given no high  $R$  is 29/170. The odds ratio is thus  $(25/11)/(29/170)=13.32$ . Thus, QRA has higher odds of occurring with high  $R$  events than without high  $R$  events. The chi-square test also shows a significant association between the two, suggesting that the null hypothesis that there is no association between high  $R$  and QRA events can be rejected. We find that our test results are robust with respect to

Table 4.1: Contingency table for high  $R$  and QRA events in DJF. Note that the table only includes independent events.

	QRA	No QRA	Total
High $R$	25	11	36
No high $R$	29	170	199
<b>Total</b>	54	181	235

the starting step of the 15-day intervals.

The frequency analysis indicates a reasonably strong association between high  $R$  and QRA conditions but does not alone offer any meteorological interpretation. Therefore, we calculate composites of tropopause-level potential vorticity (PV) and zonal winds for high  $R$  and QRA days.

#### 4.4.2 How similar or different are upper-level flow conditions during RRWPs vs QRA days?

The anomaly structures for PV at 350 K and zonal wind at 250 hPa (U250) show a remarkable similarity between high  $R$  and QRA condition days: a Pearson correlation coefficient of almost 1 between high  $R$  days and QRA days for composite mean PV and composite mean U250 fields, respectively. Anomalies of PV composites with respect to the DJF climatology for both QRA and high  $R$  days (Fig. 4.2a, 4.2b) feature cyclonic PV anomalies north of New Zealand, in the Pacific Ocean, and upstream of South America. Similarly, anticyclonic PV anomalies are present in all the major ocean basins, including downstream of Australia, upstream of South America, and both upstream and downstream of South Africa. Increase in blocking frequency (crossed hatches in Fig 4.2a, 4.2b) is also seen mainly over south Pacific Ocean. Similarly, spatial features of the U250 anomalies (Fig. 4.2d, 4.2e) show a striking similarity between the two composites, with stronger westerlies over the South Atlantic Ocean and weaker zonal winds over SEA. However, a key difference is visible upstream of South America, where high  $R$  days show positive U250 anomalies north and south of the climatological jet core and negative U250 anomalies at the climatological jet core, thus favouring a meandering jet. The major features in the spatial distribution of anomalies for high  $R$  days are robust with defining high  $R$  days with zonal maximum  $R$  values.

Subsequently, we compare the sample of QRA days exclusive of high  $R$  days with those of high  $R$  exclusive of QRA days for PV and U250 fields respectively. The null hypothesis tested is that the two samples belong to the same distribution. A two-sample Kolmogorov–Smirnov (K–S) test at 5% threshold is used to evaluate the null hypothesis with maximum FDR at 10%. The resulting significant area, where null hypothesis is rejected, is shown with dotted hatches (Fig. 4.2c, 4.2f).

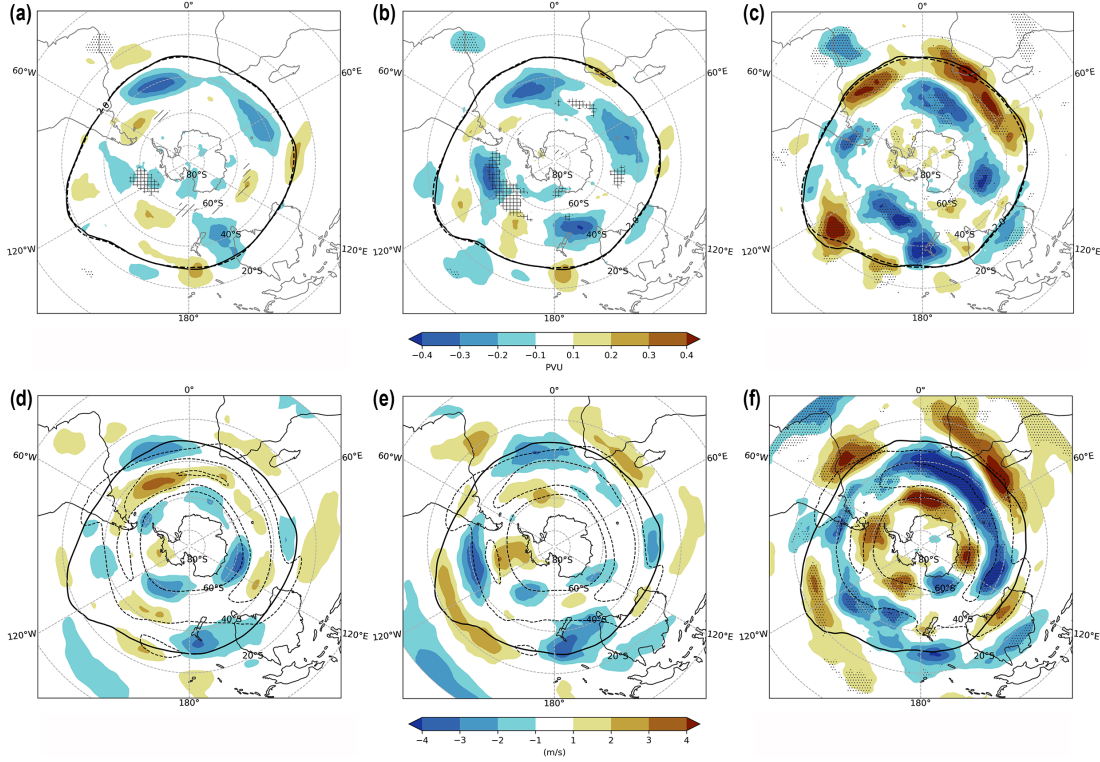


Figure 4.2: Anomalies of composite mean field with respect to DJF climatology for QRA (left), high  $R$  (middle). Right column show the difference of mean fields between QRA but non-high  $R$  days and high  $R$  but non-QRA days (right). (a), (b), and (c) show PV anomalies at 350 K isentrope. (d), (e), and (f) show zonal wind ( $U$ ) anomalies at 250 hPa ( $\text{ms}^{-1}$ ). Dashed contours in (d), (e) show isolines of mean  $U$  at 20, 30, 40  $\text{ms}^{-1}$ . (f) show DJF mean  $U$  isolines. The solid contour in (a), (b) shows mean 2PVU at 350 K isoline for the respective variable and in (c) shows the same for QRA but non-high  $R$  days. The dashed contours in (a), (b), (c) show the 2PVU at 350 K contour for DJF mean climatology. Crossed (lined) hatches in (a), (b) show areas where blocking frequency anomalies (%) with respect to DJF climatology is greater (less) than 2 %. Dotted hatches in (c) and (f) show significant regions tested using  $K$ - $S$  test at 5% threshold.

Significant areas difference in composite mean PV fields between the two samples include cyclonic PV anomalies over parts of Brazil, central Australia, and Pacific Ocean. The difference in composite mean U250 fields suggests strengthening of the westerlies and narrowing of the climatological jet (dotted isolines in Fig. 4.2f) over all the three ocean basins for QRA days exclusive of high  $R$  days compared to high  $R$  days exclusive of QRA.



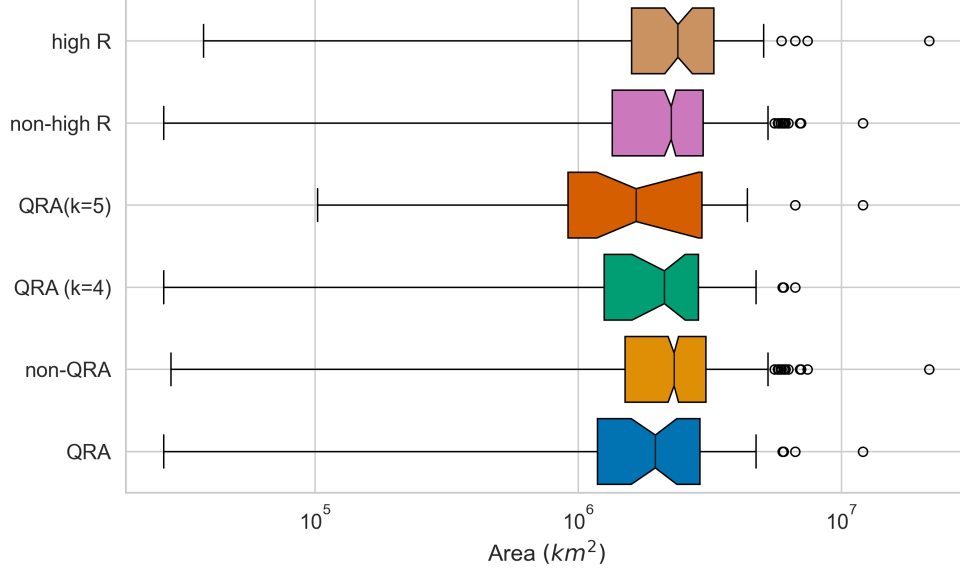


Figure 4.3: Box plots compare area ( $\text{km}^2$ ) of atmospheric blocks for various categories shown in the legend. The box shows 25<sup>th</sup> ( $Q1$ ) and 75<sup>th</sup> percentile ( $Q3$ ), with the line in the middle indicating median. The length of the box represents interquartile range ( $IQR$ ). The upper (lower) whiskers are 1.5 times the  $IQR$  plus (minus)  $Q3$  ( $Q1$ ). The notches are calculated as  $\text{median} \pm 1.57 \times IQR/(\sqrt{n})$  where  $n$  is the number of data points.

#### 4.4.3 Does blocking area increase during high $R$ or QRA conditions?

To analyse whether high  $R$  or QRA conditions increase the area of the blocks, we compare the blocks between 40° S and 70° S. First, the blocking area for each unique block is extracted at the time of maximum amplitude of PV and characterized with respect to high  $R$  or non-high  $R$  and QRA or non-QRA conditions. The sample size for each category in the same order is 86, 445, 101, and 421. For the 101 blocks with QRA days, 68 and 33 samples belong to QRA with wavenumber 4 ( $k4$ ) and QRA with wavenumber 5 ( $k5$ ), respectively.

Box plots of the blocking area under high  $R$  days show a marginally higher median than non-high  $R$  days whereas the blocking area under QRA days shows a marginal decrease in median compared to blocks with non-QRA days. The notches in the box plot give a rough estimate of whether the medians are significantly different from each other. We did not find a significant difference in the median area of blocks for either the case of high  $R$  vs non-high  $R$  or QRA vs non-QRA days (Fig 4.3). The significance was evaluated using a Mann–Whitney U test, a non-parametric test which does not require the samples to be normally distributed, using a two-sided hypothesis at 5% significance level.

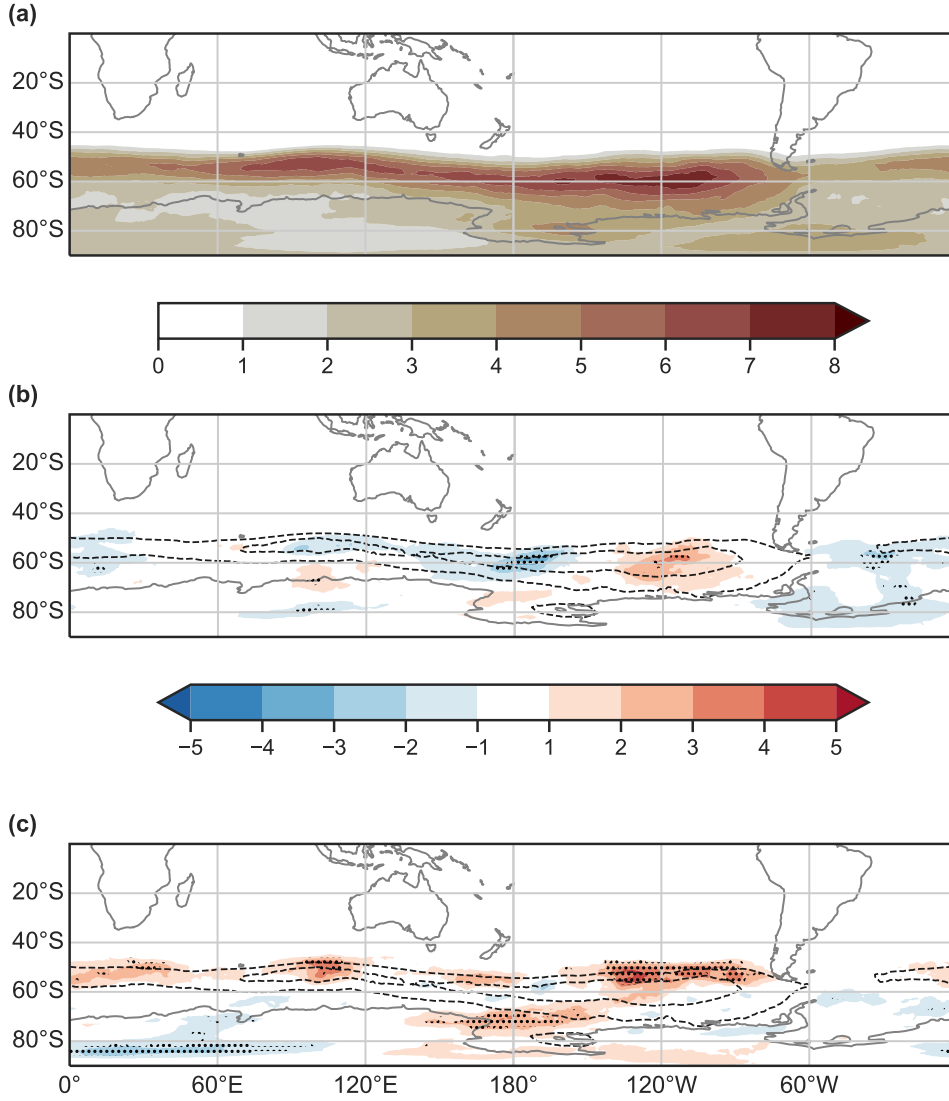


Figure 4.4: Blocking frequency (%) for (a) DJF, In (b) difference between the mean blocking frequency (%) for QRA days and (a), and in (c) same as (b) but for high  $R$  days and (a). Dashed lines in (b) and (c) show DJF mean blocking frequency contours drawn at 4, 6, and 8%. Dotted hatches in (b) and (c) show grid points with statistically significant difference in the composite mean to the mean of the sample in (a) assessed using a Mann–Whitney  $U$  test with FDR at 5%.

#### 4.4.4 How are blocks spatially distributed for high $R$ and QRA days?

Mean blocking frequency for high  $R$  days (Fig. 4.4c) shows a statistically significant increase in blocking frequency in DJF mainly over parts of two ocean basins: upstream of South America in the Pacific Ocean, and upstream of Australia in the Indian Ocean. These are also the regions where blocking frequency is highest in the DJF climatology (Fig. 4.4a). Other areas with a sig-

nificant increase include part of the Antarctic Sea ( $180^\circ$  W), south of Africa, whereas a significant decrease is observed over parts of Antarctica. The significance was assessed using Mann–Whitney U test, which assesses the null hypothesis that distribution of blocks under high  $R$  (QRA) days and that of DJF climatology are equal. For QRA days (Fig. 4.4b), there is a significant decrease in blocking frequency over south of Australia and New Zealand, south of Africa, and over parts of the south Atlantic Ocean, which was not seen for high  $R$  days. In contrast, the region upstream of South America shows an increase similar to high  $R$  days. Although most of the grid points for QRA days (Fig. 4.4) are not statistically significant, the overall decrease in blocking frequency is consistent with the results in Fig. 4.3, which show a slight decrease in the median blocking area for QRA days.

## 4.5 Discussion

We first summarize key criteria used in the objective identification of the weather features, blocks and RRWPs, and the QRA mechanism. The defining spatial and temporal characteristics of blocks, QRA, and RRWPs used in their automatic detection algorithms are summarized in Table 4.2. The zonal spatial scale of the structures increases from regional to basin-wide for blocking, through regional, basin-wide to semi-hemispheric for RRWPs, to hemispheric for QRA.

RRWPs can be regional, basin-wide, or semi-hemispheric in spatial extent. Yet, a zonal-mean approach finds that 40% of high  $R$  days coincide with QRA days. This is partly because a regionally amplified pattern can project on zonal-mean fields. For example, we found a high correlation between the high  $R$  days defined with zonal means and with the high  $R$  days defined with zonal-maximum  $R$  fields. Moreover, a recurrent transient wave pattern can appear as a quasi-stationary signal when averaged over time. Furthermore, amplified Rossby waves may influence the metrics used here for objectively detecting blocking, RRWPs, and QRA. For example, the amplified Rossby waves during the 2004 SEA heatwave (Ch. 3, Fig. 3.4), aided by recurrence, resulted in high  $R$  values, corresponded regionally to blocking, and were identified as a QRA event. These amplified waves were clearly composed of recurring transient waves with nonzero phase velocity.

Table 4.2: A comparison of the criteria used to automatically identify blocks, RRWPs, and QRA.

Characteristics	Blocks	RRWPs	QRA
Algorithm	Schwierz et al. (2004)	Röthlisberger et al. (2019)	Kornhuber et al. (2017b)
Input variable	PV (vertically averaged between 500-150 hPa)	Wavenumber filtered V at 250 hPa	Zonal mean U at 300 hPa for waveguide; thermal, orographic forcing
Presence of waveguide	No	No	Yes
Wavenumber filtering	No	$k = 4$ to 15	Focus on $k \geq 4$
Persistence criteria	Minimum 5 days	14-day running mean	15-day running mean
Spatial scale observed	Region to basin-wide	Regional, basin-wide, or semi-hemispheric	Hemispheric

However, it should be noted that merely amplified transient Rossby waves typically do not lead to large  $R$  values because their signal in meridional wind fields averages out in the bi-weekly mean. Indeed, in most cases, recurrence of multiple distinct synoptic-scale wave packets with similar phasing is required to generate large  $R$ .

The link between high  $R$  and QRA events is not only reflected in high co-occurrence but also in spatial patterns. The upper-level mean PV composites for QRA and high  $R$  days show a remarkably similar pattern (Fig. 4.2). The pattern is statistically indistinguishable even though the zonally averaged  $R$  metric does not explicitly include any phase or location restriction. This implies that high  $R$  events in the SH co-occurring with QRA have a particular phase preference. The PV anomaly pattern exhibits a wavenumber 4 structure in the extratropics and a wavenumber 5 to 6 pattern in the subtropics (Fig. 4.2).

Hence, the question is whether RRWPs and QRA may in some cases be the same structures observed through different lenses, i.e., with diagnostics from temporal, spatial, and other filters. The similarity in the composite PV anomalies during high  $R$  and QRA days point to the same mechanisms being relevant for the organization of the RRWPs, the establishment of QRA conditions, and/or interactions between the two. The fact that not all high  $R$  and QRA days overlap – 37% (197 days) of high  $R$  days do not feature QRA conditions – may be explained by the different longitudinal scales used by the detection algorithms. Another reason could be the forcing condition required for QRA events; not all high amplitude waves are detected by QRA because QRA needs the presence of a waveguide as well as thermal and orographic forcing ((Petoukhov et al., 2013; Kornhuber et al., 2017a). Moreover, the composite PV for QRA days exclusive high  $R$  days showed significant differences to high  $R$  days exclusive of QRA over several key regions: parts of Brazil, central Australia, and the south Pacific Ocean (Fig. 4.2c).

QRA events require the presence of a waveguide. The waveguide is detected in the zonal mean profiles of the two-week running mean zonal-mean zonal wind. Wirth and Polster (2021) question this approach stating that highly amplified flow, for example, the flow associated with atmospheric blocking, can affect the zonal mean profile in a way that it leads to spurious waveguide detection compared to a zonalised background flow that excludes the effects of the eddies. They demonstrated their approach with case studies for the NH heatwaves where QRA was observed. However, their study did not show whether their zonalised background flow can capture a waveguide in a non-idealized flow. It may be that the large-amplitude eddies may be essential in aiding the waveguide formation in non-idealized flows. We do indeed find a high co-occurrence of highly amplified flow (high  $R$  events) and QRA events; however, we also find a stronger, more zonal flow during QRA-days absent of high  $R$  days compared to high  $R$  days absent of QRA days (Fig. 4.2). Hence, it may be that some of the QRA-events analysed here are sensitive to the exact definition of the background flow. Furthermore, the interpretations on this matter are also influenced by how the background state is defined, which is not a physically measurable state and thus, has various interpretations (White et al., 2022).

## 4.6 Conclusions and Outlook

In this chapter, we answered the following research questions:

- How do RRWPs conditions relate to QRA conditions in the SH? We found a strong and statistically significant association between RRWPs and QRA events (Table 4.1); QRA events are more likely to occur with RRWPs than without RRWPs. We also showed that 40% of QRA days also feature high  $R$  days, indicating RRWP conditions, which implies that QRA conditions can often feature RRWPs. We also found similar flow conditions in the composite mean upper-level fields during QRA and high  $R$  days. However, 60% of QRA days do not feature high  $R$ . Significant differences in flow conditions for QRA days exclusive of high  $R$  days with high  $R$  days exclusive of QRA days show cyclonic PV over parts of Brazil, central Australia, and south Pacific Ocean, and increased westerlies over all the three ocean basins.
- How do RRWPs and QRA conditions relate to blocks in the SH? We found an insignificant increase in the median area of blocks for high  $R$  vs non-high  $R$  in the SH and a slight decrease for QRA days vs non-QRA days (Fig. 4.3). We looked further into how blocks are spatially distributed for high  $R$  and QRA days, respectively (Fig. 4.4). Important differences can be seen between the two in blocking frequency over the Indian Ocean, south of Australia and New Zealand, south of Africa, and in the south Atlantic Ocean, whereas both show an increase in blocking frequency over the south Pacific Ocean.

However, several questions that relate to the interaction between blocking, RRWPs and QRA remain open. Does blocking modulate the phase of Rossby waves and thus help in establishing RRWPs, or is the causal link instantaneous? What is the role of blocks during the QRA conditions, and why do we see a difference in blocking frequency between RRWPs and QRA conditions (Fig. 4.4)? The role of QRA in the recurrence of Rossby waves also needs to be investigated further. Investigating the role of background flow is not straightforward because defining it is a formidable problem (White et al., 2022). The interaction of RRWPs with other well-known climate oscillation patterns also needs to be investigated further. The improved understanding between the interplay of these features will help to reduce model biases and improve our confidence in future climate projections.



## Chapter 5

# Drivers of Recurrent Rossby Waves in the North Atlantic using Causal Networks

### 5.1 Introduction

Synoptic-scale Rossby waves at upper levels spawn and steer mid-latitude weather systems (e.g., Rhines, 2015). They can lead to persistent surface weather when they exhibit particularly low phase speed, i.e., become quasi-stationary (e.g., Blackburn et al., 2008; Wolf et al., 2018). However, persistent surface weather can also arise from transient (i.e., propagating) Rossby waves recurring in the same phase at one location over days to weeks (Röthlisberger et al., 2019; Ali et al., 2021). Such recurrence of transient Rossby waves was observed during several episodes of persistent surface weather, e.g., the winter seasons of 1985 and 2013-14 (Hoskins and Sardeshmukh, 1987; Davies, 2015); the Russian heatwave of 2010 (Fragkoulidis et al., 2018), the southeastern Australian heatwaves in 2004 and 2009 (Ali et al., 2022); and the anomalous precipitation of April-May 1984 over the Iberian Peninsula (Ali et al., 2021).

Given the importance of the recurrence of Rossby waves in generating persistent weather for individual cases, Röthlisberger et al. (2019) defined a metric  $R$  to capture these recurring Rossby waves and termed this phenomenon as Recurrent Rossby Wave Packets (RRWPs). The metric  $R$  attains large values when the synoptic-scale waves amplify in the same phase. Using  $R$ , Röthlisberger et al. (2019) showed that RRWPs are statistically linked to the duration of persistent hot spells in summer and persistent cold spells in winter over the mid-latitudes. RRWPs also have a significant association with hot spells in the Southern Hemisphere (Ali et al., 2022) and are also associated with increased duration of persistent dry and wet spells across the globe (Ali et al., 2021). Given the relevance of RRWPs for weather persistence, it is worthwhile to investigate which processes drive RRWPs. This study uses theory-guided causal networks (CNs) (Runge et al., 2019a) to investigate the causal drivers of RRWPs, hereafter –driver– is used in a –causal– sense. Therefore, processes that might lead to RRWPs are summarized next to motivate the

choices of the potential causal drivers used later in the CN.

During RRWP periods several transient Rossby wave packets recur in the same phase at one location. This requires mechanisms that influence the phase and potentially the formation of the waves. Atmospheric blocks modulate the phase of Rossby waves and may initiate Rossby waves downstream. Indeed, blocks are closely associated with RRWPs. Composites of  $R$  values prior to, during, and after blocks in the North Atlantic and the North Pacific basins show positive  $R$  anomalies upstream and downstream of blocks (Röthlisberger et al., 2019). Rossby waves frequently break downstream of blocking and form troughs (e.g., Altenhoff et al., 2008). Through this process, blocks can influence the phase of Rossby waves downstream of the block. A feedback may exist between RRWPs and blocks. RRWPs, which are composed of transient eddies, can help to sustain blocks by advecting low Potential Vorticity (PV) air (e.g., Shutts, 1983; Hoskins and Sardeshmukh, 1987). Furthermore, blocking onset can be forced by transient eddies (e.g., Ma and San Liang, 2017).

Wave propagation and the meridional displacement of isentropic PV contours are modulated by the background flow (Hoskins and Ambrizzi, 1993; Hoskins and Woollings, 2015). Meridional undulations of the PV contours become larger in weaker zonal flow (Hoskins and Woollings, 2015). Nakamura and Huang (2018) showed that the jet stream has a wave activity flux capacity. A block can form when the wave activity flux capacity is exceeded. Therefore, we expect a close association between the background flow, blocks, and RRWPs.

Transient Rossby waves can be triggered by mid-latitude diabatic heating (e.g., Grams et al., 2011; Röthlisberger et al., 2018) or active tropical convection (e.g., Davies, 2015) and subsequently amplified by baroclinic instability (Charney, 1947; Pierrehumbert and Swanson, 1995). RRWPs can form if the wave initiation process is persistent in space and time over a week and more. Active tropical convection is persistent enough to act as an RRWP initiator potentially. Several model and observational studies have shown tropical and mid-latitude teleconnections whereby active tropical convection can act as a Rossby wave source (e.g., Sardeshmukh and Hoskins, 1988; Hoskins and Ambrizzi, 1993; Trenberth et al., 1998; Stan et al., 2017). In the presence of a strong and narrow jet, the resulting Rossby waves are ducted into the jet waveguide and propagate downstream along the jet under linear dynamics. Several studies have suggested this teleconnection to be a precursor to North Atlantic weather regimes (e.g., Cassou, 2008; Lin et al., 2009; Straus et al., 2015; Davies, 2015; Fromang and Rivière, 2020). Check Stan et al. (2017) for a detailed review. Active tropical convection can also influence via non-linear Rossby wave dynamics in the Pacific with effects downstream over the Atlantic. The Madden-Julian Oscillation (MJO) modulates Rossby wave breaking and blocking in the Pacific basin (e.g., Fig. 9 Moore et al., 2010; Cassou, 2008). Using MJO as a predictor at 4 to 12-day lag improves the predictability of North Atlantic weather regimes (Cassou, 2008). Furthermore, recurving tropical cyclones undergoing an extratropical transition can be linked to Rossby wave amplification downstream (Grams et al., 2011; Quinting and Jones, 2016; Riboldi et al., 2019; Keller et al.,



2019). Barton et al. (2016) describe an RRWP episode over Europe that was initiated with the recurrent extratropical transition over the Atlantic.

To study the relevance of the mechanisms discussed above as drivers for RRWPs we use causal networks. Many recent studies have advocated the use of causal networks (CNs) for identifying causal links rather than the standard practices of regression and composite analyses often used in climate sciences (Barnes et al., 2019; Runge et al., 2019b; Kretschmer et al., 2021). These networks help to distinguish direct effects from indirect effects and prevent misleading identification of causal connections (Pearl, 2009). However, the variables used in a causal network should be carefully selected based on the physical understanding of the system (Di Capua et al., 2020; Saggioro and Shepherd, 2019). This paper follows that approach and present composites for RRW events over the North Atlantic to identify potential actors that are subsequently tested for causal associations in the CNs framework.

This study of the drivers of RRWPs over the North Atlantic is divided into winter and summer seasons, respectively. We present the analysis for winter first, starting with the results from the composite maps of the meteorological variables for a set of RRWP events. Theory-guided links outlined above motivate the choice of variables used in the composites. The composite maps are used to understand the flow situation during RRWPs events and help us to identify indices that form the potential causal processes (actors). Then, the potential actors identified from the composite maps are tested in a causal network framework on a climatological time scale. We repeat the same steps for summer. The key drivers of RRWPs, and the similarities and the differences between the two seasons are discussed further. The section 5.3 presents results, section 5.4 discusses the results, and section 5.5 summarizes the main conclusions of this study.

## 5.2 Method

### 5.2.1 Dataset

This study uses the ERA5 data, the fifth generation atmospheric reanalysis produced by the European Centre for Medium-Range Weather forecasts (ECMWF) (Hersbach et al., 2020). ERA5 was downloaded at  $0.5^\circ$  by  $0.5^\circ$  spatial resolution and six hourly temporal resolution for the period 1979 to 2018. For composite analysis, the data were resampled to  $1^\circ$  by  $1^\circ$  spatial and 1-day mean temporal resolution.

Meridional wind at 250 hPa is used to calculate the metric  $R$  following Röthlisberger et al. (2019). Zonal wind field,  $U$  at 250 hPa is used to calculate background zonal wind, hereafter BU, in the following way: We extract the portion of the zonal wind associated with the zonal wavenumbers,  $k=0$  to  $k=3$ , by decomposing  $U$  along the longitude at each grid following the method in Zimin et al. (2003). That is, the separation between background and eddy components of the flow is performed via the spatial-scale rather than over time. This separation of background and eddy

components is beneficial in the context of this study in two ways. Firstly, synoptic experience suggests that transient eddies do not propagate purely zonally, but rather follow the large-scale flow pattern established by stationary (i.e., low wave number) waves, which motivates a separation in scale. Secondly, our decomposition results in a smooth and slowly varying BU field, which also captures the key structure of a BU field obtained, e.g., by a running mean (not shown). Stream function (SF) is calculated at 250 hPa using the zonal and meridional wind components at each time step.

The Rossby wave source (RWS) can be used to examine sources of vorticity associated with tropical convection Sardeshmukh and Hoskins (1988). Active tropical convection results in strong upper tropospheric divergence in the tropics and convergence in the subtropics, which acts as a RWS. The RWS can be insensitive to the location of tropical heating due to climatological stationary planetary waves and associated jet streams (Trenberth et al., 1998). The RWS ( $\text{s}^{-2}$ ) can be calculated from the absolute vorticity,  $\zeta$  and the divergent wind  $v_\chi$  as in Sardeshmukh and Hoskins (1988):

$$RWS = -\zeta \left[ \frac{\partial u}{\partial x} + \frac{\partial v}{\partial y} \right] - v_\chi \cdot \nabla \zeta \quad (5.1)$$

where the first term in Eq. 5.1 describes the effects of vortex stretching, and the second term describes the advection of absolute vorticity by the divergent wind  $v_\chi$  (O’Kane et al., 2016; Trenberth et al., 1998). RWS is larger poleward of diabatic heating source and in jet stream regions. We calculate RWS on a daily timescale as in O’Kane et al. (2016) and calculate the anomalies to the bootstrap sample mean explained next.

The maximum Eady growth rate, EGR is used as a measure of baroclinicity (Lindzen and Farrell, 1980) at lower levels in the atmosphere. The EGR is calculated at 700 hPa using the equation as in Simmonds and Lim (2009):

$$\sigma_E = 0.3098 \frac{|f| \left| \frac{\partial U(z)}{\partial z} \right|}{N} \quad (5.2)$$

where  $f$  is the Coriolis parameter,  $N$  is the Bunt-Väisälä frequency and  $U(z)$  is the vertical profile of the zonal wind component and  $z$  being the vertical coordinate.  $\frac{\partial U}{\partial z}$  is calculated using  $U$  at 550 hPa and 850 hPa .

Outgoing Longwave Radiation (OLR) ( $\text{Wm}^{-2}$ ) is used identify convection over the tropics. Note that the ECMWF convention for vertical fluxes is positive downwards; however, we use absolute values from the OLR data. In this case, convection is shown by negative OLR anomalies indicating lower OLR due to colder cloud tops.

Atmospheric blocks are identified from persistent anticyclonic PV anomalies vertically averaged between 500 hPa and 150 hPa. The algorithm of Rohrer et al. (2020) is used which is based on the

detection scheme of Schwierz et al. (2004). The following parameters are used in the detection scheme: PV threshold of 1.3 PVU; persistence criterion of 5 days; and a minimum overlap of 0.7 between two consecutive time steps. The blocking dataset is only used for 40° N to 90° N

### 5.2.2 Selecting high $R$ events

We focus on the North Atlantic basin since  $R$  has climatologically higher values over the two ocean basins in the Northern Hemisphere and is relevant for persistent weather over Europe (Röthlisberger et al., 2019). Based on earlier case studies, RRWP events over the North Atlantic can extend into western Europe (Röthlisberger et al., 2019; Ali et al., 2021). Therefore, as a first step, the daily time series of the metric  $R$  is averaged longitudinally over 50° W and 10° E to include parts of the North Atlantic and the western Europe. To identify high  $R$  events, a peak over threshold approach is employed for the months of December-January-February (DJF) and June-July-August (JJA). An event is defined as consecutive days that exceed a selected threshold. Two events separated by less than 14 days are merged to have a set of independent events. The threshold starting with 0.85 quantile of  $R$  is increased or decreased iteratively until a minimum number of 30 events is obtained for each season. In this way we identify a set of 30 long-lasting and amplified North Atlantic RRWP episodes for both the seasons.

The sets of high  $R$  events are used to create composite mean maps of meteorological variables at daily time lags prior to and after the onset of the event ( $t=0$ ). The anomalies at each time lag are calculated relative to a bootstrap sample mean. The bootstrap sample mean is calculated individually at each time lag for a given variable by generating 10,000 random samples. These samples are constructed by selecting random dates. The process of generating random dates is the following. The years are randomly generated between 1980 and 2018. The day is randomly generated such that it is within  $\pm 5$  day of the respective day-of-year for which the samples are generated. The bootstrap samples are also used to calculate respective  $p$  values. At this stage, a  $p$  value threshold is not set and different  $p$  value contours are displayed to identify regions of interest and formulate theory-guided causal hypothesis for the actors of interest. Univariate time series, later referred to as actors, are created by averaging over the selected regions of interest emerging from the composites to test the causal hypotheses in a graphical network framework. The composite maps thus are used to identify potentially important synoptic features during high  $R$  events, whose causal effect on  $R$  is subsequently examined using the causal network framework.

### 5.2.3 Causal Networks

The Causal Networks (CNs) used here use conditional independence-based learning algorithms to construct a graph-based network of dependent and independent variables. The dependent variables are linked directly in the graph, with a line called edge. More specifically, we use the Peter and Clark (PC) momentary conditional independence algorithm, PCMCI (Runge, 2018). A short description of the PCMCI algorithm is provided below based on Di Capua et al. (2020);

Kretschmer et al. (2016); Runge et al. (2019a). The readers are encouraged to check those papers and the supplementary materials in Runge et al. (2019a); Di Capua et al. (2020) for further details.

The PCMCI algorithm consists of two stages: first, a PC condition-based selection stage that selects parents of each variable based on iterative conditional independence (CI) tests; second, the MCI stage, which removes spurious links due to auto-dependencies in the time series and orients the significant links. The mathematical equations comprising the two stages are given below.

Let  $\mathbf{X}$  be a set of individual, detrended, time dependent variables (or actors) such that,  $\mathbf{X} = (X_t^1, X_t^2, \dots, X_t^N)$ . Let  $\mathbf{X}_t$  denote the present time step for the set of time series of the variables. Then,  $\mathbf{X}_t^- = (\mathbf{X}_{t-1}, \mathbf{X}_{t-2}, \dots)$  denote the past processes of  $\mathbf{X}_t$ .

Let  $\mathcal{P}(X_t^j)$  denote the causal parents of variable  $X_t^j$ . The PC stage implements iterative independence tests given a condition  $\mathcal{S}$ , where  $\mathcal{S}$  is chosen from each variable in  $\mathcal{P}(X_t^j)$ . Thus, to check if  $X_t^i$  at a lag of  $\tau$  drives  $X_t^j$ , i.e.,  $X_{t-\tau}^i \rightarrow X_t^j$ , the PC stage tests for:

$$X_{t-\tau}^i \perp\!\!\!\perp X_t^j \mid \mathbf{X}_t^- \setminus \{X_{t-\tau}\} \quad (5.3)$$

where,  $\mathbf{X}_t^- \setminus \{X_{t-\tau}\}$  denote that the algorithm does not condition on the past of the multivariate process  $X_{t-\tau}^i$ . The variables for which eq. 5.3 holds true are dropped from the set of potential parents  $\mathcal{P}(X_t^j)$ . In the next steps, the dimensions of the tests is increased to more dimensions, starting with  $\mathcal{S}$  containing two variables, that results in reduced set of parents after the CI tests. The dimension of  $\mathcal{S}$  is increased further to three, four variables, and so on resulting in further reduced sets of variables. The algorithm converges until no more conditions can be tested. Thus, each actor in  $X_t^j$  has an estimate of parents  $\mathcal{P}(X_t^j)$  at the end of the PC stage and goes into the MCI step.

The MCI stage conditions simultaneously on both sets of parents of the parents of  $X^j$  and  $X^i$ . Thus, to test for  $X_{t-\tau}^i \rightarrow X_t^j$ , MCI tests for:

$$X_{t-\tau}^i \perp\!\!\!\perp X_t^j \mid \mathcal{P}(X_t^j) \setminus \{X_{t-\tau}^i\}, \mathcal{P}(X_{t-\tau}^i) \quad (5.4)$$

After passing the MCI test, we obtain the final set of parents for each actor in  $\mathbf{X}$ . The strength of the correlations obtained after the MCI stage can be used as a measure of the causal strengths and the model-output ranks the causal actors on this basis (Runge et al., 2019b). See supplementary material of Runge et al. (2019b) for detailed explanation of PCMCI and other variants available.

The CNs obtained from the PCMCI rests on several assumptions (see Runge, 2018; Runge et al., 2019b). One key assumption is that all the relevant actors are included in the CN, although Runge et al. (2019b) stated that this assumption can be relaxed. However, this implies that the causal links obtained from the CN are obtained relative to the set of actors used in the model

Time	-3	-2	-1	0	1	2	3	4
k=0			↓	↓	↓	↓	↓	↓
k=1				↓		↓	↓	↓
k=2					↓			↓

Figure 5.1: Illustration of the time series used for the CNs. First row shows the 3-day running mean time series, where the red rectangle shows the 3-day centered running mean window. Three time series of 3-day interval are created based on the starting step of the interval, where "k" represents the starting step. The model using k=1 time series is the main model presented here. The other two models, using k=0 and k=2, are used to check the robustness of the CNs.

and the links maybe sensitive to adding more actors (Di Capua et al., 2020). Hence, the causal links obtained should be interpreted as causal relative to the set of actors included. Therefore, it is vital to construct the networks based on process knowledge. Hence, we use composite maps of various variables prior to and during high  $R$  events to formulate theory-guided hypotheses and select actors of interests for the CNs.

Although, PCMCI works well for highly auto-correlated time series (Runge et al., 2019b), high auto-correlation decreases the detection power of the algorithm and may give rise to spurious links. Most of the time series used here have high auto-correlation at daily time-scale. To decrease the auto-correlation, we use 3-day interval time series. The robustness of 3-day intervals was tested by Meyer (2022). First, the time series of the variables are resampled using a 3-day centered running mean window (Fig. 5.1) and detrended with a linear fit. We keep the seasonality in the time series as we construct models separately for winter and summer. Based on the starting step of the 3-day interval, two additional time series are created as shown in figure 5.1 are used for sensitivity tests. The CNs using time series k=1 in figure 5.1 is presented in the results. Appendix C and D show the significant links for  $R$  using the time series k=0 and k=2.

PCMCI can be combined with a variety of CI tests. We use the Partial Correlation CI test as in Kretschmer et al. (2016); Di Capua et al. (2020), but it can only capture linear dependencies. Refer to (supplementary material S 4.1 Runge et al., 2019b) for more details. The hyper-parameters used for the CNs are a maximum time lag,  $\tau_{max} = 15$  days and an  $\alpha = 0.05$  in the CI tests. PCMCI is combined with false discovery rate controls (Benjamini and Hochberg, 1995) to adjust the  $p$  values resulting from the MCI stage.

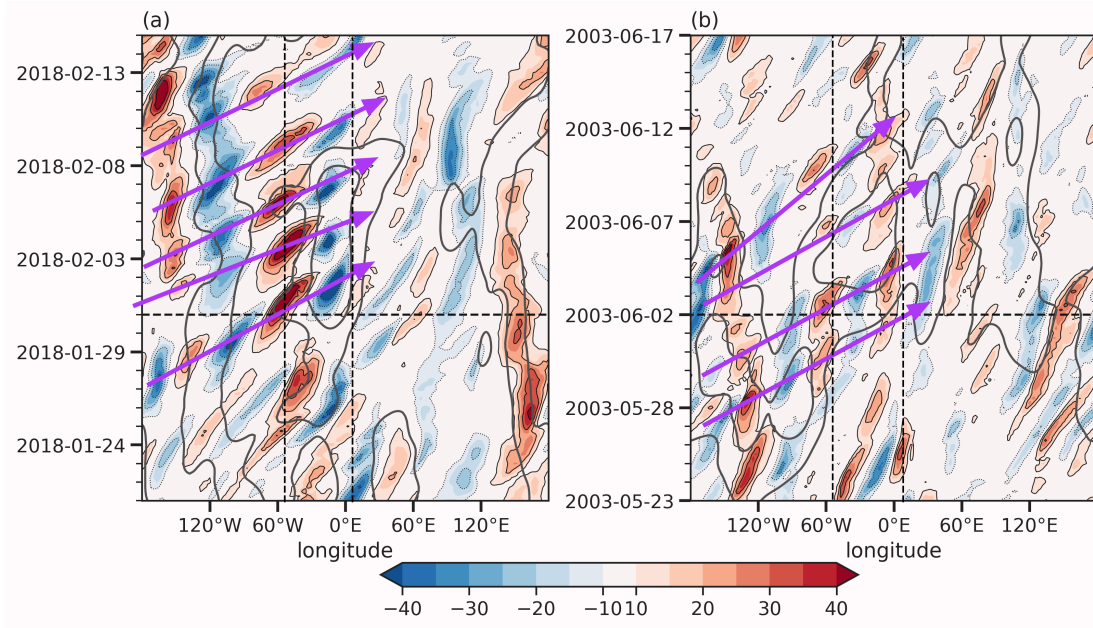


Figure 5.2: Hovmöller diagrams show two examples of high  $R$  events in (a) DJF and (b) JJA. Filled contours show meridional wind at 250 hPa in  $\text{ms}^{-1}$  averaged between  $35^\circ \text{N}$  and  $65^\circ \text{N}$ . Black contours show  $R$  values at 8 and  $12 \text{ ms}^{-1}$ . Dashed horizontal lines show the starting day of the respective events and vertical lines show the study area over the North Atlantic. Magenta arrows mark the Rossby wave trains.

## 5.3 Results

### 5.3.1 Example high $R$ event: January 2018

In winter 2018-19 a high  $R$  event occurred over the Atlantic basin (Fig. 5.2, high  $R$  contours). The event started on 31 January 2018 and lasted for 28 days. It was composed of a series of transient RRWPs that amplified in the same phase over the Euro-Atlantic sector. The Rossby wave trains formed upstream of the Atlantic over North America and the eastern Pacific (Fig. 5.2). Downstream of Asia, in the western Pacific, recurrence was also present.

Ten days prior to the start of the event ( $t=0$ ), Figure 5.3a shows positive background zonal wind (BU) anomalies over central North America and the Atlantic (roughly  $40^\circ \text{N}$  to  $50^\circ \text{N}$ ). A block formed at  $t=-4$  along the east coast of North America (Fig. 5.3b). The block moved downstream to the North Atlantic in the following days ( $t=-1$  day in Fig. 5.3c). The block over the North Atlantic was associated with a decrease in BU over the Atlantic ( $40^\circ \text{N}$ ). Simultaneously, the core of the BU shifted northward to the southern tip of Greenland. Overall the BU shifted northward when comparing  $t=-10$  to  $t=-1$  day.

Motivated by the extratropical-tropical teleconnection summarized in the introduction, we show

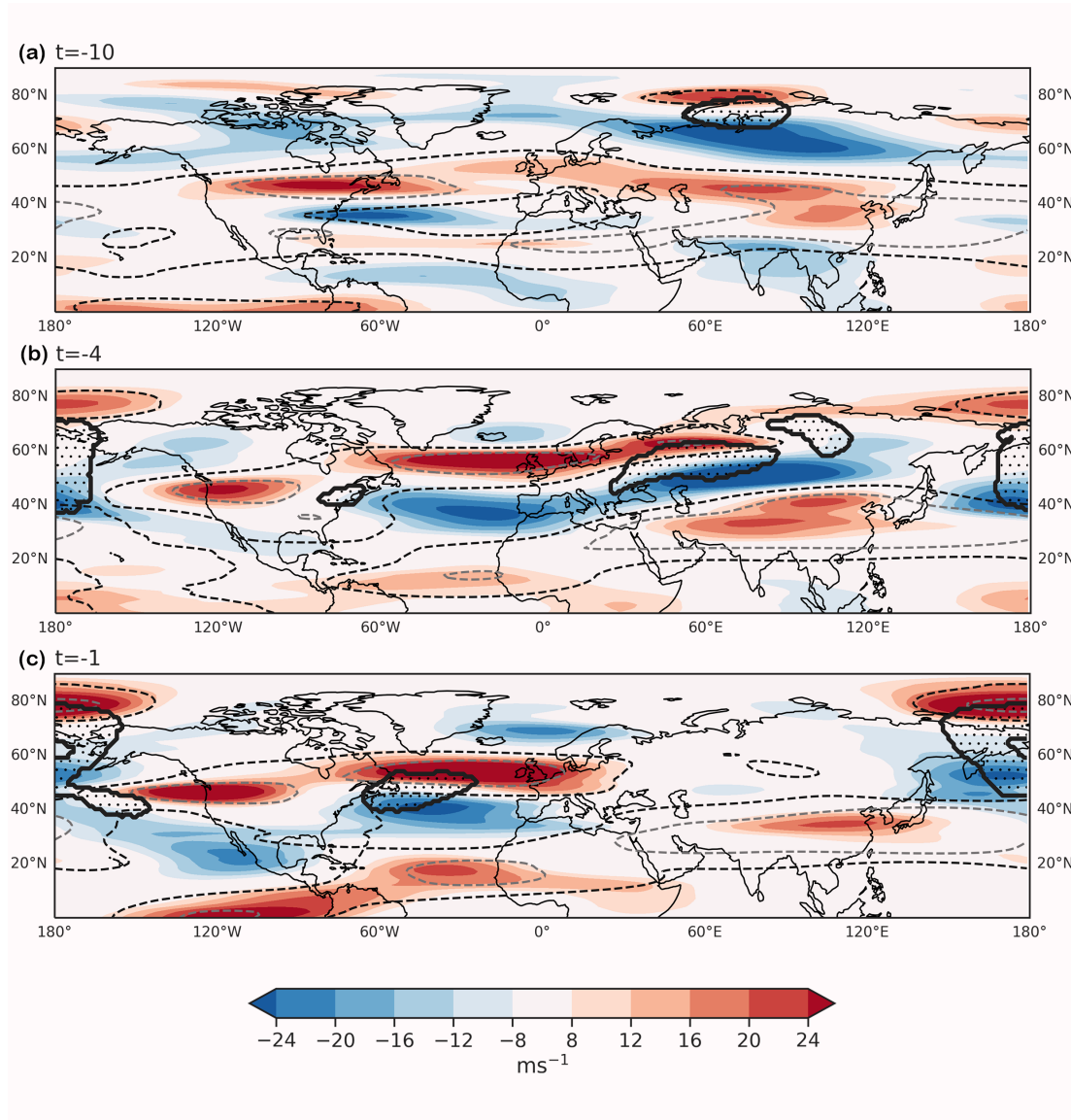


Figure 5.3: BU and blocks for the high R event in winter 2018. Colours show BU anomalies with seasonal mean at 250 hPa in  $\text{ms}^{-1}$  at various time-lag to the starting day of the event. Dashed contours show BU at 20, and 40  $\text{ms}^{-1}$ . The BU fields extend only from 0° to 90° N. Thick black contours with hatches show blocks.

OLR and  $\text{RWS}_{adv}$  anomalies in Figure 5.4 at 12-day prior to the start of the event.  $\text{RWS}_{adv}$  anomalies over the central Pacific (X in Fig. 5.4b) were co-located with the stream function (SF) anomalies that arch into North America. The band of OLR anomalies (X in Fig. 5.4a) indicate high clouds to the east of the elongated trough over the central Pacific (negative SF anomaly). The band of cold cloud top temperatures likely indicates the presence of a warm conveyor belt and the associated upper-level divergent flow providing an RWS. Concurrently, enhanced convection was present over the Maritime Continent and at the southern tip of the trough over the

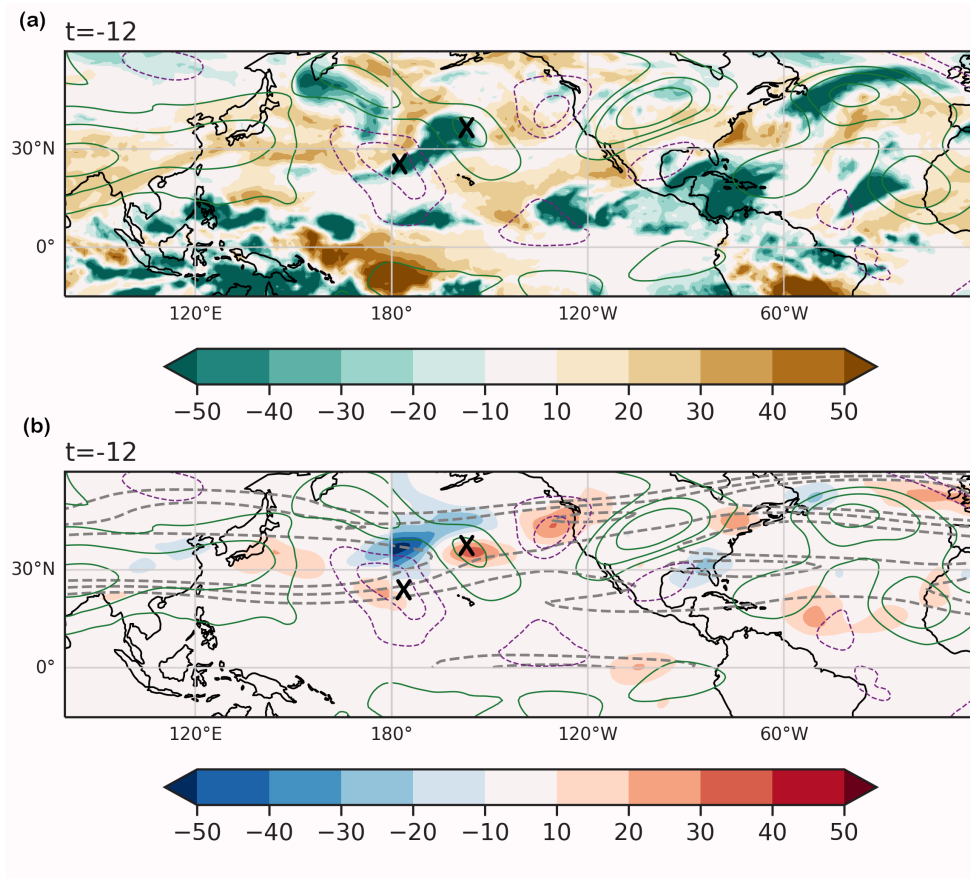


Figure 5.4: Colours show OLR anomalies in (a) and  $RWS_{adv}$  scaled by  $10^{-11}$  in (b) at  $t = -12$  days prior to the starting day of the winter 2018 high  $R$  event. Solid-green (dashed-magenta) contours in (a) and (b) show SF anomalies at 1, 2, 3  $m^2 s^{-1}$  scaled by  $10^{-6}$ . Dashed grey contours in (b) show BU at 20, 30, 40  $ms^{-1}$ . "X" in (a) show the enhanced convection and corresponding RWS in (b). All the anomalies here are with respect to the respective seasonal mean.

central Pacific. Observation records show an active MJO in Phase 3 on 15 January and moving to Phase 4 on 17 January, 14 days prior to the high  $R$  event. The trough over the central Pacific and the corresponding RWS was also persistent in the next days (not shown).

In summary, key features preceding the January 2018 event were a block establishing over the central North Atlantic just prior to the start of the event, active convection over the Maritime continent due to an ongoing MJO wave in the weeks preceding the event, which resulted in an emerging wave train from the subtropical Pacific.



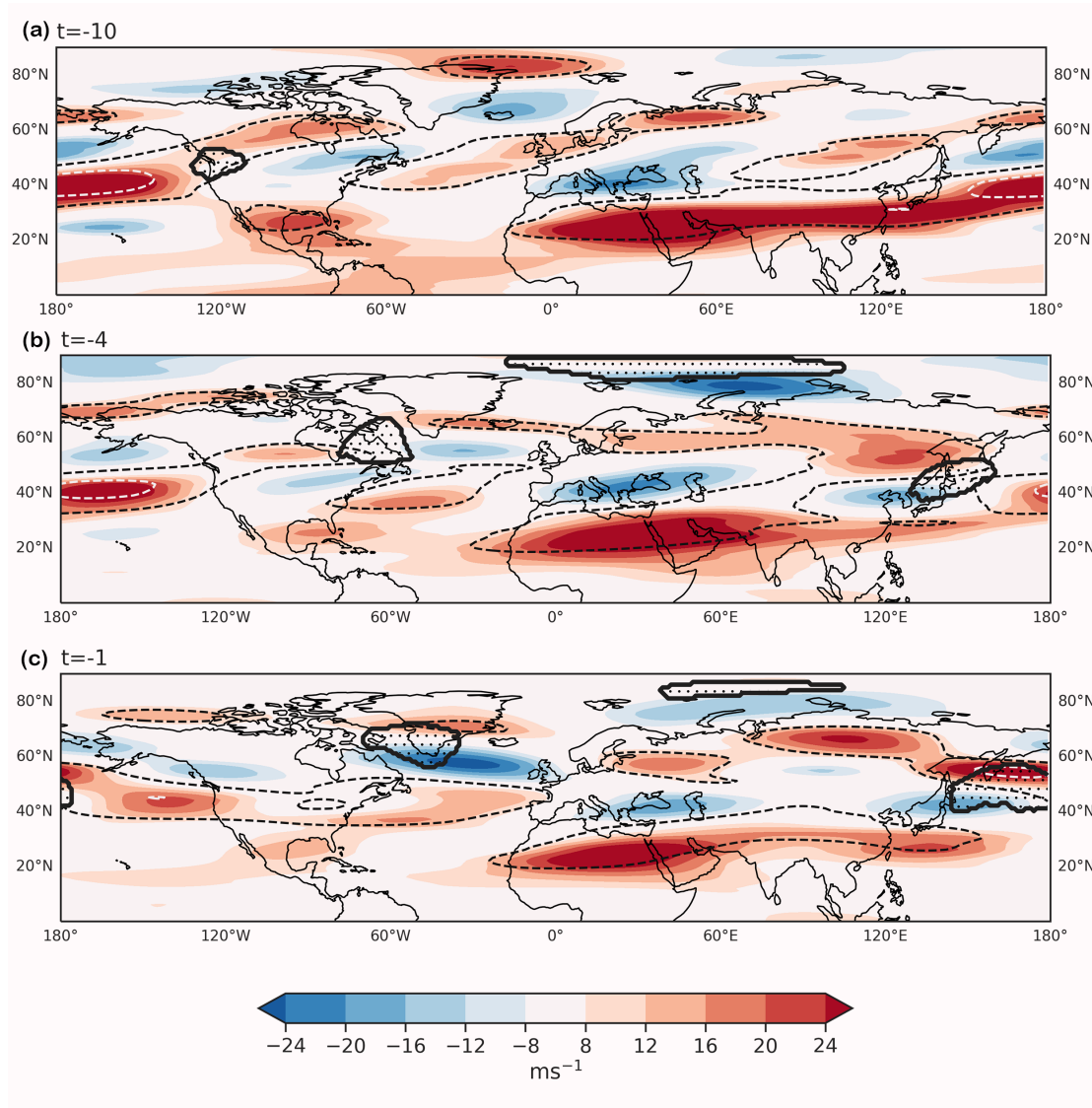


Figure 5.5: Same as in Fig. 5.3 but for the high  $R$  event in June 2003.

### 5.3.2 Example high $R$ event: June 2003

The JJA event started on 6 June 2003 and lasted nine days. It coincided with the first part of the summer 2003 heat waves over Europe. The recurrence pattern was composed of several transient wave trains, some forming upstream over the Pacific (Fig. 5.2b).

Downstream of positive BU anomalies over the Pacific a block formed over the west coast of North America on  $t=-10$  days (Fig. 5.5a), similar to the DJF event (Fig. 5.3a). This block moved downstream (see  $t=-4$  day Fig. 5.5b). Subsequently, the BU weakened over the North Atlantic. At  $t=-1$  day, the block was situated over South Greenland, and strong BU anomalies were present north and south of it. An MJO Phase 7 event was observed ten days before the

JJA event (not shown). However, we did not see an indication of a Rossby wave source from the tropics or subtropics in the SF anomalies nor any  $RWS_{adv}$  in the central Pacific. In summary, key features preceding the June 2003 event were a block forming downstream of positive BU anomalies in the eastern Pacific which was later moved to the North Atlantic.

### 5.3.3 North Atlantic DJF

#### 5.3.3.1 Composite Analysis

The theoretical considerations outlined in the introduction and the two case studies discussed above point to atmospheric blocking and tropical convection as potential drivers of high  $R$  events with the background flow acting as a modulator. To study these potential drivers in more detail and to identify actors for the CNs, composites of the atmospheric flow prior to high  $R$  events are discussed next. The composite maps focus on the period prior to and during the first days of high  $R$  events and present maps at different time-lags to the starting day of the high  $R$  event ( $t=0$ ).

First the flow over the Atlantic prior the high  $R$  events is analysed to illuminate the role of blocking and the changes in BU for high  $R$  events (Fig. 5.6). Ten days before the high  $R$  events, blocking frequencies are lower than usual south of Greenland (Fig. 5.6b). Upstream in the extra-tropical Pacific, above-average blocking frequencies are co-located with negative BU anomalies and positive BU anomalies in the subtropical Pacific.

Six days before the events, blocking frequencies are still low south of Greenland (Fig. 5.6e). The upper-level trough moves downstream over the UK, and subtropical-high forms downstream of America. The BU slows downstream of the east coast of North America, as evident by the shrinking of the  $40 \text{ ms}^{-1}$  BU contour, which is subsequently not observed at  $t=-4$  (Figs. 5.6d, 5.6g). The negative BU anomalies over the subtropical Atlantic, North America, and positive anomalies to the North indicate a northward shift of the BU at  $t=-6$  and  $t=-4$  day.

At a 2-day lag, we observe anomalously high blocking frequencies over the east coast of North America co-located with positive SF anomalies (Figs. 5.6k, 5.6l). Upstream and downstream of it, we observe enhanced BU anomalies. It is reminiscent of the situation during the 2018 January case study (Fig. 5.6). The trough over the UK re-strengthens, and a downstream ridge forms over Siberia. The ridge over America has moved eastward. Overall, SF composites depict a transient flow leading up to the starting day.

At  $t=0$  or the starting day of the events, strong negative SF anomalies are present over Europe and positive anomalies upstream over the Atlantic (Fig. 5.7c). This is a key feature because it shows the preferred phase of the the high  $R$  events over the Atlantic. The blocking frequencies are positive south of Greenland (Fig. 5.7b). Simultaneously, BU is weak over the Atlantic

and the North American east coast (Fig. 5.7b). A wave pattern is present at  $t=0$  in the SF anomalies with the wave extending from the Atlantic into the Pacific sector (Fig. 5.7c). Higher blocking frequencies persist south of Greenland after the onset, and anomalously low BU anomalies are present downstream of Greenland over north-western Europe. The trough over Europe strengthens further, and the ridge over Siberia is also persistent.

In summary, the large-scale flow changes from low blocking to high blocking over the Atlantic in the build-up to the high  $R$  events and remains high after the onset (Fig. 5.6). This points to a key role of blocking in forming high  $R$  events. At the same time, the BU over the Atlantic weakens and shifts northward. A wave train extending from the central Atlantic into Asia forms a few days prior to the high  $R$  onset (Figs. 5.6l, 5.7c), also indicating the preferred phasing of the transient eddies. Subsequently, to evaluate the causality of the observations made in the composites in a causal network (CN) framework, we create one dimensional time series by averaging BU over potential causal areas of interest (black boxes in Fig. 5.6). We average BU over the following regions: western and central Atlantic, BU-NAt ( $35^\circ$  N to  $50^\circ$  N,  $55^\circ$  W to  $15^\circ$  W), and over Pacific, BU-Pac ( $30^\circ$  N to  $40^\circ$  N and  $180^\circ$  E to  $140^\circ$  W). All the variables used in the CN model are summarized in Table 5.1.

Next, we investigate sources of Rossby waves from the tropics and subtropics. As summarized in the introduction, several studies have shown that a wave signal initiated by tropical convection in the Pacific and modulated by extratropical weather systems can propagate into the Atlantic. Hence, we next present composites maps of OLR and  $RWS_{adv}$  fields.

Negative OLR anomalies, i.e., areas of intense tropical convection, are present consistently over and to the east of the Maritime continent at around two weeks prior to the starting day of the high  $R$  event ( $t=-13$  and  $t=-12$  in Fig. 5.8). The negative OLR anomalies move eastward in the subsequent days (not shown) indicating an active MJO wave. However, we do not observe low  $p$  values for the set of the events (i.e.,  $p < 0.05$ ). It could be because of the low signal to noise ratio in the set of events. Note that the low  $p$ -values in the composites are not critical for the CNs as it is based on CI tests. At 12-day lag, a ridge-tough-ridge pattern is evident over the Pacific (SF contours in Fig. 5.8) extending into the North American continent. Active convection is present over the central Pacific, which could play a role to strengthen the upper-level trough west of it. Positive  $RWS_{adv}$  anomalies in the central Pacific are present in the central Pacific.

Studies suggest that convection over the Maritime continent can help to generate convection downstream over the central Pacific (e.g., Ghil and Mo, 1991; Johnson and Feldstein, 2010; Fromang and Rivière, 2020) and the latter are shown to have teleconnections with the North Atlantic weather regimes in the presence of a strong jet during winter (e.g., Cassou, 2008; Moore et al., 2010; Lukens et al., 2017). Our initial tests with CNs (not shown) showed that the link from OLR anomalies east of the Maritime continent to the Atlantic is indirect and modulated via the Pacific BU and  $RWS_{adv}$  term over the Pacific. Therefore, for the CN shown later, only the actor over the central Pacific is used by creating a one-dimensional time series of  $RWS_{adv}$  over the

Table 5.1: Summary of the one dimensional time series used in the CN for DJF.

Variable	Description	Grid box
R-NAt	R-metric over the North Atlantic	50°W–10°E
BU-NAt	BU over western and central Atlantic	35°–50°N, 55°W–15°W
Blocks-NAt	Fraction of area blocked over NAT	40°N–60°N, 50°W–5°W
BU-Pac	BU over Pacific	30°N–40°N, 170°E–160°W
RWS	RWS <sub>adv</sub> over Pacific	20°N–40°N, 180°W–140°W

Pacific 20°N–40°N, 180°W–140°W, later referred as only RWS in the CN model.

### 5.3.3.2 Causal Network Analysis

Table 5.1 summarizes the time series for the actors used in the CN analysis for DJF, and Fig. 5.9 shows the corresponding grid points over which the one-dimensional variables were created. In a causal graph model, directed arrows, called edges, are shown between two variables that are significantly associated with each other. As an example,  $X \xrightarrow{t} Y$  shows changes in  $X$  at a time lag  $t$  is a statistically significant causal driver for changes in  $Y$ . Dashed edges show instantaneous association and do not show a causal direction. The numbers accompanying the name of an variable state the strength of the auto-correlated link. When there are causal links at multiple lags between two variables, the lags displayed over the edges are sorted in decreasing order of the correlation strength with the colour of the edge representing the strongest link. In such a case, if the correlation between the two lags is of opposite sign then it is displayed by the asterisk sign above the lag, e.g.,  $X \xrightarrow{9, 3^*} Y$  implies that the link from  $X$  to  $Y$  at 9-day lag is stronger and oppositely correlated then the one at 3-day lag and the colour of the link  $X \rightarrow Y$  will show the cross-correlation of the 9-day lagged link.

We begin by discussing the CN for DJF (Fig. 5.10). A key result from the CN is that Blocks-NAt primarily drives R-NAt. A positively correlated link Blocks-NAt  $\xrightarrow{6}$  R-NAt is seen at a 6-day lag. This link is consistent with Fig 5.6, where we see an increase in blocking frequency over the Atlantic in the build-up to the high  $R$  events ( $t=0$  day) and positive blocking frequency anomalies at the onset ( $t=0$ ) and later (Fig. 5.7). R-NAt has feedback on Blocks-NAt at two different time lags: positively correlated at 3-day lag with a strength of 0.101 and negatively correlated at 9-day lag with a strength of -0.0807. These two feedback links are robust in the sensitivity tests (App. C.3).

There are no direct links from BU-NAt to R-NAt (Fig. 5.10). BU-NAt may indirectly affect R-NAt by modulating Blocks-NAt, shown by BU-NAt  $\xrightarrow{3, 6^*}$  Blocks-NAt. R-NAt has a feedback on BU-NAt at two different time lags, R-NAt  $\xrightarrow{3, 9^*}$  BU-NAt. The two feedback links are oppositely correlated with a correlation of 0.127 at 9-day lag and -0.115 at 3-day lag. The oppositely corre-

lated links between R-NAt and BU-NAt can be understood when considering the instantaneous association between BU-NAt and Blocks-NAt. At a shorter time lag of 3 days, R-NAt decreases BU-NAt and increases Blocks-NAt, whereas, at a lag of 9 days, R-NAt increases BU-NAt and decreases Blocks-NAt. Overall, the drivers of RRWPs over the Atlantic agree with our theoretical understanding that an increase in the low wavenumber flow at upper levels will be positively correlated with increased vertical shear and is associated with increased baroclinicity as per the thermal wind relation. High baroclinic conditions lead to baroclinic eddies that grow using the potential energy of the system (e.g., Pierrehumbert and Swanson, 1995). However, for large values in  $R$ , these baroclinic eddies need to recur in the same phase. From a dynamic perspective, one could argue that BU and Blocks are closely linked. However, the CNs show that BU-NAt does not modulate the links from Blocks-NAt to R-NAt. There is also a link from BU-Pac to BU-NAt and not to Blocks-NAt. Based on these unique links, we choose to keep both the actors in the CN models.

There is no direct causal link between RWS in the Pacific and R-NAt. An indirect pathway exists where  $\text{RWS} \xrightarrow{3,6^*,9^*} \text{BU-Pac}$  and  $\text{BU-Pac} \xrightarrow{6} \text{BU-NAt}$ . Our findings are in agreement with previous studies that suggest that convection-related anomalies in the Pacific can be a source for jet variability in the North Atlantic but that the response over the Atlantic is modulated by the regional baroclinic and barotropic instabilities (e.g., Frederiksen, 1982, 1983; Wu, 1993; Franzke and Feldstein, 2005; Stan et al., 2017).

### 5.3.4 North Atlantic JJA

The composite maps for high  $R$  events in summer (JJA) follow the same approach as for DJF.

#### 5.3.4.1 Composite analysis

Like winter events, blocking frequencies are lower south of Greenland at a 10-day lag to the high  $R$  events (Fig. 5.11). The blocking anomalies coincide with anomalously high BU over the North Atlantic, and the SF composites feature negative anomalies, indicating an upper-level trough over southern Greenland. Downstream, over eastern Siberia, a ridge is observed. Upstream of the Atlantic, over Quebec and Newfoundland, an upper-level ridge is observed with above-average blocking frequencies. The BU indicates weakening over subtropical Atlantic and America, and the positive anomalies North of it suggest a northward shift in BU.

At a lag of six days, blocking increases over the extratropical Pacific with corresponding changes in BU north and south of the blocking (Figs. 5.11d, 5.11e). The  $20 \text{ ms}^{-1}$  BU contour is connected over the Pacific up to the Atlantic and extends upstream until the Mediterranean. An upper-level trough-ridge couplet is seen over Iceland and the UK. The ridge over Siberia persists as well. A hemispheric-wide wave number pattern is not clear at this stage. At 4-day lag, the ridge persists over north-western Europe, a ridge-trough-ridge pattern emerges over the Atlantic, and a ridge

is observed over the east coast of the US (Fig. 5.11i). Positive blocking frequencies persist over the Pacific along with the concurrent anomalies in the BU. Increased blocking is also seen over southern Greenland and Canadian archipelago parts.

At 2-day lag, the ridge-trough-ridge pattern persists over the Atlantic, with the ridge over Europe (Fig. 5.11l). The ridge over the eastern US persists as well as the trough over the Pacific. Blocking anomalies are persistent over south Greenland, along with the decrease in BU (Figs. 5.11k, 5.11j). Positive blocking frequencies are seen over the UK and north-western Europe. The  $20 \text{ ms}^{-1}$  BU contour, which previously stretched from the Mediterranean to the Pacific and into the Atlantic, splits into three.

At day zero, the ridge over Europe extends over central Europe, and the ridge south of Greenland strengthens with the corresponding anomalies in the blocking frequencies (Fig. 5.12 b, c). The blocking anomalies have decreased over the Pacific as well (c.f.  $t=-4$  and  $t=-2$  in Fig. 5.11). There is an overall decrease in BU over the Atlantic and North America. The BU stays weaker over the Atlantic two days later, and the ridge persists south of Greenland. The ridge over central Europe also persists, and the ridge over eastern Europe moves slightly downstream.

As for the DJF events, we looked for tropical and subtropical RWS sources. We find active convection in the tropics around the Maritime continent prior to the JJA high  $R$  events but the corresponding SF anomalies do not arch into the extra-tropics and instead propagate parallel to the equator (not shown). Furthermore, over the central Pacific, we did not observe active convection and correspondingly, no positive  $\text{RWS}_{adv}$  anomalies were present over the Pacific unlike for DJF (Fig. 5.8). Therefore, we do not find indications of teleconnections between the tropics and the mid-latitudes for summer. Our findings are in line with previous studies that also report an absence of the tropical teleconnections with the Atlantic for summer (Stan et al., 2017). However, tropical-extratropical connection might still be observed for individual events.

To summarize, the important changes before the JJA events are an increase in blocking over south Greenland, and first strengthening and then weakening of the subtropical BU over the Pacific corresponding to the changes in blocks over the Pacific. Hence, based on Figures 5.11 and 5.12, we create two one-dimensional time series of BU for the CN for summer: BU over the North Atlantic, BU-NAt  $40^\circ \text{ N}$  to  $55^\circ \text{ N}$ ,  $65^\circ \text{ W}$  to  $25^\circ \text{ W}$ ; BU over the eastern Pacific, BU-EPac  $30^\circ \text{ N}$  to  $40^\circ \text{ N}$ ,  $170^\circ \text{ W}$  to  $130^\circ \text{ W}$ . The area used for BU-NAt is slightly north of the one used for DJF (Table 5.1) because of the changes seen in the composites (cf. Fig. 5.11 and Fig. 5.6). Similarly, we create a time series of fraction of area covered by blocks over the North Atlantic, i.e., over  $50^\circ \text{ N}$  to  $65^\circ \text{ N}$  and  $50^\circ \text{ W}$  to  $30^\circ \text{ W}$ , which is also slightly northward to the area used for winter (Table 5.1). Figure 5.13 shows the area over which time series are averaged and table 5.2 summarizes the variables used in the CN.

Table 5.2: Summary of the one dimensional time series used in the CN for JJA.

Variable	Description	Grid box
R-NAt	R-metric over North Atlantic	50°W–10°E
Blocks-NAt	Fraction of area blocked over North Atlantic	50°N–65°N, 50°W–30°W
BU-NAt	BU over North Atlantic	40°–55°N, 65°W–25°W
BU-EPac	BU over eastern Pacific	30°N–40°N, 170°W–130°W

#### 5.3.4.2 Causal Network Analysis

In summer, we find three causal drivers of R-NAt: BU-NAt, Blocks-NAt and BU-EPac (Fig. 5.14). The link from the BU-NAt  $\xrightarrow{9}$  R-NAt is positive and acts on a time scale of 9 days. An increase in BU is also captured in the composites (e.g.,  $t=10$  day in Fig. 5.11a). A stronger upper-level flow over the North Atlantic also decreases blocking (the link BU-NAt  $\xrightarrow{3}$  Blocks-NAt and the instantaneous link between the two). We also find a positive causal link Blocks-NAt  $\xrightarrow{3}$  R-NAt. A feedback R-NAt  $\xrightarrow{3}$  Blocks-NAt is observed that could indicate that the transient synoptic waves that form the RRWPs contribute to blocking strength and persistence. This is in line with Shutts (1983); Hoskins and Sardeshmukh (1987). Blocks-NAt  $\xrightarrow{3}$  R-NAt acts on a time-scale of 3 days. The links between BU-NAt, Blocks-NAt and R-NAt capture the interactions between the background flow, blocks, and RRWPs over the Atlantic as outlined in the introduction. Note, that the causal connection to R-NAt is not mediated solely through either BU-NAt or Blocks-NAt, this implies that both processes modulate R-NAt; even though the dynamics of BU-NAt and Blocks-NAt are closely linked.

Upstream in the Pacific, we find a positively correlated causal link from BU-EPac  $\xrightarrow{3}$  R-NAt. This link is robust in the sensitivity tests. In the BU composites (Fig. 5.11), a significant increase in BU over the eastern Pacific preceded high  $R$  events. One of the underlying processes to explain this link could be that an increase in BU-EPac may help to exceed the capacity of the zonal wave activity flux, which then results in the formation of the blocks downstream over North America (Nakamura and Huang, 2018). This is also seen in the blocking composites (e.g.,  $t=-4$  in Fig. 5.11). The resulting blocks may play a role in modulating RRWPs downstream (Altenhoff et al., 2008; Röthlisberger et al., 2019). We also observe a positively correlated causal link BU-NAt  $\xrightarrow{6}$  BU-EPac. This link is robust in the sensitivity tests. The mechanisms through which the BU-NAt acts on the BU-EPac are not immediately apparent and therefore, this link can be treated as causal discovery. It could very-well be that a hidden process, not included in the CN, acts to mediate the link between BU-NAt and BU-EPac. In summary, the primary drivers of R-NAt are the process over the Atlantic, BU-NAt and Blocks-NAt, and BU-EPac. R-NAt has a feedback on Blocks-NAt.



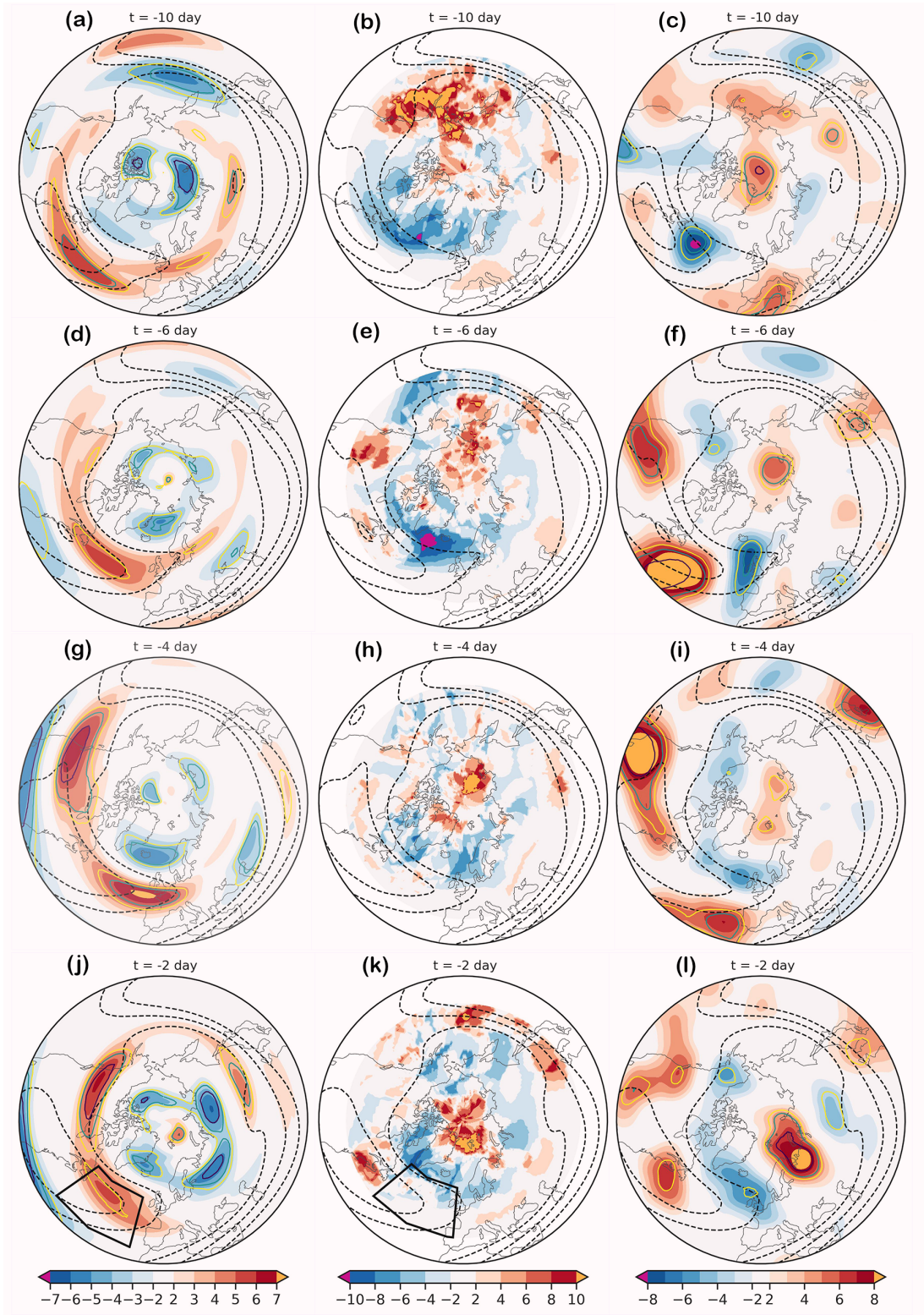


Figure 5.6: Composite mean anomalies for meteorological fields extending from  $30^\circ \text{N}$  to  $90^\circ \text{N}$ : left column BU, middle column blocking frequency, right column SF at different time lags to the starting day of DJF high R events in the North Atlantic. Black dashed contours show mean BU contours at 20, 30, and  $40 \text{ ms}^{-1}$  at the given time lag. Yellow, green, and blue contours show  $p$  values at 0.1, 0.05, and 0.01, respectively except for blocks. Black boxes in (j) and (k) show the area used to create 1-dimensional time series for the CNs.



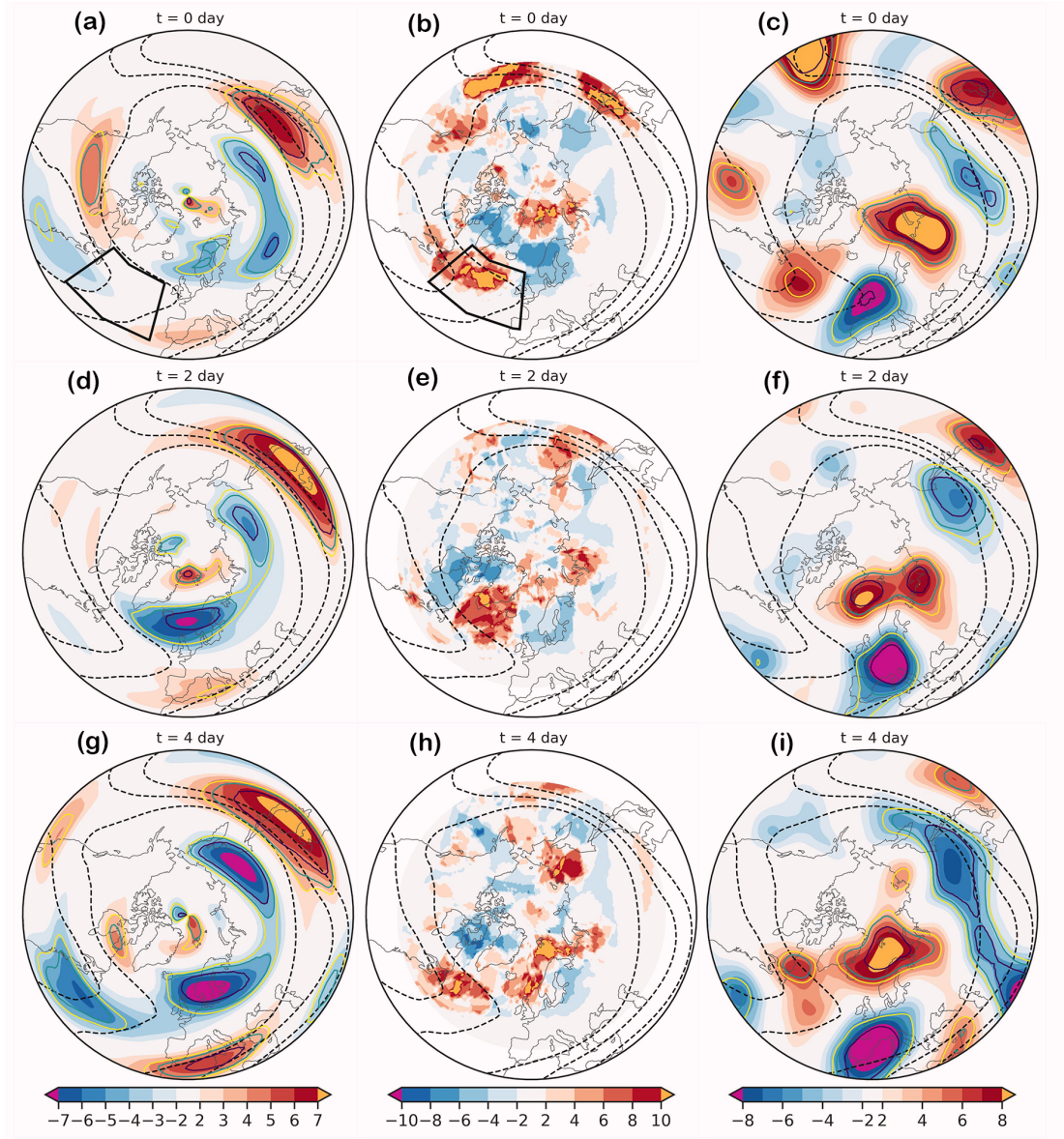


Figure 5.7: As in Figure 5.6, but for the onset of the events and after. Black boxes in (a) and (b) show the area used to create 1-dimensional time series for the CNs.

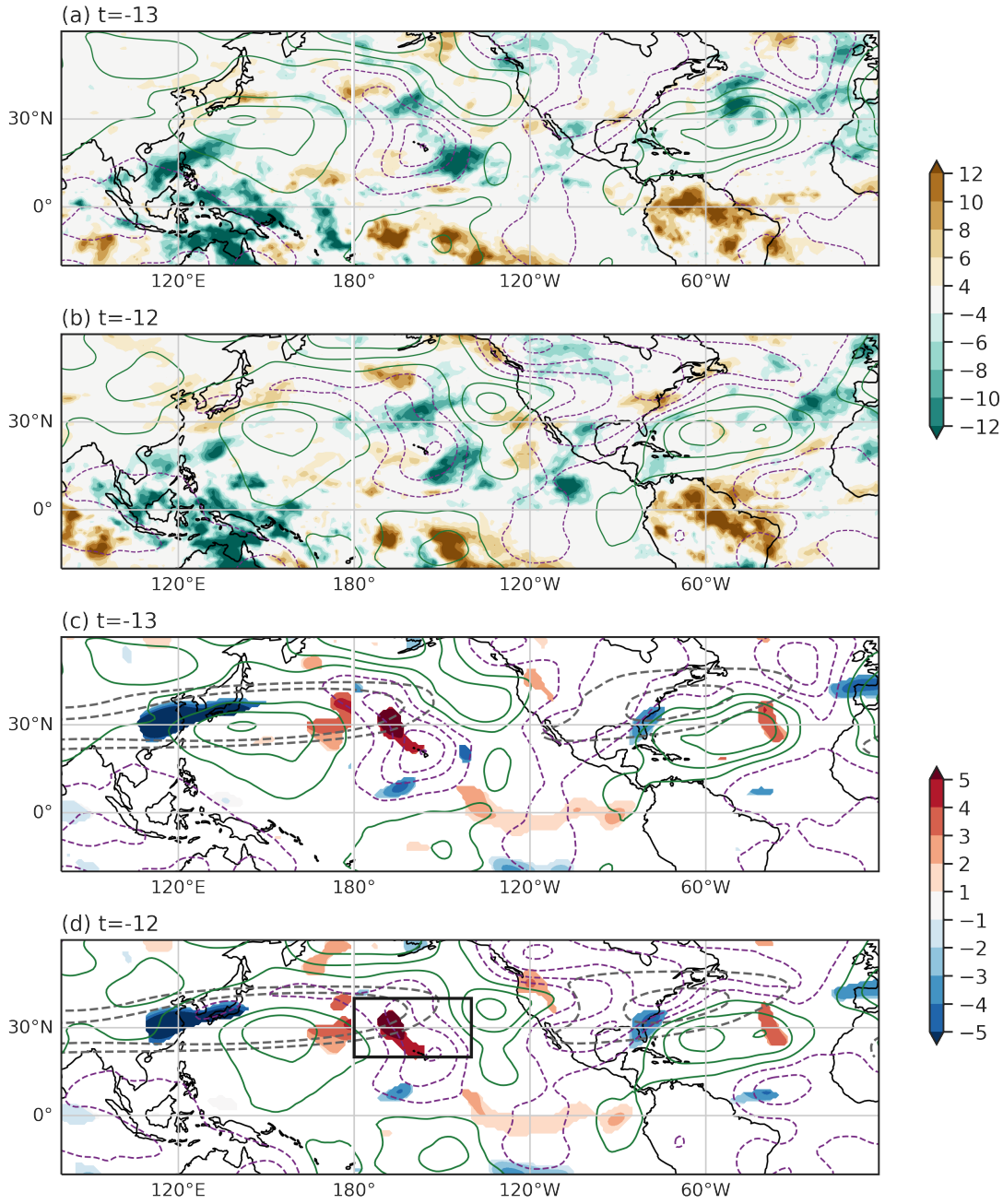


Figure 5.8: Same as in figure 5.6 but for absolute OLR anomalies ( $Wm^{-2}$ ) in (a) and (b) and  $RWS_{adv}$  anomalies ( $s^{-1}$ ) at 250 hPa (scaled by  $10^6$ ) in (c) and (d). In (c) and (d) anomalies are shown only at grid points having  $p < 0.1$ . Solid green (dashed magenta) contours in all subplots show SF anomalies at 250 hPa scaled by  $10^{-6} m^2 s^{-1}$ . BU contours at 30 and 40  $ms^{-1}$  are shown in grey dashed lines in (c) and (d). Black box in (d) show the area used to create 1-dimensional time series for the CNs.

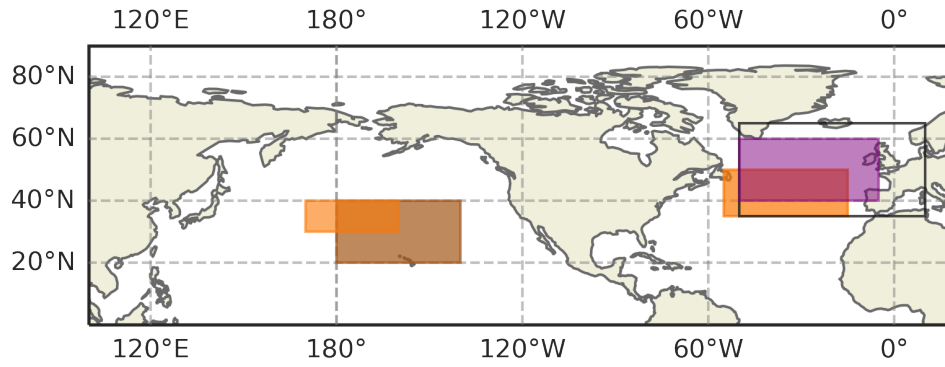


Figure 5.9: Grid boxes over which the time series were averaged to create one dimension time series (cf. Table 5.1) for the CN model for DJF. Black box over the North Atlantic shows area over which metric  $R$  is averaged. Purple box shows the area used to create the blocking time series. Orange boxes show area used to create the two BU time series, and brown box shows the same for  $RWS_{adv}$  time series.

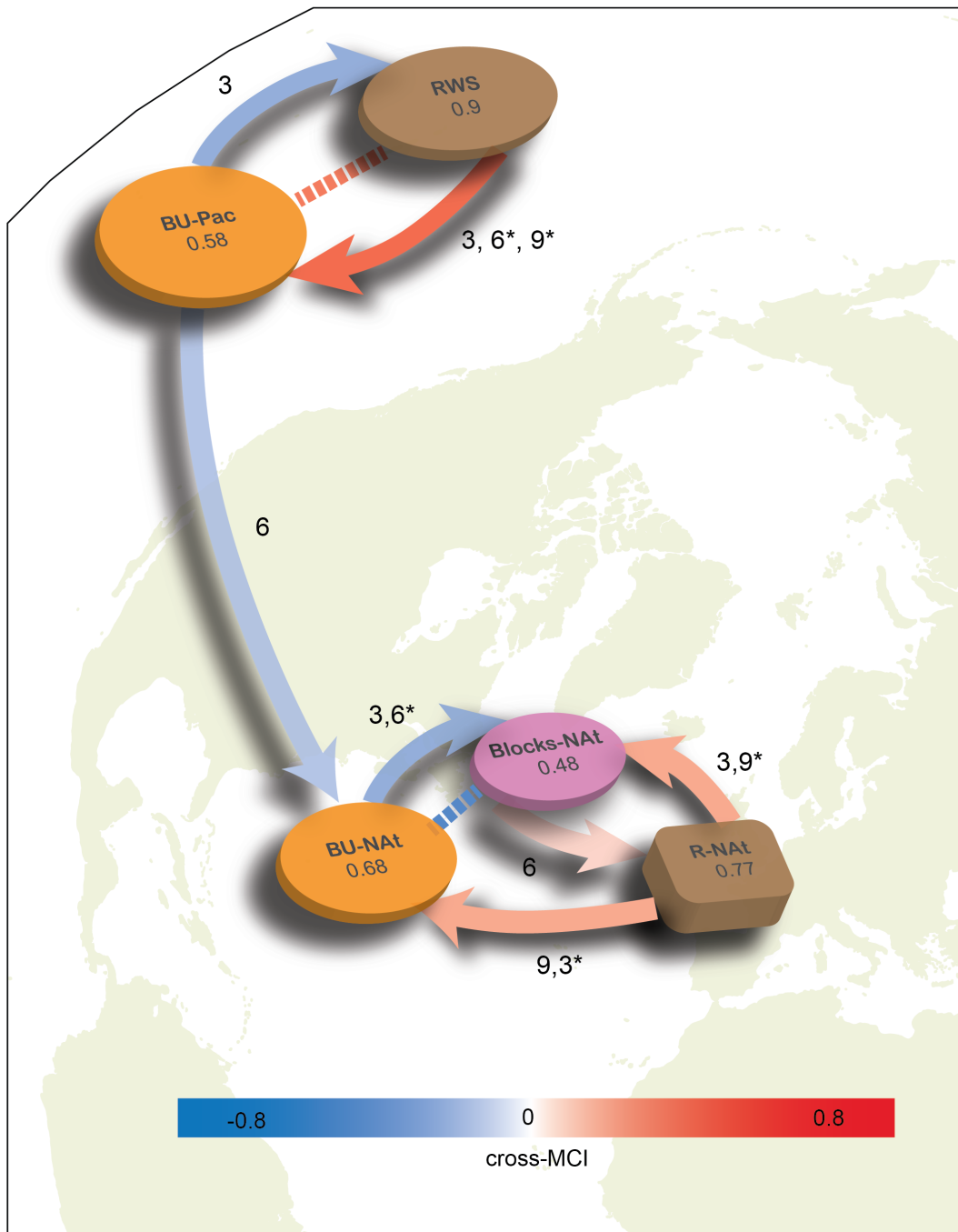


Figure 5.10: Causal Network (CN) shows significant drivers of  $R$  over the North Atlantic for DJF at  $p < 0.05$  and a maximum time lag of 15 days. The number over the edges indicate the time lag in days of the causal link and the colour of the edges show the strength of the link. Instantaneous links are shown by dashed edges. Numbers accompanying the actors show the auto-correlation. See appendix C.1 for the full model output.



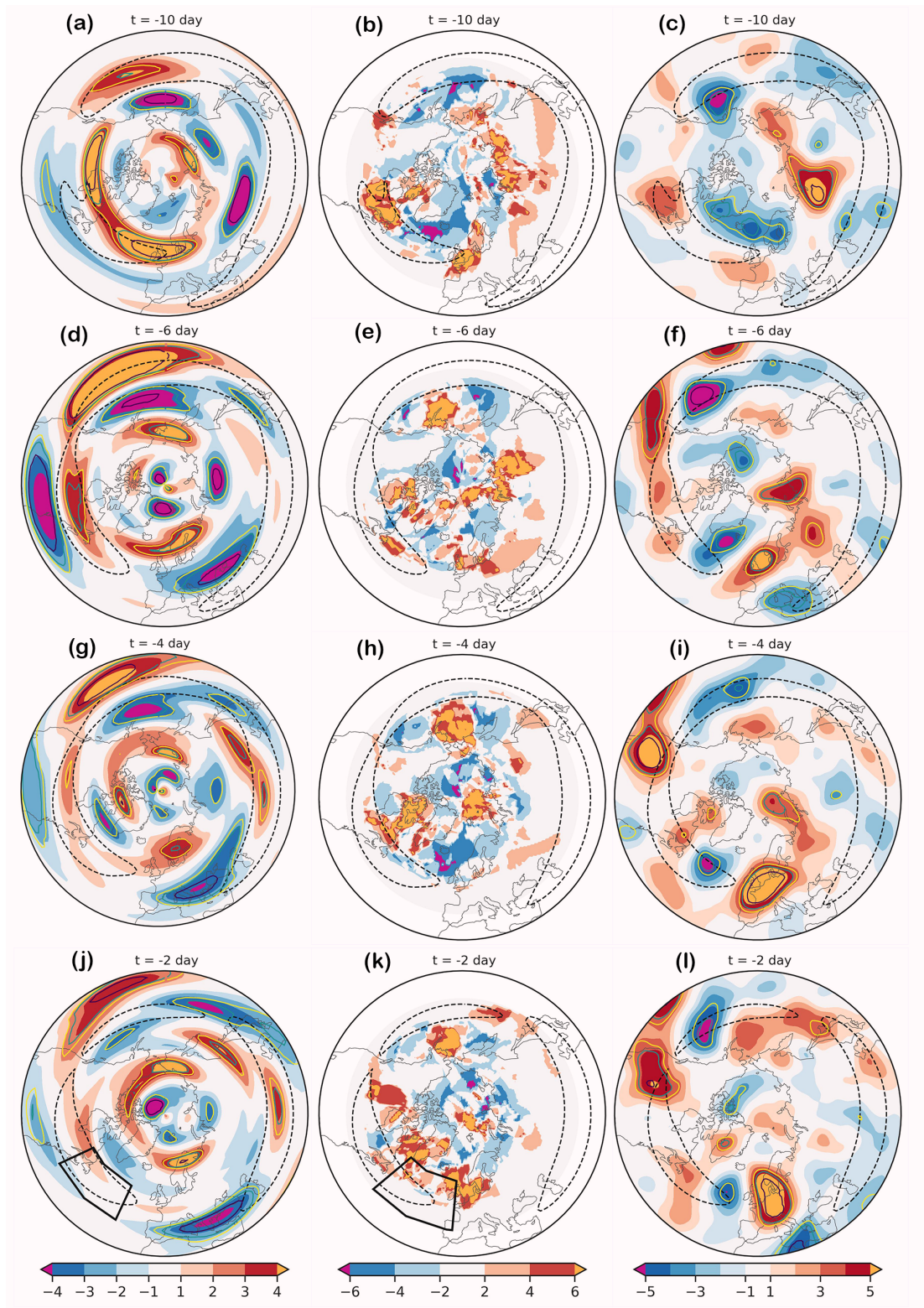


Figure 5.11: As in Figure 5.6 except for high  $R$  events in JJA.

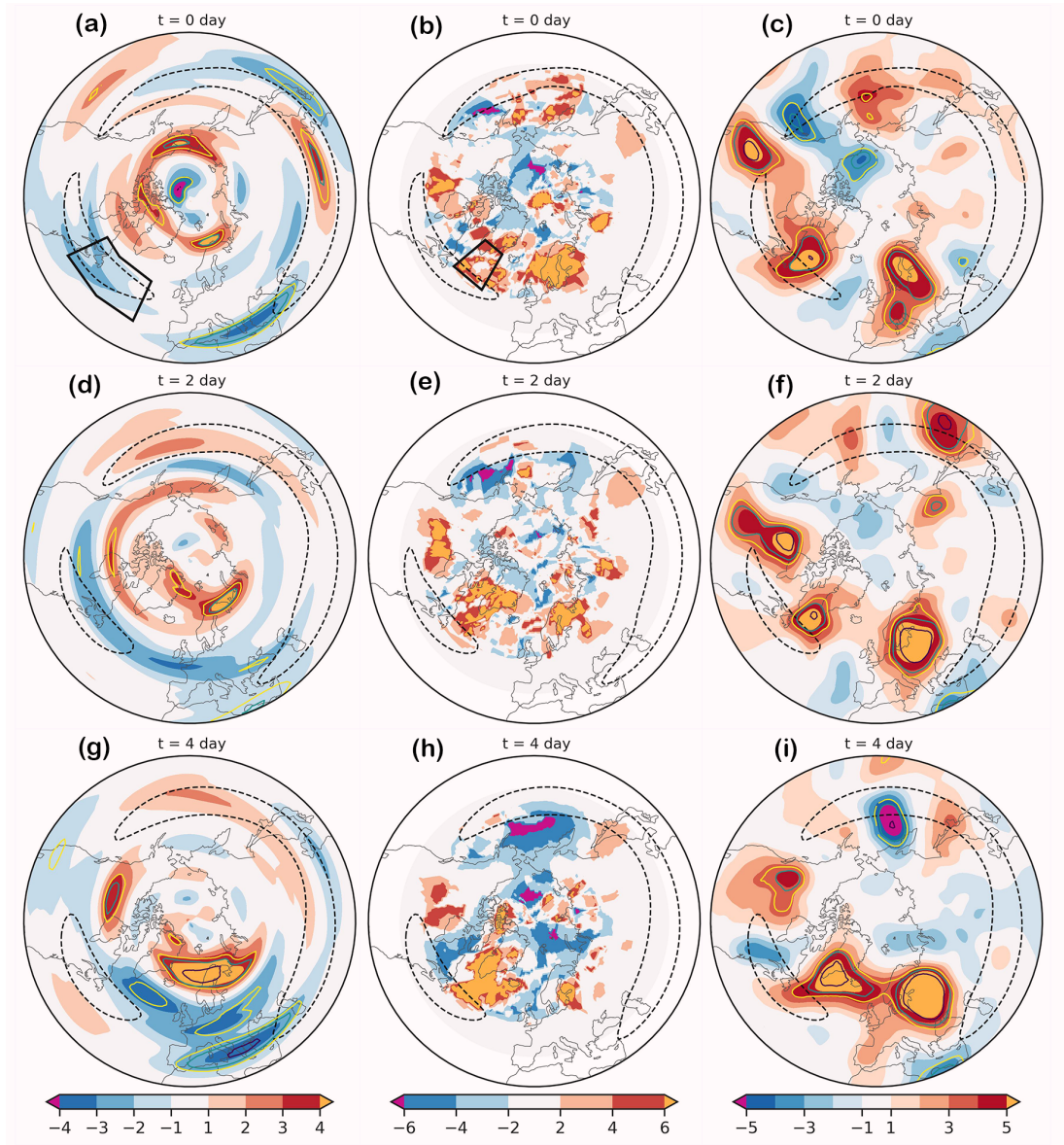


Figure 5.12: As in Fig. 5.7 except for high  $R$  events in JJA.

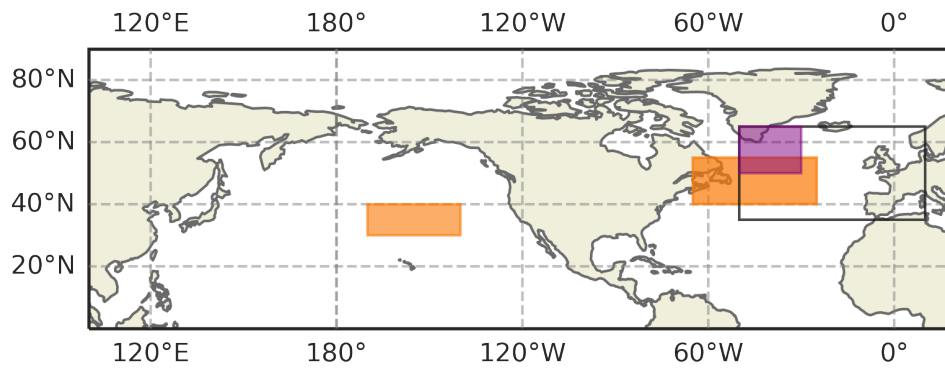


Figure 5.13: Grid boxes over which the time series were averaged to create one dimension time series (cf. Table 5.2) for the CN model for JJA. Colours used are the same as in same as in Fig. 5.9 except that no RWS time series is used for the JJA model.

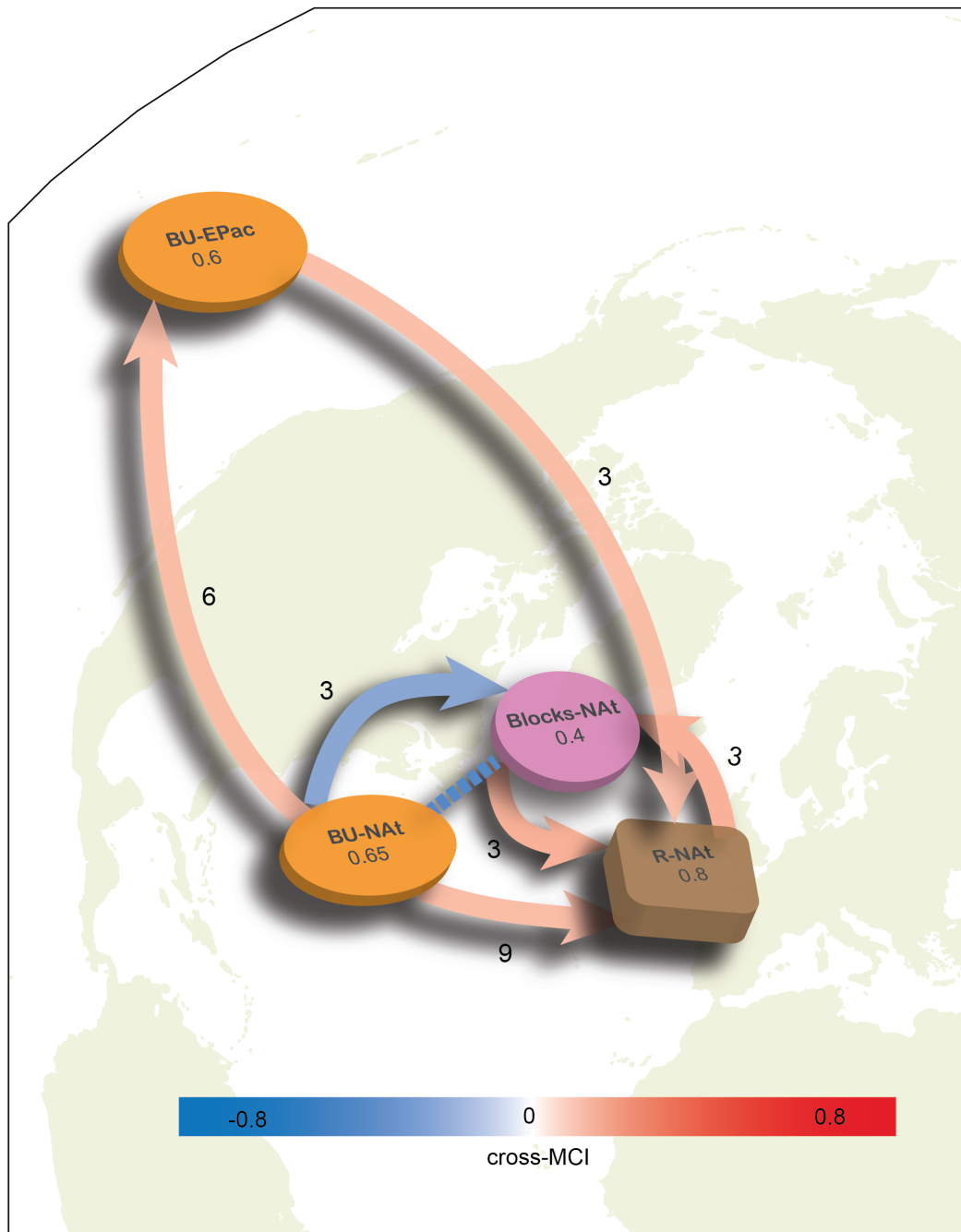


Figure 5.14: CN same as in Fig. 5.10 but shows significant drivers of  $R$  over North Atlantic for JJA. The  $p$  value and  $\tau_{max}$  used are the same as in Fig. 5.10. See appendix C.2 for the full model output.



## 5.4 Discussion

The time-lagged composites show the dominant anomaly patterns for the set of top-30 North Atlantic RRWP events for summer and winter. For winter events, a hemisphere-wide wave pattern emerges at  $t=0$ , suggesting concurrent high  $R$  events in the Atlantic and the Pacific (Fig. 5.6). The hemisphere-wide wave pattern is not evident for the summer high  $R$  events (Fig. 5.11). Note that the CNs use the full time-series and hence, bring forward the causal drivers significant in the climatology. CNs also do not have a subjectively-chosen starting day ( $t=0$ ) as for the composites, where the starting day is defined by the peak over threshold method. However, interpreting the links found by the CNs with the help of composites of the top high  $R$  events helped to explain the links observed in the CNs.

The CNs show a statistically significant association between the background flow (BU), blocks, and RRWPs over the North Atlantic for winter and summer (Figs. 5.10, 5.14). In summer, BU acts directly on  $R$  whereas in winter, BU acts on blocks over the Atlantic, and the latter act on RRWPs. We find positive BU anomalies for winter composites at a 10-day lag over  $40^\circ$  N in the Atlantic. For the summer composites, the positive anomalies are in the extratropical North Atlantic to the south of Greenland. The increase in BU prior to the events is correlated with an increase in EGR anomalies (not shown) and suggests that RRWPs may form because of the high baroclinicity in the Atlantic and may not necessarily need a tropical forcing. Furthermore, Novak et al. (2015) suggests that enhanced storm-track activity is responsible for downstream latitudinal shifts in the jet. However, why are the Rossby waves recurring in the same phase?

Our results suggest that blocks play a vital role in modulating the phase of the Rossby waves, helping them to recur in the same phase. Blocks may act like a metronome to modulate the phase the RRWPs (Altenhoff et al., 2008; Röthlisberger et al., 2019). The association between blocks over Atlantic and  $R$  revealed by the CNs might support the role of blocks in modulating the phase of RRWPs. Furthermore, the CNs show that an increase in blocking over the Atlantic is closely associated with a decrease in BU. RRWPs also have feedback on blocks and BU in both seasons. There is direct feedback from RRWPs on BU in winter, but an indirect link in summer modulated by blocking. The feedback on the BU can be through wave amplification, and Rossby wave breaking, where the momentum transfer from the wave breaking changes the background flow (e.g., Moore et al., 2010).

Hamill and Kiladis (2014) show that European blocking frequency shifts from being anomalously low to being anomalously high as the MJO convection shifts across the Maritime continent, consistent with the results of Cassou (2008). The CN for winter shows that the link between tropical convection in the Pacific basin and RRWPs over the North Atlantic in winter is indirect and captured by the advection-term of the Rossby wave source in the Pacific (Fig. 5.10). The "indirect" link implies that the tropical link is mediated by changes in the background flow over the central Pacific. Hence, it is unnecessary to include an OLR-related actor in the CN (Kretschmer

et al., 2021). We find that the BU over the Pacific influences the BU over the Atlantic, thus acting indirectly on RRWPs. Our results do not contradict the above observations and the idealized model studies showing a tropical, and mid-latitude teleconnection (see the introduction, e.g., Sardeshmukh and Hoskins, 1988; Hoskins and Ambrizzi, 1993; Matthews and Kiladis, 1999; Fromang and Rivière, 2020).

However, RRWPs do not necessarily need a forcing external to the mid-latitude flow, and recurrent but rather local perturbations in the baroclinic regions can also trigger them. CNs suggest the local changes in blocks and BU drive  $R$  over the Atlantic as the CNs identify the most substantial causal effect on  $R$  from these actors. However, the CN for winter suggests that tropical-extra tropical teleconnection exists and could be one of the sources of the variability in the background flow over the Atlantic. During summer, we did not find large RWS anomalies in the tropical Pacific. Although, we do find a direct causal link from BU over subtropical Pacific to  $R$  over the Atlantic (Fig. 5.14). The changes in BU over subtropical Pacific is possibly due to the extratropical blocking over the Pacific ( $t=-6$  day in Fig. 5.11).

The CNs used in this study are based on a linear model, which might not be able to capture some of the non-linear processes. Another limitation is that the PCMCI algorithm used here cannot detect latent confounders, that is, the hidden processes which are not included in the CNs. This is a challenging problem for the machine learning community and recent developments are trying to address it (Gerhardus and Runge, 2020; Liu et al., 2021). However, despite these limitations, the CN approach is more rigorous in providing insights into true causal relationships than the standard practices of correlation and regression analysis (e.g., Kretschmer et al., 2016; Runge et al., 2019a; Di Capua et al., 2020; Saggioro and Shepherd, 2019; Vijverberg and Coumou, 2022).

## 5.5 Conclusions

RRWPs over the Atlantic can lead to persistence and high-impact weather through the recurrent formation of troughs or ridges on sub-seasonal time-scale over Europe. This study identifies drivers of RRWP events over the North Atlantic for winter and summer based on theoretical considerations, two case studies, a composite analysis and causal networks. We present composite maps of meteorological variables prior to 30 high  $R$  events in winter and summer and use them to select actors for a theory-guided CN framework.

For RRWP events in winter, a hemispheric wave pattern emerges in SF anomalies at start day of the events but not so for summer. The composites maps for winter show a ridge-trough pattern with a ridge over the Atlantic and trough over western Europe at  $t=0$  (Fig. 5.7). For RRWP events in summer, we see a ridge-trough-ridge pattern with the two ridges over the Atlantic and central Europe at  $t=0$  (Fig. 5.12). The RRWP events for both the seasons reveal a preferred phasing of the RRWPs despite not having an explicit condition for phasing in the event selection.

The CN for summer reveals the link  $BU \rightarrow R$  as causal at a 9-day lag (Fig. 5.14), but not so for winter (Fig. 5.10). This association is seen in the composites where BU over the North Atlantic increases around 10 days before the onset of RRWP events (Fig. 5.11). However, in the winter, also we see similar changes in BU (Fig. 5.6), but the CN does not reveal that link as causal. Instead, the causal driver for winter is only blocks over the North Atlantic, where blocks are closely associated with BU over the Atlantic. Blocks also causally driver  $R$  for summer and are also closely associated with BU. We hypothesize that blocks act by modulating the phasing of the RRWPs. The RRWPs, in turn, have feedback on the blocks (Figs. 5.10, 5.14), which helps to make them more persistent.

We also observe active convection over the Pacific before the onset of the winter RRWP events. The CN reveals that this drives changes in BU over the Pacific, which drives changes in BU over the Atlantic. For summer, the CN shows a direct 3-day lagged link from the subtropical eastern Pacific  $BU \rightarrow R$  over the Atlantic and a 6-day lagged link from BU over the Atlantic  $\rightarrow$  BU over the eastern Pacific. However, the SF composites for RRWP events in summer did not show Rossby waves arching into the extratropics, unlike in the winter. We also do not have a theoretical understanding of the causal link  $R \rightarrow BU$  over Pacific (Fig. 5.14). We treat this link as a casual discovery because it was robust in our sensitivity tests and suggest that it needs to be investigated in future studies.

The CNs show that complex interconnections between different processes modulate the flow variability over the North Atlantic. Therefore, correct simulations of intermediate processes are essential for improving forecasts and removing model biases. The connections upstream from the Pacific to the Atlantic may offer a window of opportunity for improving predictability over the Atlantic for RRWP events.

## 5.6 Acknowledgments

SMA is grateful for discussions with Brian Hoskins, Ted Shepherd, and also for discussions with Elena Saggioro and Giorgia Di Capua on the application of causal networks.



## Chapter 6

# Conclusions and Outlook

### 6.1 Summary and conclusions

This thesis demonstrates the vital role of RRWPs in persistent surface weather and investigates the causal drivers of RRWPs over the North Atlantic. Previously, mainly stationary flow has been considered an important driver of persistent weather conditions. However, the first part of the thesis established the vital role of recurrent transient synoptic-scale Rossby wave packets as a non-stationary mechanism for modulating persistent surface weather. The second part of the thesis investigated the association of RRWPs with quasi-stationary anticyclones identified as blocks and the quasi-stationary anticyclones driven by quasi-resonant amplification (QRA). Furthermore, the thesis identified the causal drivers of RRWPs in the North Atlantic.

Chapter 2 examined the role of RRWPs for dry and wet spells. It revealed that RRWPs significantly affect the duration of dry and wet spells globally by significantly shortening or extending the persistent dry/wet conditions. Spatial patterns of statistically significant regression coefficients feature superimposed components, a zonally symmetric component, and a wave-like component modulated by local effects, presumably arising from the local geography, such as orography or the position relative to major moisture sources. The zonally symmetric component is apparent during the Northern Hemisphere (NH) winter and dominates the Southern Hemisphere (SH) signal in both seasons. Moreover, a lack of a wave signal in the SH extratropics and the wavenumber (WN) dependence on the season (change from WN4 in winter to WN6 in summer) suggests that the wave component is related to the stronger planetary waves in the NH that organise the transient eddies in preferred phases. Finally, the intricacies of local effects such as orography and moisture availability also dictate the persistence of dry and wet spells.

The aim of Chapter 3 was to study the role of RRWPs for persistent hot spells in the SH. Furthermore, the chapter examined the role of RRWPs in the most persistent and extreme south-eastern Australian (SEA) heatwaves. RRWPs are associated with a significant increase in the persistence of hot spells over parts of South America and Australia. Several parts of SEA, including the states of South Australia, New South Wales, Victoria, and Tasmania, show longer hot spells

coincide with high amplitude RRWPs. Case studies of two SEA heatwaves – the 2004 and 2009 heatwaves demonstrate the role of RRWPs in building recurrent ridges over SEA. Furthermore, this chapter investigated the co-occurrence of RRWPs during the most persistent and extreme SEA heatwaves. On days with RRWPs, there is an increased conditional probability of SEA heatwaves compared to climatology. However, not all days associated with RRWPs are associated with SEA heatwaves. Further investigations reveal that the RRWP days having an appropriate phase that facilitates forming a ridge over SEA are associated with SEA heatwaves. The results from Chapters 2 and 3 demonstrate that RRWPs significantly alter the persistence of potentially high-impact surface weather. Therefore, RRWPs should be considered an essential flow feature for understanding and predicting persistent sub-seasonal weather patterns.

RRWPs, blocks, and QRA, the three drivers of persistent weather, have not been studied together so far. Hence, Chapter 4 studies the association of the three drivers in the SH for the austral summer. There is a statistically significant association between RRWPs and QRA events in the SH, where QRA events have higher odds of occurring with an RRWP event than without it. 40% of days that fall under QRA feature high RRWP conditions, referred to as high  $R$ . It implies that QRA events can be composed of transient synoptic-scale RRWPs. Days featuring RRWP reveal similar upper-level flow conditions with high  $R$  days. Therefore, it is argued that the two metrics may capture similar features. For the links with blocks, an insignificant increase in the median area of blocks is seen for high  $R$  days compared with non-high  $R$  days. QRA days reveal an insignificant decrease in the median area of the blocks compared to non-QRA days. The spatial distribution of the blocks supports the decrease in the area of blocks observed for QRA days as it shows significant differences in blocking frequency with high  $R$  days. Essential differences emerge over the Indian Ocean: south of Australia and New Zealand, south of Africa, and in the south Atlantic Ocean. Whereas both QRA and high  $R$  days show an increase in blocking frequency over the south Pacific Ocean.

After establishing the importance of RRWPs, Chapter 5 sets out to find drivers of RRWP events over the North Atlantic for winter and summer. A two-step approach is used where first, the composite maps of meteorological variables for the top-30 RRWP events are used to find the characteristics of RRWP events in winter and summer and their similarities and differences. The maps leading up to the RRWP events, supplemented with theoretical understanding, helped to identify possible causal actors of RRWP events. In a second step, the identified actors are tested for causality in a Causal Network (CN) framework.

The RRWP events for both seasons in the Atlantic show a preferred phasing of the RRWs despite not having an explicit condition for phasing in the event selection. In winter, RRWP events predominantly feature a ridge-trough pattern with a ridge over the Atlantic and a trough over western Europe. In summer, a ridge-trough-ridge pattern emerges with the two ridges over the Atlantic and central Europe. The onset of RRWP events shows a regime change in the atmospheric circulation compared to ten days before the event. An increase in blocking is observed

over the Atlantic with corresponding changes in background flow.

The CNs helped to reveal causal drivers of RRWPs. It shows that changes in blocking over the Atlantic causally drive RRWPs events in the Atlantic. The causal association of blocks with RRWPs may resemble blocks' vital role in modulating the phase of the individual Rossby waves that recur in the same phase forming RRWPs. Also, RRWPs have feedback on the blocks, and background flow, which shows the transient eddies forming a part of RRWPs modifies background flow and helps to sustain blocks. The tropical-extratropical link driving RRWs over the Atlantic exists only in winter, and the link is indirect, where active convection over the subtropical Pacific is one of the actors modulating the background flow over the Atlantic.

This thesis has established that RRWPs are an essential large-scale driver for persistent weather events. Different weather spells can become persistent due to synoptic-scale Rossby waves propagating in the same configuration and influencing the surface weather. Furthermore, the thesis discovered the causal actors of RRWPs over the Atlantic. Local drivers such as blocking and background flow are the primary drivers, and the link with subtropical convection was only observed for winter. The knowledge of the causal drivers helps to further the understanding of RRWPs and can serve as a starting point to test and improve the representation of RRWPs in the models.

## 6.2 Outlook

The field of RRWPs is quite nascent, and several themes can branch out in the direction of understanding the dynamics of RRWPs, forecasting potential of RRWPs, attribution of RRWPs for different types of weather events, and using RRWPs as a predictor. Some future studies that can be undertaken are outlined below:

1. Given the importance of RRWPs for persistent extreme weather, it is natural to ponder how well RRWPs are forecasted? Some studies report forecast errors for extreme events comprised of a single RWP (Glatt and Wirth, 2014). Hence, it may be that RRWP events are also not well forecasted. Furthermore, it should be explored whether ensembles having a better representation of RRWPs provide a more skillful sub-seasonal to seasonal forecasts.
2. Chapter 5 showed that background flow over the Pacific is one of the drivers for RRWP events over the Atlantic in summer at a lag of 3 days. The link is indirect in winter and acts at a lag of 6 days. The upstream link with the Pacific provides a window to predict downstream events. Thus, it could be explored whether this link could be exploited to improve regional forecasts for RRWP events.
3. It is critical to study how RRWPs evolve with climate change. First, it should be evaluated how well climate models simulate RRWPs compared to reanalysis data outputs to quantify

potential model biases. Fei and White (2022) have done some work on this aspect.

4. The differences in RRWP climatology between the Northern and Southern Hemisphere points to the role of orography and planetary waves in generating RRWPs. It can be further extended to combine idealized model simulations to study the role of specific factors such as the role of orography and land-sea contrast.
5. Hovmöller diagrams for several events (e.g., January 2018 case in Ch. 5) showed recurrence across Atlantic and Pacific basins. Furthermore, Riboldi et al. (2022) found that amplified Rossby waves in the Northern hemisphere can stretch across the two storm track regions. Therefore, it is natural to ask how often the RRWP events in the two basins co-occur? This question can be of interest to attribute the effect of RRWPs for spatially compound extremes.
6. The RRWP events identified in the North Atlantic basin (Ch. 5) can be used to identify which harmonics contribute the most during the RRWP events. A space-time spectral analysis (e.g., Riboldi et al., 2022)) can help to answer that. Similar study can be carried out for the North Pacific basin.
7. Unexplored drivers of RRWPs remains to be tested. Case studies have shown that outflow from warm conveyor belts can also be a source of Rossby waves. Similarly, some cases have shown that recurving tropical cyclones can initiate Rossby waves. Furthermore, the role of sea ice has not been explored yet. The role of these variables can be explored in a causal network framework. Moreover, a causal network framework can also be used to explore links with slowly-evolving SST patterns such as El Niño - Southern Oscillation, Pacific Decadal Oscillation, and Indian Ocean dipole.
8. The current metric used to capture RRWPs involves choosing a band of latitudes. The metric does quite well in capturing RRWPs, as demonstrated by the different case studies. However, the current method cannot capture a wave packet in two-dimensional space, i.e., along latitude and longitude. Fragkoulidis and Wirth (2020) developed a method to identify the spatial extent of a wave packet. Their approach can be explored further to identify two-dimensional RWP objects that recur in time.



# Bibliography

- Ali, S. M.: Dataset for Recurrent Rossby wave packets modulate the persistence of dry and wet spells across the globe [dataset], URL <https://doi.org/10.5281/zenodo.4134145>, 2020.
- Ali, S. M. and Pithan, F.: Following moist intrusions into the Arctic using SHEBA observations in a Lagrangian perspective, *Quarterly Journal of the Royal Meteorological Society*, 146, 3522–3533, URL <https://doi.org/10.1002/qj.3859>, 2020.
- Ali, S. M. and Röthlisberger, M.: R-metric [code], URL <https://doi.org/10.5281/zenodo.5742810>, 2021.
- Ali, S. M., Martius, O., and Röthlisberger, M.: Recurrent Rossby wave packets modulate the persistence of dry and wet spells across the globe, *Geophysical Research Letters*, 48, e2020GL091452, URL <https://doi.org/10.1029/2020GL091452>, 2021.
- Ali, S. M., Röthlisberger, M., Parker, T., Kornhuber, K., and Martius, O.: Recurrent Rossby waves during Southeast Australian heatwaves and links to quasi-resonant amplification and atmospheric blocks, *Weather and Climate Dynamics Discussions*, pp. 1–41, URL <https://doi.org/10.5194/wcd-2022-1>, 2022.
- Altenhoff, A. M., Martius, O., Croci-Maspoli, M., Schwierz, C., and Davies, H. C.: Linkage of atmospheric blocks and synoptic-scale Rossby waves: A climatological analysis, *Tellus A: Dynamic Meteorology and Oceanography*, 60, 1053–1063, URL <https://doi.org/10.1111/j.1600-0870.2008.00354.x>, 2008.
- Barnes, E. A., Samarasinghe, S. M., Ebert-Uphoff, I., and Furtado, J. C.: Tropospheric and stratospheric causal pathways between the MJO and NAO, *Journal of Geophysical Research: Atmospheres*, 124, 9356–9371, URL <https://doi.org/10.1029/2019JD031024>, 2019.
- Barriopedro, D., Fischer, E. M., Luterbacher, J., Trigo, R. M., and García-Herrera, R.: The hot summer of 2010: redrawing the temperature record map of Europe, *Science*, 332, 220–224, URL <https://doi.org/10.1126/science.1201224>, 2011.
- Barton, Y., Giannakaki, P., Von Waldow, H., Chevalier, C., Pfahl, S., and Martius, O.: Clustering of regional-scale extreme precipitation events in southern Switzerland, *Monthly Weather Review*, 144, 347–369, URL <https://doi.org/10.1175/MWR-D-15-0205.1>, 2016.

- Barton, Y., Rivoire, P., Koh, J., Ali, S. M., Jérôme, K., and Martius, O.: On the Temporal Clustering of European Extreme Precipitation Events and its Relationship to Persistent and Transient Large-Scale Atmospheric Drivers, *EarthSciRN: Meteorology*, URL <http://dx.doi.org/10.2139/ssrn.4033240>, 2022.
- Benjamini, Y. and Hochberg, Y.: Controlling the false discovery rate: a practical and powerful approach to multiple testing, *Journal of the Royal statistical society: series B (Methodological)*, 57, 289–300, URL <https://doi.org/10.1111/j.2517-6161.1995.tb02031.x>, 1995.
- Blackburn, M., Methven, J., and Roberts, N.: Large-scale context for the UK floods in summer 2007, *Weather*, 63, 280–288, URL <https://centaur.reading.ac.uk/1313/>, 2008.
- Cassou, C.: Intraseasonal interaction between the Madden–Julian oscillation and the North Atlantic Oscillation, *Nature*, 455, 523–527, URL <https://doi.org/10.1038/nature07286>, 2008.
- Charney, J. G.: The dynamics of long waves in a baroclinic westerly current, *Journal of the Atmospheric Sciences*, 4, 136–162, URL [https://doi.org/10.1007/978-1-944970-35-2\\_13](https://doi.org/10.1007/978-1-944970-35-2_13), 1947.
- Coates, L., Haynes, K., O’Brien, J., McAneney, J., and De Oliveira, F. D.: Exploring 167 years of vulnerability: An examination of extreme heat events in Australia 1844–2010, *Environmental Science & Policy*, 42, 33–44, URL <https://doi.org/10.1016/j.envsci.2014.05.003>, 2014.
- Comission, V. B. R.: Final report of the Victorian Bushfires Royal Commission, URL <http://www.royalcommission.vic.gov.au/Commission-Reports>, 2010.
- Coumou, D., Robinson, A., and Rahmstorf, S.: Global increase in record-breaking monthly-mean temperatures, *Climatic Change*, 118, 771–782, URL <https://doi.org/10.1007/s10584-012-0668-1>, 2013.
- Coumou, D., Petoukhov, V., Rahmstorf, S., Petri, S., and Schellnhuber, H. J.: Quasi-resonant circulation regimes and hemispheric synchronization of extreme weather in boreal summer, *Proceedings of the National Academy of Sciences*, 111, 12 331–12 336, URL <https://doi.org/10.1073/pnas.1412797111>, 2014.
- David W. Hosmer, Stanley Lemeshow, S. M.: *Applied Survival Analysis: Regression Modeling of Time-to-Event Data*, Second Edition, John Wiley & Sons, URL <https://doi.org/10.1002/9780470258019>, 2008.
- Davies, H. C.: Weather chains during the 2013/2014 winter and their significance for seasonal prediction, *Nature Geoscience*, 8, 833–837, URL <https://doi.org/10.1038/ngeo2561>, 2015.
- De Vries, A. J.: A global climatological perspective on the importance of Rossby wave breaking and intense moisture transport for extreme precipitation events, *Weather and Climate Dynamics*, 2, 129–161, URL <https://doi.org/10.5194/wcd-2020-44>, 2021.
- de Vries, A. J., Tyrlis, E., Edry, D., Krichak, S., Steil, B., and Lelieveld, J.: Extreme precipitation events in the Middle East: dynamics of the Active Red Sea Trough, *Journal of Geophysical Research: Atmospheres*, 118, 7087–7108, URL <https://doi.org/10.1002/jgrd.50569>, 2013.

- Dee, D. P., Uppala, S. M., Simmons, A. J., Berrisford, P., Poli, P., Kobayashi, S., Andrae, U., Balmaseda, M., Balsamo, G., Bauer, d. P., et al.: The ERA-Interim reanalysis: Configuration and performance of the data assimilation system, *Quarterly Journal of the royal meteorological society*, 137, 553–597, URL <https://doi.org/10.1002/qj.828>, 2011.
- Di Capua, G., Kretschmer, M., Donner, R. V., Van Den Hurk, B., Vellore, R., Krishnan, R., and Coumou, D.: Tropical and mid-latitude teleconnections interacting with the Indian summer monsoon rainfall: a theory-guided causal effect network approach, *Earth System Dynamics*, 11, 17–34, URL <https://esd.copernicus.org/articles/11/17/2020/>, 2020.
- Drouard, M. and Woollings, T.: Contrasting mechanisms of summer blocking over western Eurasia, *Geophysical Research Letters*, 45, 12–040, URL <https://doi.org/10.1029/2018GL079894>, 2018.
- Engel, C. B., Lane, T. P., Reeder, M. J., and Rezny, M.: The meteorology of black Saturday, *Quarterly Journal of the Royal Meteorological Society*, 139, 585–599, URL <https://doi.org/10.1002/qj.1986>, 2013.
- Fang, B. and Lu, M.: Heatwave and blocking in the Northeastern Asia: Occurrence, variability, and association, *Journal of Geophysical Research: Atmospheres*, 125, e2019JD031627, URL <https://doi.org/10.1029/2019JD031627>, 2020.
- Fang, Y., Chen, W., and Zhou, W.: Analysis of the role played by circulation in the persistent precipitation over South China in June 2010, *Advances in Atmospheric Sciences*, 29, 769–781, URL <https://doi.org/10.1007/s00376-012-2018-7>, 2012.
- Fei, C. and White, R. H.: Recurrent Rossby waves in the CESM2: features, precursors and model biases in Northern hemisphere winter, *Journal of Atmospheric Sciences*, under review, 2022.
- Ferranti, L., Corti, S., and Janousek, M.: Flow-dependent verification of the ECMWF ensemble over the Euro-Atlantic sector, *Quarterly Journal of the Royal Meteorological Society*, 141, 916–924, URL <https://doi.org/10.1002/qj.2411>, 2015.
- Fragkoulidis, G. and Wirth, V.: Local Rossby Wave Packet Amplitude, Phase Speed, and Group Velocity: Seasonal Variability and Their Role in Temperature Extremes, *Journal of Climate*, 33, 8767 – 8787, <https://doi.org/10.1175/JCLI-D-19-0377.1>, 2020.
- Fragkoulidis, G., Wirth, V., Bossmann, P., and Fink, A.: Linking Northern Hemisphere temperature extremes to Rossby wave packets, *Quarterly Journal of the Royal Meteorological Society*, 144, 553–566, URL <https://doi.org/10.1002/qj.3228>, 2018.
- Franzke, C. and Feldstein, S. B.: The continuum and dynamics of Northern Hemisphere teleconnection patterns, *Journal of the atmospheric sciences*, 62, 3250–3267, URL <https://doi.org/10.1175/JAS3536.1>, 2005.

- Frederiksen, J.: A unified three-dimensional instability theory of the onset of blocking and cyclogenesis, *Journal of Atmospheric Sciences*, 39, 969–982, URL [https://doi.org/10.1175/1520-0469\(1982\)039<0969:AUTDIT>2.0.CO;2](https://doi.org/10.1175/1520-0469(1982)039<0969:AUTDIT>2.0.CO;2), 1982.
- Frederiksen, J.: A unified three-dimensional instability theory of the onset of blocking and cyclogenesis. II. Teleconnection patterns, *Journal of Atmospheric Sciences*, 40, 2593–2609, URL [https://doi.org/10.1175/1520-0469\(1983\)040<2593:AUTDIT>2.0.CO;2](https://doi.org/10.1175/1520-0469(1983)040<2593:AUTDIT>2.0.CO;2), 1983.
- Fromang, S. and Rivière, G.: The effect of the Madden–Julian Oscillation on the North Atlantic Oscillation using idealized numerical experiments, *Journal of the Atmospheric Sciences*, 77, 1613–1635, URL <https://doi.org/10.1175/JAS-D-19-0178.1>, 2020.
- Funatsu, B. M. and Waugh, D. W.: Connections between potential vorticity intrusions and convection in the eastern tropical Pacific, *Journal of the Atmospheric Sciences*, 65, 987–1002, URL <https://doi.org/10.1175/2007JAS2248.1>, 2008.
- Gerhardus, A. and Runge, J.: High-recall causal discovery for autocorrelated time series with latent confounders, *Advances in Neural Information Processing Systems*, 33, 12 615–12 625, URL <https://proceedings.neurips.cc/paper/2020/file/94e70705efae423efda1088614128d0b-Paper.pdf>, 2020.
- Ghil, M. and Mo, K.: Intraseasonal oscillations in the global atmosphere. Part I: Northern Hemisphere and tropics, *Journal of Atmospheric Sciences*, 48, 752–779, URL [https://doi.org/10.1175/1520-0469\(1991\)048<0752:IOITGA>2.0.CO;2](https://doi.org/10.1175/1520-0469(1991)048<0752:IOITGA>2.0.CO;2), 1991.
- Glatt, I. and Wirth, V.: Identifying Rossby wave trains and quantifying their properties, *Quarterly Journal of the Royal Meteorological Society*, 140, 384–396, URL <https://doi.org/10.1002/qj.2139>, 2014.
- Grams, C. M., Wernli, H., Böttcher, M., Čampa, J., Corsmeier, U., Jones, S. C., Keller, J. H., Lenz, C.-J., and Wiegand, L.: The key role of diabatic processes in modifying the upper-tropospheric wave guide: a North Atlantic case-study, *Quarterly Journal of the Royal Meteorological Society*, 137, 2174–2193, URL <https://doi.org/10.1002/qj.891>, 2011.
- Green, J. S. A.: THE WEATHER DURING JULY 1976: SOME DYNAMICAL CONSIDERATIONS OF THE DROUGHT, *Weather*, 32, 120–126, URL <https://doi.org/10.1002/j.1477-8696.1977.tb04532.x>, 1977.
- Hamill, T. M. and Kiladis, G. N.: Skill of the MJO and Northern Hemisphere blocking in GEFS medium-range reforecasts, *Monthly Weather Review*, 142, 868–885, URL <https://doi.org/10.1175/MWR-D-13-00199.1>, 2014.
- Handmer, J., Honda, Y., Kundzewicz, Z. W., Arnell, N., Benito, G., Hatfield, J., Mohamed, I. F., Peduzzi, P., Wu, S., Sherstyukov, B., et al.: Changes in impacts of climate extremes: human systems and ecosystems, in: Managing the risks of extreme events and disasters to advance climate change adaptation: Special report of the Intergovernmental Panel on Climate Change,

- edited by Field, C. B., Barros, V., Stocker, T. F., and Dahe, Q., pp. 231–290, Cambridge University Press, URL <https://doi.org/10.1017/CBO9781139177245.007>, 2012.
- Hersbach, H., Bell, B., Berrisford, P., Hirahara, S., Horányi, A., Muñoz-Sabater, J., Nicolas, J., Peubey, C., Radu, R., Schepers, D., et al.: The ERA5 global reanalysis, *Quarterly Journal of the Royal Meteorological Society*, 146, 1999–2049, URL <https://doi.org/10.1002/qj.3803>, 2020.
- Hoskins, B. and Woollings, T.: Persistent extratropical regimes and climate extremes, *Current Climate Change Reports*, 1, 115–124, URL <https://doi.org/10.1007/s40641-015-0020-8>, 2015.
- Hoskins, B. J. and Ambrizzi, T.: Rossby wave propagation on a realistic longitudinally varying flow, *Journal of Atmospheric Sciences*, 50, 1661–1671, URL [https://doi.org/10.1175/1520-0469\(1993\)050\(1661:RWPOAR\)2.0.CO;2](https://doi.org/10.1175/1520-0469(1993)050(1661:RWPOAR)2.0.CO;2), 1993.
- Hoskins, B. J. and Sardeshmukh, P. D.: A diagnostic study of the dynamics of the northern hemisphere winter of 1985–86, *Quarterly Journal of the Royal Meteorological Society*, 113, 759–778, URL <https://doi.org/10.1002/qj.49711347705>, 1987.
- Hoyer, S. and Hamman, J.: xarray: ND labeled arrays and datasets in Python, *Journal of Open Research Software*, 5, URL <http://doi.org/10.5334/jors.148>, 2017.
- Hughes, L., Steffen, W., Mullins, G., Dean, A., Weisbrot, E., and Rice, M.: Summer of crisis, 2020.
- Hunter, J. D.: Matplotlib: A 2D graphics environment, *Computing in science & engineering*, 9, 90–95, URL <https://ieeecomputersociety.org/10.1109/MCSE.2007.55>, 2007.
- Johnson, N. C. and Feldstein, S. B.: The continuum of North Pacific sea level pressure patterns: Intraseasonal, interannual, and interdecadal variability, *Journal of Climate*, 23, 851–867, URL <https://doi.org/10.1175/2009JCLI3099.1>, 2010.
- Karoly, D. J.: The recent bushfires and extreme heat wave in southeast Australia, *Bull Aust Meteorol Oceanogr Soc*, 22, 10–13, 2009.
- Kautz, L.-A., Martius, O., Pfahl, S., Pinto, J. G., Ramos, A. M., Sousa, P. M., and Woollings, T.: Atmospheric blocking and weather extremes over the Euro-Atlantic sector—a review, *Weather and Climate Dynamics*, 3, 305–336, URL <https://doi.org/10.5194/wcd-3-305-2022>, 2022.
- Keller, J. H., Grams, C. M., Riemer, M., Archambault, H. M., Bosart, L., Doyle, J. D., Evans, J. L., Galarneau, T. J., Griffin, K., Harr, P. A., et al.: The extratropical transition of tropical cyclones. Part II: Interaction with the midlatitude flow, downstream impacts, and implications for predictability, *Monthly Weather Review*, 147, 1077–1106, URL <https://doi.org/10.1175/MWR-D-17-0329.1>, 2019.
- King, M. J. and Reeder, M. J.: Extreme heat events from an object viewpoint with application to south-east Australia, *International journal of climatology*, 41, 2693–2709, URL <https://doi.org/10.1002/joc.6984>, 2021.

- Kluyver, T., Ragan-Kelley, B., Pérez, F., Granger, B. E., Bussonnier, M., Frederic, J., Kelley, K., Hamrick, J. B., Grout, J., Corlay, S., et al.: Jupyter Notebooks-a publishing format for reproducible computational workflows., vol. 2016, URL <https://jupyter.org/>, 2016.
- Kopp, J., Rivoire, P., Ali, S. M., Barton, Y., and Martius, O.: A novel method to identify sub-seasonal clustering episodes of extreme precipitation events and their contributions to large accumulation periods, *Hydrology and earth system sciences*, 25, 5153–5174, URL <https://hess.copernicus.org/articles/25/5153/2021/>, 2021.
- Kornhuber, K., Petoukhov, V., Karoly, D., Petri, S., Rahmstorf, S., and Coumou, D.: Summer-time planetary wave resonance in the Northern and Southern Hemispheres, *Journal of Climate*, 30, 6133–6150, URL <https://doi.org/10.1175/JCLI-D-16-0703.1>, 2017a.
- Kornhuber, K., Petoukhov, V., Petri, S., Rahmstorf, S., and Coumou, D.: Evidence for wave resonance as a key mechanism for generating high-amplitude quasi-stationary waves in boreal summer, *Climate Dynamics*, 49, 1961–1979, URL <https://doi.org/10.1007/s00382-016-3399-6>, 2017b.
- Kornhuber, K., Osprey, S., Coumou, D., Petri, S., Petoukhov, V., Rahmstorf, S., and Gray, L.: Extreme weather events in early summer 2018 connected by a recurrent hemispheric wave-7 pattern, *Environmental Research Letters*, 14, 054 002, URL <https://iopscience.iop.org/article/10.1088/1748-9326/ab13bf>, 2019.
- Kornhuber, K., Coumou, D., Vogel, E., Lesk, C., Donges, J. F., Lehmann, J., and Horton, R. M.: Amplified Rossby waves enhance risk of concurrent heatwaves in major breadbasket regions, *Nature Climate Change*, 10, 48–53, URL <https://doi.org/10.1038/s41558-019-0637-z>, 2020.
- Kretschmer, M., Coumou, D., Donges, J. F., and Runge, J.: Using causal effect networks to analyze different Arctic drivers of midlatitude winter circulation, *Journal of climate*, 29, 4069–4081, URL <https://doi.org/10.1175/JCLI-D-15-0654.1>, 2016.
- Kretschmer, M., Adams, S. V., Arribas, A., Prudden, R., Robinson, N., Saggioro, E., and Shepherd, T. G.: Quantifying causal pathways of teleconnections, *Bulletin of the American Meteorological Society*, 102, E2247–E2263, URL <https://doi.org/10.1175/BAMS-D-20-0117.1>, 2021.
- Lenggenhager, S., Croci-Maspoli, M., Brönnimann, S., and Martius, O.: On the dynamical coupling between atmospheric blocks and heavy precipitation events: A discussion of the southern Alpine flood in October 2000, *Quarterly Journal of the Royal Meteorological Society*, 145, 530–545, URL <https://doi.org/10.1002/qj.3449>, 2019.
- Li, M., Luo, D., Yao, Y., and Zhong, L.: Large-scale atmospheric circulation control of summer extreme hot events over China, *International Journal of Climatology*, 40, 1456–1476, URL <https://doi.org/10.1002/joc.6279>, 2020.
- Lin, H., Brunet, G., and Derome, J.: An observed connection between the North Atlantic Oscillation and the Madden–Julian oscillation, *Journal of Climate*, 22, 364–380, URL <https://doi.org/10.1175/2008JCLI2515.1>, 2009.

- Lindzen, R. and Farrell, B.: A simple approximate result for the maximum growth rate of baroclinic instabilities, *Journal of the atmospheric sciences*, 37, 1648–1654, URL [https://doi.org/10.1175/1520-0469\(1980\)037<1648:ASARFT>2.0.CO;2](https://doi.org/10.1175/1520-0469(1980)037<1648:ASARFT>2.0.CO;2), 1980.
- Liu, A., Liu, H., Li, T., Karimi-Bidhendi, S., Yue, Y., and Anandkumar, A.: Disentangling observed causal effects from latent confounders using method of moments, *arXiv preprint arXiv:2101.06614*, 2021.
- Lukens, K. E., Feldstein, S. B., Yoo, C., and Lee, S.: The dynamics of the extratropical response to Madden–Julian Oscillation convection, *Quarterly Journal of the Royal Meteorological Society*, 143, 1095–1106, URL <https://doi.org/10.1002/qj.2993>, 2017.
- Ma, J. and San Liang, X.: Multiscale dynamical processes underlying the wintertime Atlantic blockings, *Journal of the Atmospheric Sciences*, 74, 3815–3831, URL <https://doi.org/10.1175/JAS-D-16-0295.1>, 2017.
- Marshall, A., Hudson, D., Wheeler, M., Alves, O., Hendon, H., Pook, M., and Risbey, J.: Intra-seasonal drivers of extreme heat over Australia in observations and POAMA-2, *Climate dynamics*, 43, 1915–1937, URL <https://doi.org/10.1007/s00382-013-2016-1>, 2014.
- Martius, O., Wehrli, K., and Rohrer, M.: Local and remote atmospheric responses to soil moisture anomalies in Australia, *Journal of Climate*, 34, 9115–9131, <https://doi.org/https://doi.org/10.1175/JCLI-D-21-0130.1>, 2021.
- Masson-Delmotte, V., Zhai, P., Pirani, A., Connors, S. L., Péan, C., Berger, S., Caud, N., Chen, Y., Goldfarb, L., Gomis, M., et al.: Climate change 2021: the physical science basis, Contribution of working group I to the sixth assessment report of the intergovernmental panel on climate change, p. 2, URL <https://www.ipcc.ch/report/ar6/wg1/>, 2021.
- Matsueda, M. and Palmer, T.: Estimates of flow-dependent predictability of wintertime Euro-Atlantic weather regimes in medium-range forecasts, *Quarterly Journal of the Royal Meteorological Society*, 144, 1012–1027, URL <https://doi.org/10.1002/qj.3265>, 2018.
- Matthews, A. J. and Kiladis, G. N.: The tropical–extratropical interaction between high-frequency transients and the Madden–Julian oscillation, *Monthly weather review*, 127, 661–677, URL [https://doi.org/10.1175/1520-0493\(1999\)127<0661:TTEIBH>2.0.CO;2](https://doi.org/10.1175/1520-0493(1999)127<0661:TTEIBH>2.0.CO;2), 1999.
- McTaggart-Cowan, R., Deane, G. D., Bosart, L. F., Davis, C. A., and Galarneau Jr, T. J.: Climatology of tropical cyclogenesis in the North Atlantic (1948–2004), *Monthly Weather Review*, 136, 1284–1304, URL <https://doi.org/10.1175/2007MWR2245.1>, 2008.
- Meyer, L.: Analysing Potential Drivers of Recurrent Rossby Wave Packets using Causal Inference [thesis], URL <https://occrdata.unibe.ch/students/theses/msc/361.pdf>, 2022.
- Michelangeli, P.-A., Vautard, R., and Legras, B.: Weather regimes: Recurrence and quasi stationarity, *Journal of the atmospheric sciences*, 52, 1237–1256, URL [https://doi.org/10.1175/1520-0469\(1995\)052<1237:WRRAS>2.0.CO;2](https://doi.org/10.1175/1520-0469(1995)052<1237:WRRAS>2.0.CO;2), 1995.

- Moore, R. W., Martius, O., and Spengler, T.: The modulation of the subtropical and extratropical atmosphere in the Pacific basin in response to the Madden–Julian oscillation, *Monthly Weather Review*, 138, 2761–2779, URL <https://doi.org/10.1175/2010MWR3194.1>, 2010.
- Mooring, T. and Linz, M.: Investigating quasi-resonant Rossby waves with an idealized general circulation model, in: *EGU General Assembly Conference Abstracts*, p. 12992, URL <https://doi.org/10.5194/egusphere-egu2020-12992>, 2020.
- Nakamura, N. and Huang, C. S.: Atmospheric blocking as a traffic jam in the jet stream, *Science*, 361, 42–47, URL <https://www.science.org/doi/full/10.1126/science.aat0721>, 2018.
- Novak, L., Ambaum, M. H., and Tailleux, R.: The life cycle of the North Atlantic storm track, *Journal of the Atmospheric Sciences*, 72, 821–833, URL <https://doi.org/10.1175/JAS-D-14-0082.1>, 2015.
- O’Brien, L. and Reeder, M. J.: Southern Hemisphere summertime Rossby waves and weather in the Australian region, *Quarterly Journal of the Royal Meteorological Society*, 143, 2374–2388, URL <https://doi.org/10.1002/qj.3090>, 2017.
- O’Kane, T. J., Risbey, J. S., Monselesan, D. P., Horenko, I., and Franzke, C. L.: On the dynamics of persistent states and their secular trends in the waveguides of the Southern Hemisphere troposphere, *Climate dynamics*, 46, 3567–3597, URL <https://doi.org/10.1007/s00382-015-2786-8>, 2016.
- Papritz, L. and Dunn-Sigouin, E.: What configuration of the atmospheric circulation drives extreme net and total moisture transport into the Arctic, *Geophysical Research Letters*, 47, e2020GL089769, URL <https://doi.org/10.1029/2020GL089769>, 2020.
- Parker, T., Quinting, J., and Reeder, M.: The synoptic-dynamics of summertime heatwaves in the Sydney area (Australia), *Journal of Southern Hemisphere Earth Systems Science*, 69, 116–130, URL <https://doi.org/10.1071/ES19004>, 2020.
- Parker, T. J., Berry, G. J., and Reeder, M. J.: The structure and evolution of heat waves in southeastern Australia, *Journal of Climate*, 27, 5768–5785, URL <https://doi.org/10.1175/JCLI-D-13-00740.1>, 2014a.
- Parker, T. J., Berry, G. J., Reeder, M. J., and Nicholls, N.: Modes of climate variability and heat waves in Victoria, southeastern Australia, *Geophysical Research Letters*, 41, 6926–6934, URL <https://doi.org/10.1002/2014GL061736>, 2014b.
- Pearl, J.: Causal inference in statistics: An overview, *Statistics surveys*, 3, 96–146, URL <https://doi.org/10.1214/09-SS057>, 2009.
- Pelly, J. L. and Hoskins, B. J.: A new perspective on blocking, *Journal of the atmospheric sciences*, 60, 743–755, URL [https://doi.org/10.1175/1520-0469\(2003\)060<0743:ANPOB>2.0.CO;2](https://doi.org/10.1175/1520-0469(2003)060<0743:ANPOB>2.0.CO;2), 2003.



- Perkins-Kirkpatrick, S. and Lewis, S.: Increasing trends in regional heatwaves, *Nature communications*, 11, 1–8, URL <https://doi.org/10.1038/s41467-020-16970-7>, 2020.
- Petoukhov, V., Rahmstorf, S., Petri, S., and Schellnhuber, H. J.: Quasiresonant amplification of planetary waves and recent Northern Hemisphere weather extremes, *Proceedings of the National Academy of Sciences*, 110, 5336–5341, URL <https://doi.org/10.1073/pnas.1222000110>, 2013.
- Pfahl, S. and Wernli, H.: Quantifying the relevance of atmospheric blocking for co-located temperature extremes in the Northern Hemisphere on (sub-) daily time scales, *Geophysical Research Letters*, 39, URL <https://doi.org/10.1029/2012GL052261>, 2012.
- Pierrehumbert, R. and Swanson, K.: Baroclinic instability, *Annual review of fluid mechanics*, 27, 419–467, 1995.
- Quandt, L.-A., Keller, J. H., Martius, O., and Jones, S. C.: Forecast variability of the blocking system over Russia in summer 2010 and its impact on surface conditions, *Weather and Forecasting*, 32, 61–82, <https://doi.org/https://doi.org/10.1175/WAF-D-16-0065.1>, 2017.
- Quinting, J., Parker, T., and Reeder, M.: Two synoptic routes to subtropical heat waves as illustrated in the Brisbane region of Australia, *Geophysical Research Letters*, 45, 10–700, URL <https://doi.org/10.1029/2018GL079261>, 2018.
- Quinting, J. F. and Jones, S. C.: On the impact of tropical cyclones on Rossby wave packets: A climatological perspective, *Monthly Weather Review*, 144, 2021–2048, URL <https://doi.org/10.1175/MWR-D-14-00298.1>, 2016.
- Quinting, J. F. and Reeder, M. J.: Southeastern Australian heat waves from a trajectory viewpoint, *Monthly Weather Review*, 145, 4109–4125, URL <https://doi.org/10.1175/MWR-D-17-0165.1>, 2017.
- Raymond, C., Horton, R. M., Zscheischler, J., Martius, O., AghaKouchak, A., Balch, J., Bowen, S. G., Camargo, S. J., Hess, J., Kornhuber, K., et al.: Understanding and managing connected extreme events, *Nature climate change*, 10, 611–621, URL <https://doi.org/10.1038/s41558-020-0790-4>, 2020.
- Rex, D. F.: Blocking action in the middle troposphere and its effect upon regional climate, *Tellus*, 2, 275–301, URL <https://doi.org/10.3402/tellusa.v2i4.8603>, 1950.
- Rhines, P.: DYNAMICAL METEOROLOGY — Rossby Waves, in: *Encyclopedia of Atmospheric Sciences (Second Edition)*, edited by North, G. R., Pyle, J., and Zhang, F., pp. 404–416, Academic Press, Oxford, second edition edn., URL <https://doi.org/10.1016/B978-0-12-382225-3.00346-7>, 2015.
- Rhodes, R. I.: Clustering and stalling of North Atlantic cyclones: The influence on precipitation in England and wales [thesis], Doctoral dissertation, URL <http://centaur.reading.ac.uk/77911/>, 2017.

- Riboldi, J., Grams, C. M., Riemer, M., and Archambault, H. M.: A phase locking perspective on Rossby wave amplification and atmospheric blocking downstream of recurving western North Pacific tropical cyclones, *Monthly Weather Review*, 147, 567–589, URL <https://doi.org/10.1175/MWR-D-18-0271.1>, 2019.
- Riboldi, J., Rousi, E., D’Andrea, F., Rivière, G., and Lott, F.: Circumglobal Rossby wave patterns during boreal winter highlighted by space–time spectral analysis, *Weather and Climate Dynamics*, 3, 449–469, URL <https://doi.org/10.5194/wcd-2021-59>, 2022.
- Risbey, J. S., O’Kane, T. J., Monselesan, D. P., Franzke, C. L., and Horenko, I.: On the dynamics of austral heat waves, *Journal of Geophysical Research: Atmospheres*, 123, 38–57, URL <https://doi.org/10.1002/2017JD027222>, 2018.
- Risser, M. D. and Wehner, M. F.: Attributable human-induced changes in the likelihood and magnitude of the observed extreme precipitation during Hurricane Harvey, *Geophysical Research Letters*, 44, 12–457, URL <https://doi.org/10.1002/2017GL075888>, 2017.
- Rohrer, M., Brönnimann, S., Martius, O., Raible, C. C., Wild, M., and Compo, G. P.: Representation of extratropical cyclones, blocking anticyclones, and Alpine circulation types in multiple reanalyses and model simulations, *Journal of Climate*, 31, 3009–3031, URL <https://doi.org/10.1175/JCLI-D-17-0350.1>, 2018.
- Rohrer, M., Martius, O., Raible, C., and Brönnimann, S.: Sensitivity of blocks and cyclones in ERA5 to spatial resolution and definition, *Geophysical Research Letters*, 47, e2019GL085582, 2020.
- Röthlisberger, M. and Martius, O.: Quantifying the local effect of Northern Hemisphere atmospheric blocks on the persistence of summer hot and dry spells, *Geophysical Research Letters*, 46, 10 101–10 111, URL <https://doi.org/10.1029/2019GL083745>, 2019.
- Röthlisberger, M., Martius, O., and Wernli, H.: Northern Hemisphere Rossby wave initiation events on the extratropical jet—A climatological analysis, *Journal of Climate*, 31, 743–760, URL <https://doi.org/10.1175/JCLI-D-17-0346.1>, 2018.
- Röthlisberger, M., Frossard, L., Bosart, L. F., Keyser, D., and Martius, O.: Recurrent synoptic-scale Rossby wave patterns and their effect on the persistence of cold and hot spells, *Journal of Climate*, 32, 3207–3226, URL <https://doi.org/10.1175/JCLI-D-18-0664.1>, 2019.
- Rudd, A. C., Kay, A. L., Wells, S. C., Aldridge, T., Cole, S. J., Kendon, E. J., and Stewart, E. J.: Investigating potential future changes in surface water flooding hazard and impact, *Hydrological Processes*, 34, 139–149, URL <https://doi.org/10.1002/hyp.13572>, 2020.
- Runge, J.: Causal network reconstruction from time series: From theoretical assumptions to practical estimation, *Chaos: An Interdisciplinary Journal of Nonlinear Science*, 28, 075310, URL <https://doi.org/10.1063/1.5025050>, 2018.

- Runge, J., Bathiany, S., Bollt, E., Camps-Valls, G., Coumou, D., Deyle, E., Glymour, C., Kretschmer, M., Mahecha, M. D., Muñoz-Marí, J., et al.: Inferring causation from time series in Earth system sciences, *Nature communications*, 10, 1–13, URL <https://doi.org/10.1038/s41467-019-10105-3>, 2019a.
- Runge, J., Nowack, P., Kretschmer, M., Flaxman, S., and Sejdinovic, D.: Detecting and quantifying causal associations in large nonlinear time series datasets, *Science advances*, 5, eaau4996, URL <https://www.science.org/doi/full/10.1126/sciadv.aau4996>, 2019b.
- Saggioro, E. and Shepherd, T. G.: Quantifying the Timescale and Strength of Southern Hemisphere Intraseasonal Stratosphere-troposphere Coupling, *Geophysical research letters*, 46, 13 479–13 487, URL <https://doi.org/10.1029/2019GL084763>, 2019.
- Sardeshmukh, P. D. and Hoskins, B. J.: The generation of global rotational flow by steady idealized tropical divergence, *Journal of the Atmospheric Sciences*, 45, 1228–1251, URL [https://doi.org/10.1175/1520-0469\(1988\)045<1228:TGOGRF>2.0.CO;2](https://doi.org/10.1175/1520-0469(1988)045<1228:TGOGRF>2.0.CO;2), 1988.
- Schaller, N., Kay, A. L., Lamb, R., Massey, N. R., Van Oldenborgh, G. J., Otto, F. E., Sparrow, S. N., Vautard, R., Yiou, P., Ashpole, I., et al.: Human influence on climate in the 2014 southern England winter floods and their impacts, *Nature Climate Change*, 6, 627–634, URL <https://doi.org/10.1038/nclimate2927>, 2016.
- Schwierz, C., Croci-Maspoli, M., and Davies, H.: Perspicacious indicators of atmospheric blocking, *Geophysical research letters*, 31, URL <https://doi.org/10.1029/2003GL019341>, 2004.
- Seneviratne, S. I., Corti, T., Davin, E. L., Hirschi, M., Jaeger, E. B., Lehner, I., Orlowsky, B., and Teuling, A. J.: Investigating soil moisture–climate interactions in a changing climate: A review, *Earth-Science Reviews*, 99, 125–161, URL <https://doi.org/10.1016/j.earscirev.2010.02.004>, 2010.
- Shepherd, T. G.: Atmospheric circulation as a source of uncertainty in climate change projections, *Nature Geoscience*, 7, 703–708, URL <https://doi.org/10.1038/ngeo2253>, 2014.
- Shutts, G.: The propagation of eddies in diffluent jetstreams: Eddy vorticity forcing of ‘blocking’ flow fields, *Quarterly Journal of the Royal Meteorological Society*, 109, 737–761, URL <https://doi.org/10.1002/qj.49710946204>, 1983.
- Simmonds, I. and Lim, E.-P.: Biases in the calculation of Southern Hemisphere mean baroclinic eddy growth rate, *Geophysical Research Letters*, 36, URL <https://doi.org/10.1029/2008GL036320>, 2009.
- Sivakumar, M. V.: Climate extremes and impacts on agriculture, *Agroclimatology: Linking Agriculture to Climate*, 60, 621–647, URL <https://doi.org/10.2134/agronmonogr60.2018.0006>, 2020.

- Stadtherr, L., Coumou, D., Petoukhov, V., Petri, S., and Rahmstorf, S.: Record Balkan floods of 2014 linked to planetary wave resonance, *Science advances*, 2, e1501428, URL <https://doi.org/10.1126/sciadv.1501428>, 2016.
- Stan, C., Straus, D. M., Frederiksen, J. S., Lin, H., Maloney, E. D., and Schumacher, C.: Review of tropical-extratropical teleconnections on intraseasonal time scales, *Reviews of Geophysics*, 55, 902–937, URL <https://doi.org/10.1002/2016RG000538>, 2017.
- Straus, D. M., Swenson, E., and Lappen, C.-L.: The MJO cycle forcing of the North Atlantic circulation: Intervention experiments with the Community Earth System Model, *Journal of the Atmospheric Sciences*, 72, 660–681, URL <https://doi.org/10.1175/JAS-D-14-0145.1>, 2015.
- Teng, H., Branstator, G., Meehl, G. A., and Washington, W. M.: Projected intensification of subseasonal temperature variability and heat waves in the Great Plains, *Geophysical Research Letters*, 43, 2165–2173, URL <https://doi.org/10.1002/2015GL067574>, 2016.
- Trenberth, K. E., Branstator, G. W., Karoly, D., Kumar, A., Lau, N.-C., and Ropelewski, C.: Progress during TOGA in understanding and modeling global teleconnections associated with tropical sea surface temperatures, *Journal of Geophysical Research: Oceans*, 103, 14 291–14 324, URL <https://doi.org/10.1029/97JC01444>, 1998.
- Uotila, P., Vihma, T., and Tsukernik, M.: Close interactions between the Antarctic cyclone budget and large-scale atmospheric circulation, *Geophysical Research Letters*, 40, 3237–3241, URL <https://doi.org/10.1002/grl.50560>, 2013.
- Vijverberg, S. and Coumou, D.: The role of the Pacific Decadal Oscillation and ocean-atmosphere interactions in driving US temperature variability, *npj Climate and Atmospheric Science*, 5, 1–11, URL <https://doi.org/10.1038/s41612-022-00237-7>, 2022.
- Webster, P., Toma, V. E., and Kim, H.-M.: Were the 2010 Pakistan floods predictable?, *Geophysical research letters*, 38, URL <https://doi.org/10.1029/2010GL046346>, 2011.
- Wehrli, K., Guillod, B. P., Hauser, M., Leclair, M., and Seneviratne, S. I.: Identifying key driving processes of major recent heat waves, *Journal of Geophysical Research: Atmospheres*, 124, 11 746–11 765, URL <https://doi.org/10.1029/2019JD030635>, 2019.
- Wernli, H. and Schwierz, C.: Surface cyclones in the ERA-40 dataset (1958–2001). Part I: Novel identification method and global climatology, *Journal of the atmospheric sciences*, 63, 2486–2507, URL <https://doi.org/10.1175/JAS3766.1>, 2006.
- White, R. H., Kornhuber, K., Martius, O., and Wirth, V.: From Atmospheric Waves to Heatwaves: A Waveguide Perspective for Understanding and Predicting Concurrent, Persistent, and Extreme Extratropical Weather, *Bulletin of the American Meteorological Society*, 103, E923–E935, URL <https://doi.org/10.1175/BAMS-D-21-0170.1>, 2022.

- Wilks, D.: “The stippling shows statistically significant grid points”: How research results are routinely overstated and overinterpreted, and what to do about it, *Bulletin of the American Meteorological Society*, 97, 2263–2273, URL <https://doi.org/10.1175/BAMS-D-15-00267.1>, 2016.
- Wirth, V. and Polster, C.: The problem of diagnosing jet waveguidability in the presence of large-amplitude eddies, *Journal of the Atmospheric Sciences*, 78, 3137–3151, URL <https://doi.org/10.1175/JAS-D-20-0292.1>, 2021.
- Wolf, G., Brayshaw, D. J., Klingaman, N. P., and Czaja, A.: Quasi-stationary waves and their impact on European weather and extreme events, *Quarterly Journal of the Royal Meteorological Society*, 144, 2431–2448, URL <https://doi.org/10.1002/qj.3310>, 2018.
- Wolter, K., Hoerling, M., Eischeid, J. K., van Oldenborgh, G. J., Quan, X.-W., Walsh, J. E., Chase, T. N., and Dole, R. M.: How unusual was the cold winter of 2013/14 in the Upper Midwest?, *Bulletin of the American Meteorological Society*, 96, S10–S14, URL <https://doi.org/10.1175/BAMS-D-15-00126.1>, 2015.
- Wu, P.: Nonlinear resonance and instability of planetary waves and low-frequency variability in the atmosphere, *Journal of Atmospheric Sciences*, 50, 3590–3607, URL [https://doi.org/10.1175/1520-0469\(1993\)050<3590:NRAIOP>2.0.CO;2](https://doi.org/10.1175/1520-0469(1993)050<3590:NRAIOP>2.0.CO;2), 1993.
- Xu, P., Wang, L., Liu, Y., Chen, W., and Huang, P.: The record-breaking heat wave of June 2019 in Central Europe, *Atmospheric Science Letters*, 21, e964, URL <https://doi.org/10.1002/asl.964>, 2020.
- Zhang, Z.: Parametric regression model for survival data: Weibull regression model as an example, *Annals of translational medicine*, 4, URL <https://doi.org/10.21037/atm.2016.08.45>, 2016.
- Zimin, A. V., Szunyogh, I., Patil, D., Hunt, B. R., and Ott, E.: Extracting envelopes of Rossby wave packets, *Monthly weather review*, 131, 1011–1017, URL [https://doi.org/10.1175/1520-0493\(2003\)131\(1011:EEORWP\)2.0.CO;2](https://doi.org/10.1175/1520-0493(2003)131(1011:EEORWP)2.0.CO;2), 2003.
- Zschenderlein, P., Pfahl, S., Wernli, H., and Fink, A. H.: A Lagrangian analysis of upper-tropospheric anticyclones associated with heat waves in Europe, *Weather and Climate Dynamics*, 1, 191–206, URL <https://doi.org/10.5194/wcd-1-191-2020>, 2020.



## Appendix A

# Supporting Information for Recurrent Rossby wave packets modulate the persistence of dry and wet spells across the globe

### A.1 Spell count and median for Dry Spells and Wet Spells

Figures A.1 and A.2 show spell counts and the median spell duration for dry spells where each spell has a minimum duration of 5 days. The yellow solid contours show regions having fewer than 40 dry spells and are excluded from the analysis. They are either the arid regions in the subtropics and poles, which have long running dry spells, or the wet regions in the tropics, which don't have more than 40 dry spells having a minimum duration of 5 days. These regions are excluded from the regression model analysis. Thus, they appear as hatches in the figures showing the acceleration factors (Figures 2.5 and 2.6). Several regions in both hemispheres have a median spell length of less than 5 days, which is less than the minimum spell length threshold used in this study.

Similarly, figures A.3 and A.4 show spell counts and the median spell duration for wet spells where each spell has a minimum duration of 5 days. Several areas in the subtropical and the polar region are usually dry, and thus have fewer than 40 spells and are excluded from the analysis. In the tropics the median wet spell duration is longest (A.4). The storm-track regions of both the Northern and the Southern hemisphere experience long wet spells during their respective winter seasons.

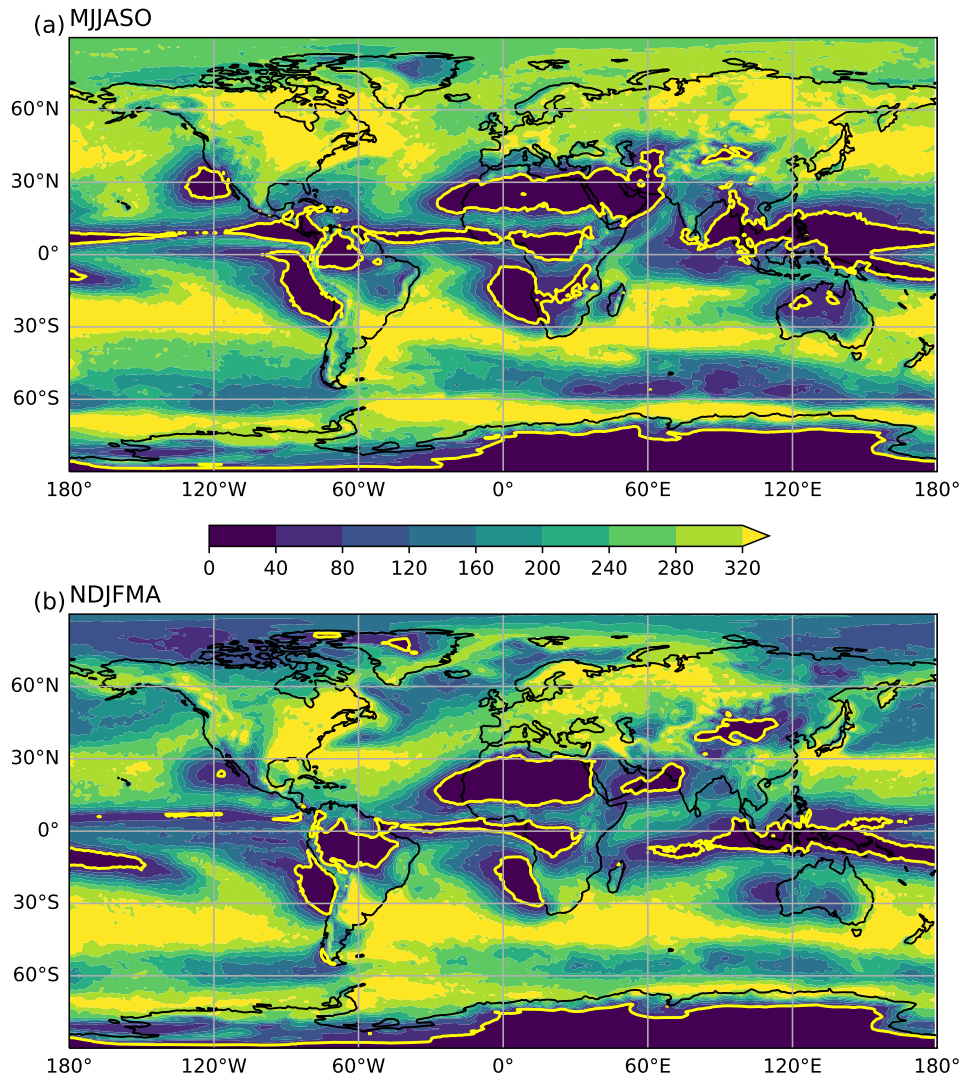


Figure A.1: Total number of MJJASO and NDJFMA dry spells (color shading) having a minimum spell length of 5 days. Solid yellow contours show areas with fewer than 40 spells between 1980-2016.



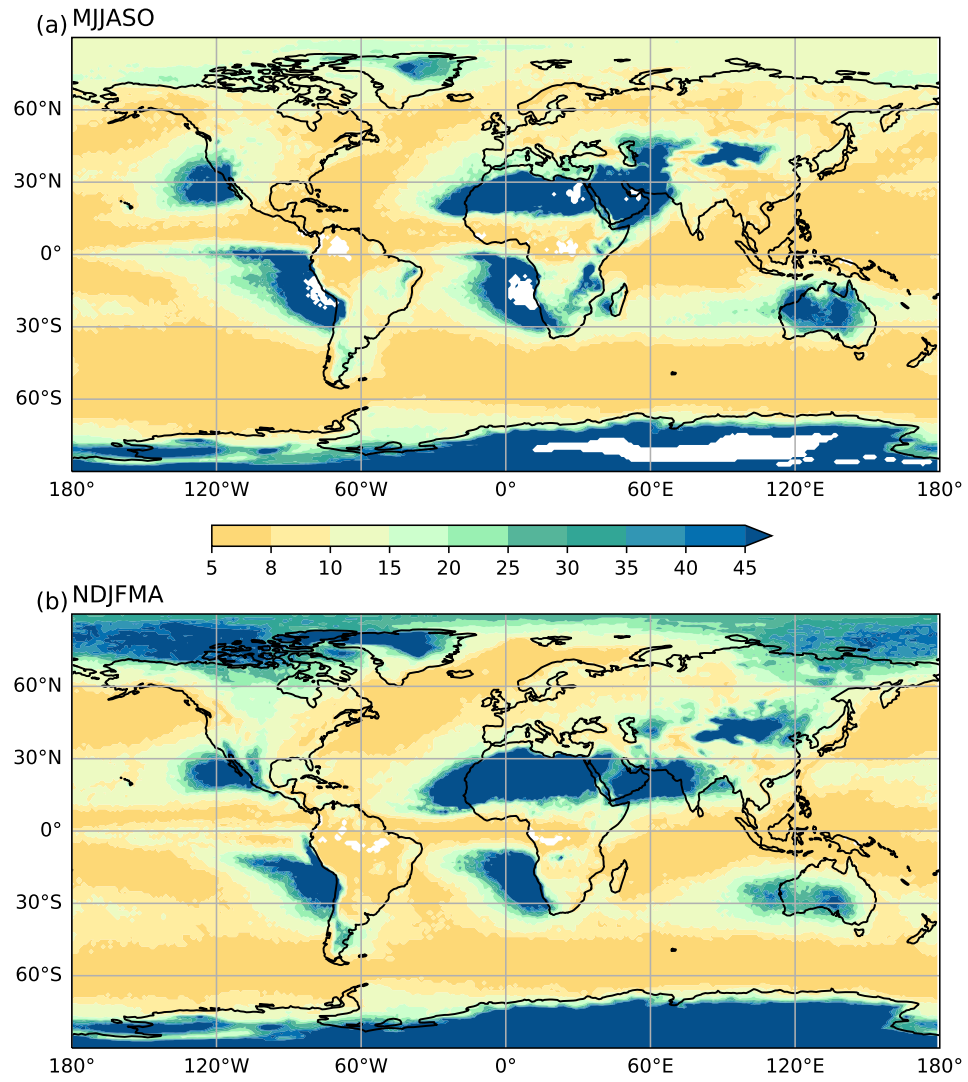


Figure A.2: Median MJJASO and NDJFMA dry spell length (color shading) for areas having a minimum spell duration of 5 days.

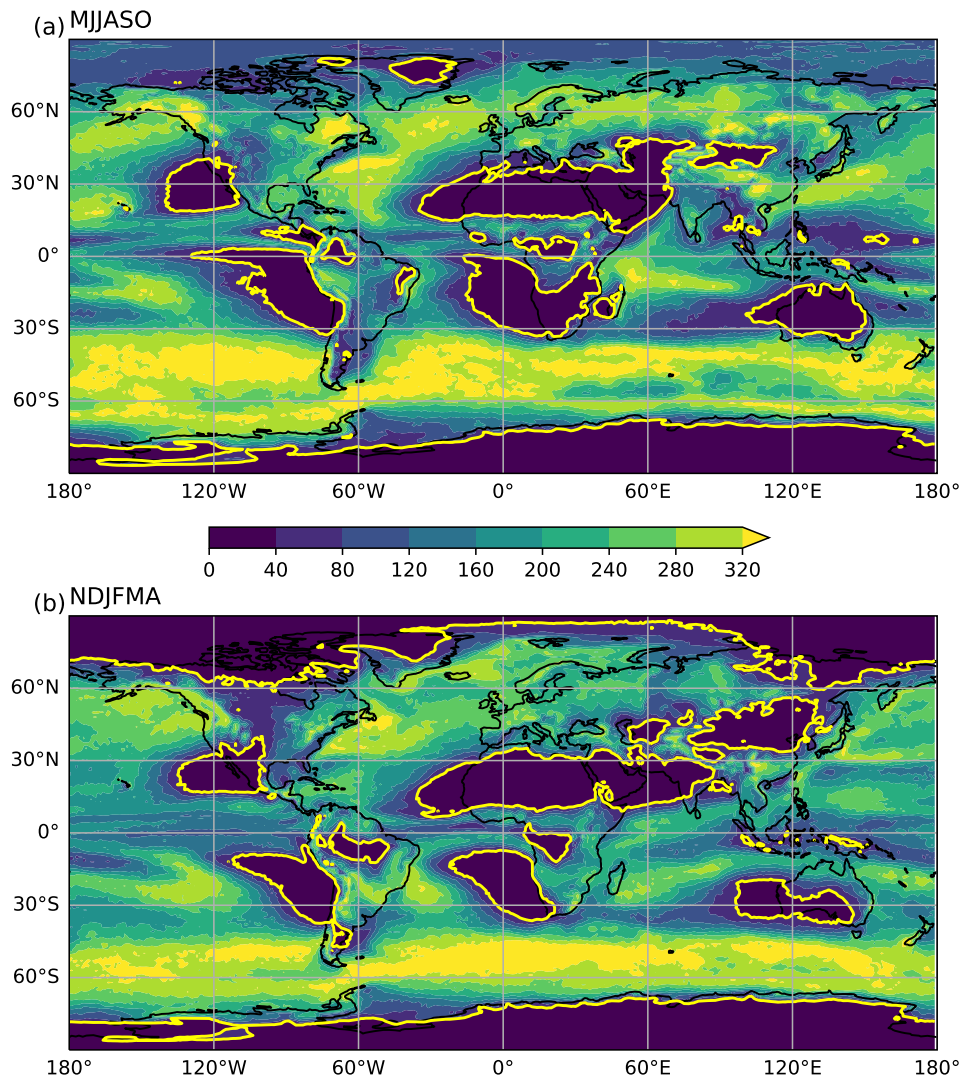


Figure A.3: Same as in figure A.1 except for MJJASO and NDJFMA wet spells.

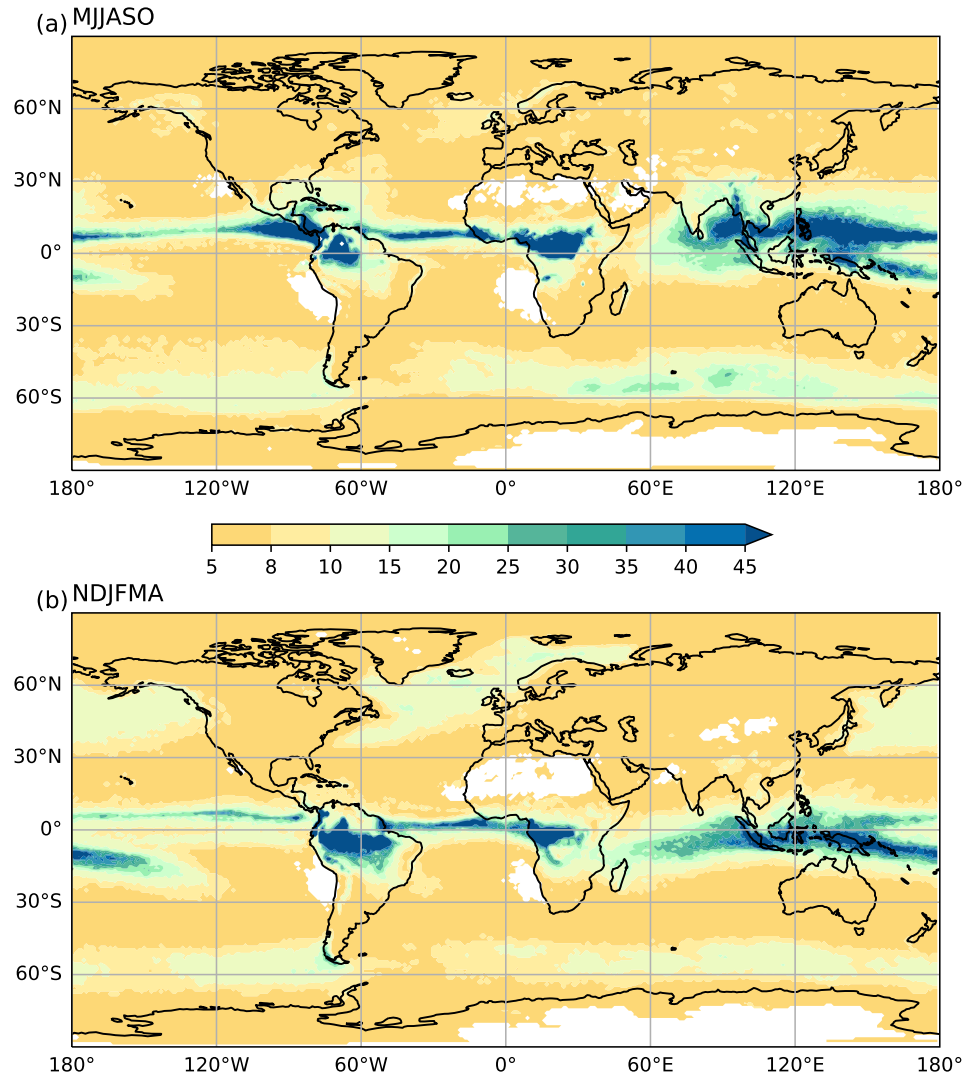


Figure A.4: Same as in figure A.2 except for MJJASO and NDJFMA wet spells.

## A.2 Additional examples of RRWPs and persistent dry and wet spells

### A.2.1 A dry spell in North America

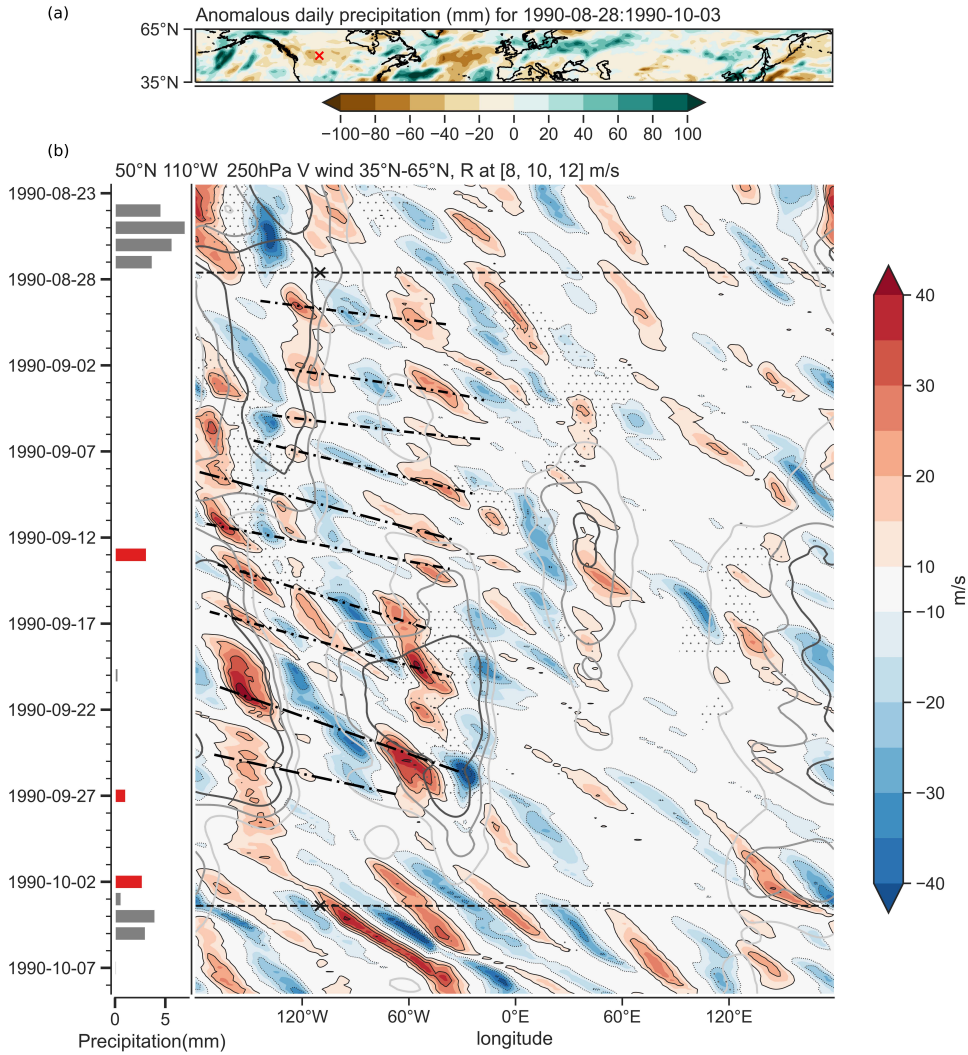


Figure A.5: Dry spell during Aug-Sept 1990 over Canada and Northern US (a) Anomalous daily precipitation (mm) compared to ERA-I climatology (1979-2018) for the same period. (b) Bars show aggregated daily precipitation at location ‘x’ (50°N, 110°W) in (a), red when precipitation is in the spell period and above 1 mm threshold, else grey. The Hovmöller diagram in (b) shows 35°N-65°N averaged meridional wind at 250 hPa. Black dotted lines in (b) mark the onset and end of the spell at ‘x’ in (a). Grey contours show R values of 8, 10, 12 ms<sup>-1</sup>. Stipplings depicts longitudes at which at least one grid point 20°N-70°N featured an atmospheric block while the dash-dotted lines indicate the approximate longitude-time trajectory of the Rossby wave packets (i.e., group propagation).

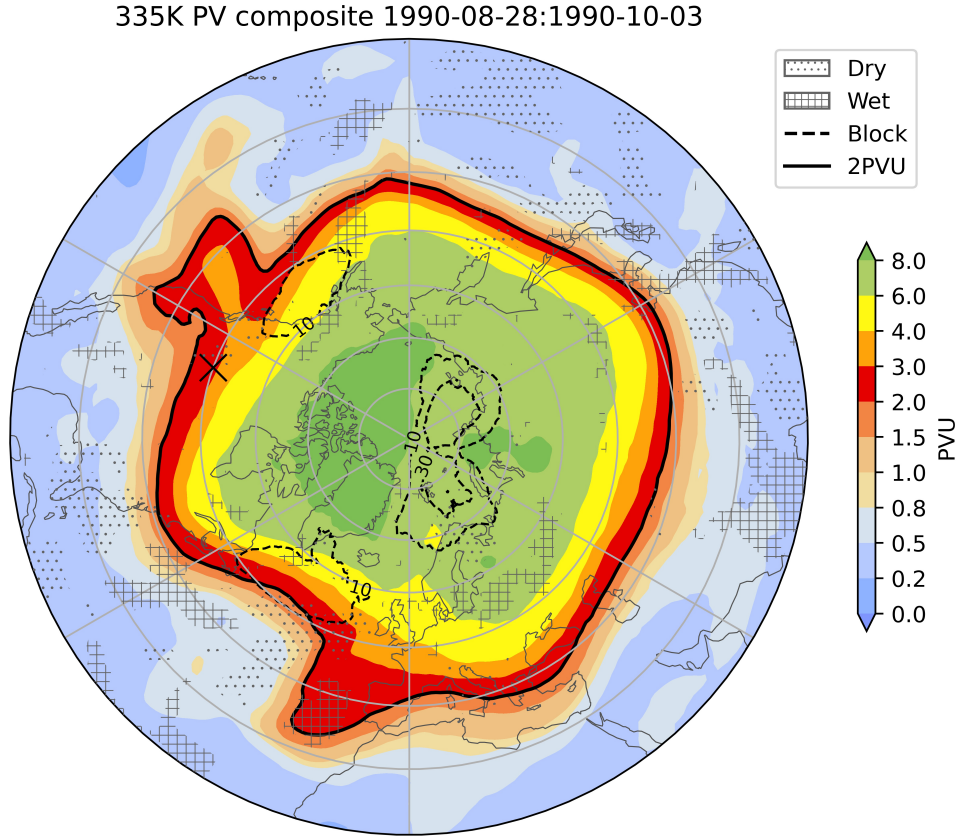


Figure A.6: PV at 335 K isentropes averaged for the spell duration in figure A.5. Dashed contours indicate blocking frequency in %. Daily precipitation anomalies aggregated for the spell duration which exceed  $\pm 40$  mm are indicated by the corresponding hatches (see legend).

A 37-day long dry spell started on 28 August 1990 at 50°N 110°W, Canada. During the first 2-weeks high  $R$  values are present over and around 110°W, where several trough-ridge couplets amplify recurrently as shown in Figure A.5. Noticeably, no blocking is directly present over this grid-point during the entire episode. There is also a consistent high  $R$  signal and recurrence of wave packets over the western Pacific Ocean as well as blocking. The PV composite (Figure A.6) for this episode shows a wave extending from the western Pacific over to the Atlantic and into Europe. The flow over Asia and eastern Pacific is rather zonal. The PV composite indicates anticyclonic wave breaking over the Gulf of Alaska. There are also several blocks present south of Alaska during this period as shown by the blocking frequency contours.

### A.2.2 A wet spell in South America

9 June 2006 marks the start of a 9-day long wet spell. The daily precipitation time series for 50°S and 55°W shows 9 consecutive days of precipitation. The Hovmöller diagram (Fig. A.7) shows recurrent troughs leading to anomalous rainfall over parts of southern Brazil and Uruguay. The PV composite for this period (Figure A.8) also shows a prominent trough over subtropical



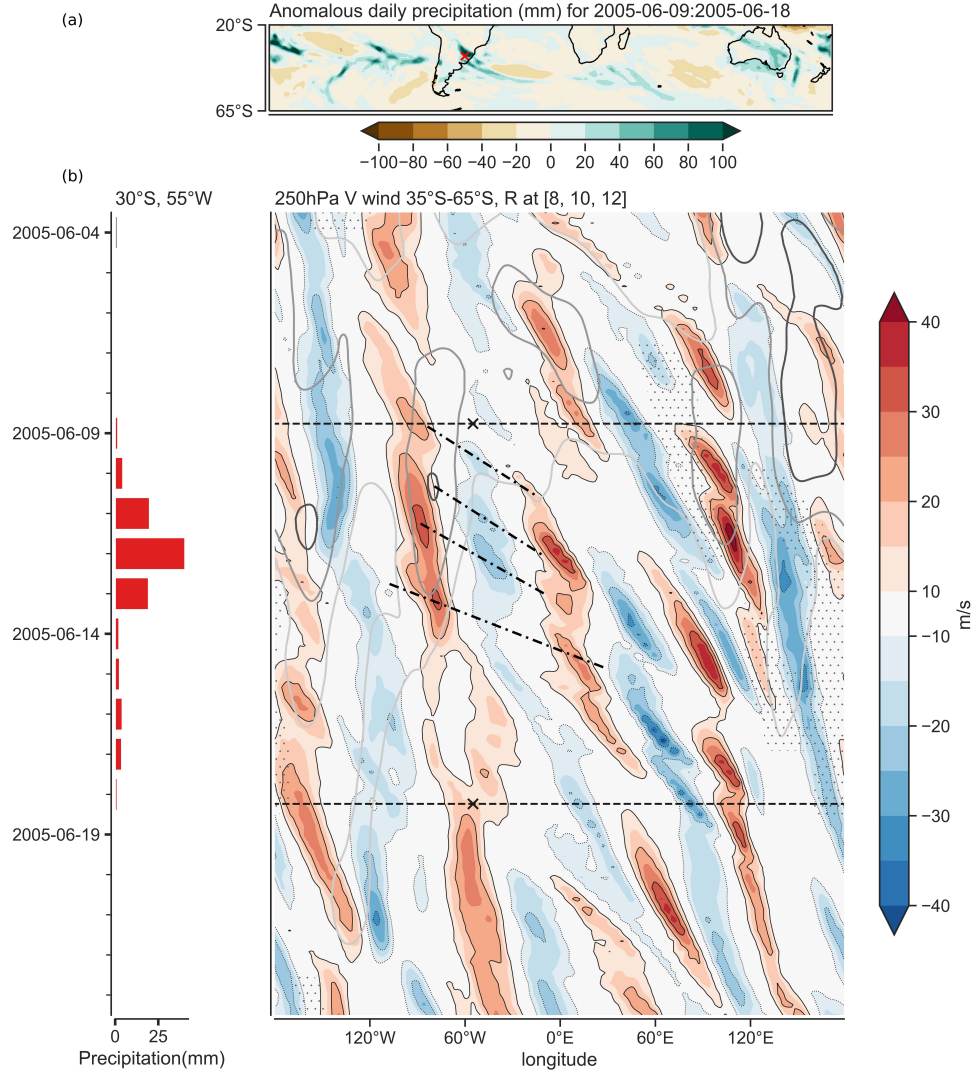


Figure A.7: Same as in figure A.5 but for a heavy precipitation event over Southern Brazil and Uruguay (30°S, 55°W) during June 2005. The Hovmöller diagram shows mean meridional wind at 250 hPa between 35°S-65°S in (b). Grey contours show R values at 8, 10, 12 m/s. Stipplings depicts longitudes at which at least one grid point 20°S-70°S featured an atmospheric block while the dash-dotted lines indicate the approximate longitude-time trajectory of the Rossby wave packets (i.e., group propagation).

South America. In the PV composite, wavenumber 5 structure is visible; however, the flow is considerably more zonal compared to the PV composite for the dry spell case over Iberia discussed in the main text (Fig. 2.4). There are also two blocks situated over Indian Ocean and Pacific Ocean during this period with the later block being present for around 60% of time during this event.

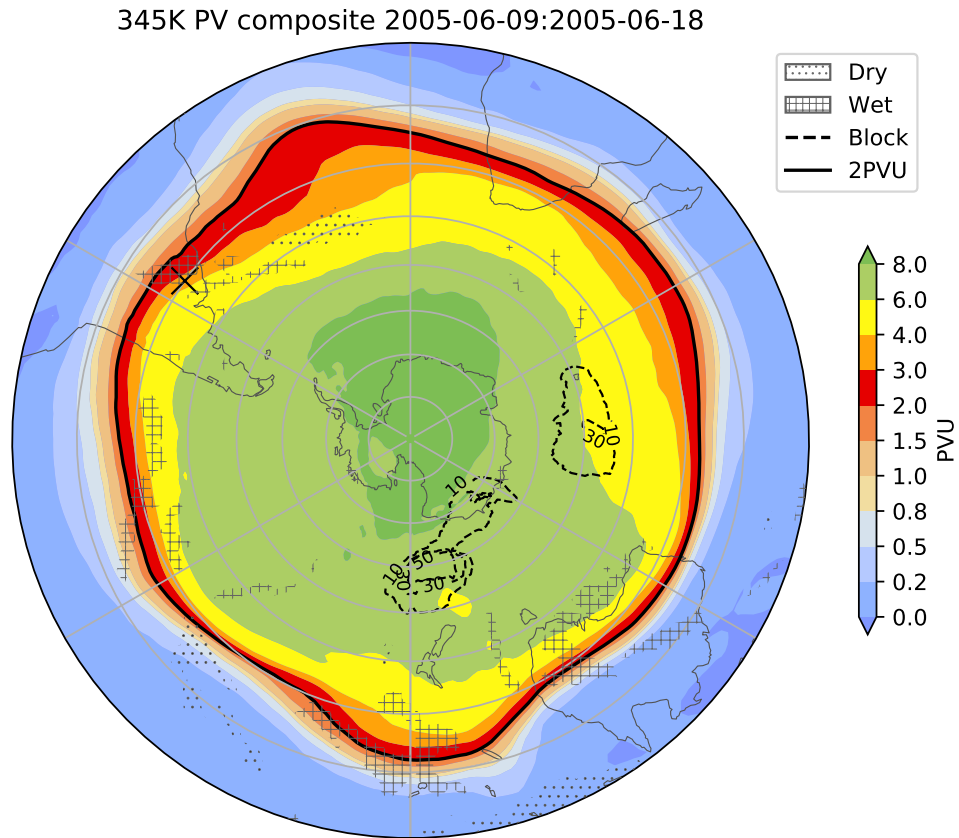


Figure A.8: PV at 345 K isentropes averaged for the duration of the wet spell shown in A.7 at the location “X”. Daily precipitation anomalies aggregated for the spell duration exceeding  $\pm 30$  mm are indicated by the corresponding hatches (see legend). Dashed contours show blocking frequency in % during this period.





## Appendix B

# Supporting Information for Recurrent Rossby waves and South-eastern Australian heatwaves

### B.1 Comparison of $R$ anomalies for Southern Hemisphere and Northern Hemisphere

Both the Southern and Northern Hemisphere  $R$  fields show seasonality (Fig. B.1). Anomalies are highest for Northern Hemisphere boreal autumn and winter days. Interestingly, the Southern Hemisphere shows higher  $R$  anomalies during austral summer days than winter days (Fig. B.1a).

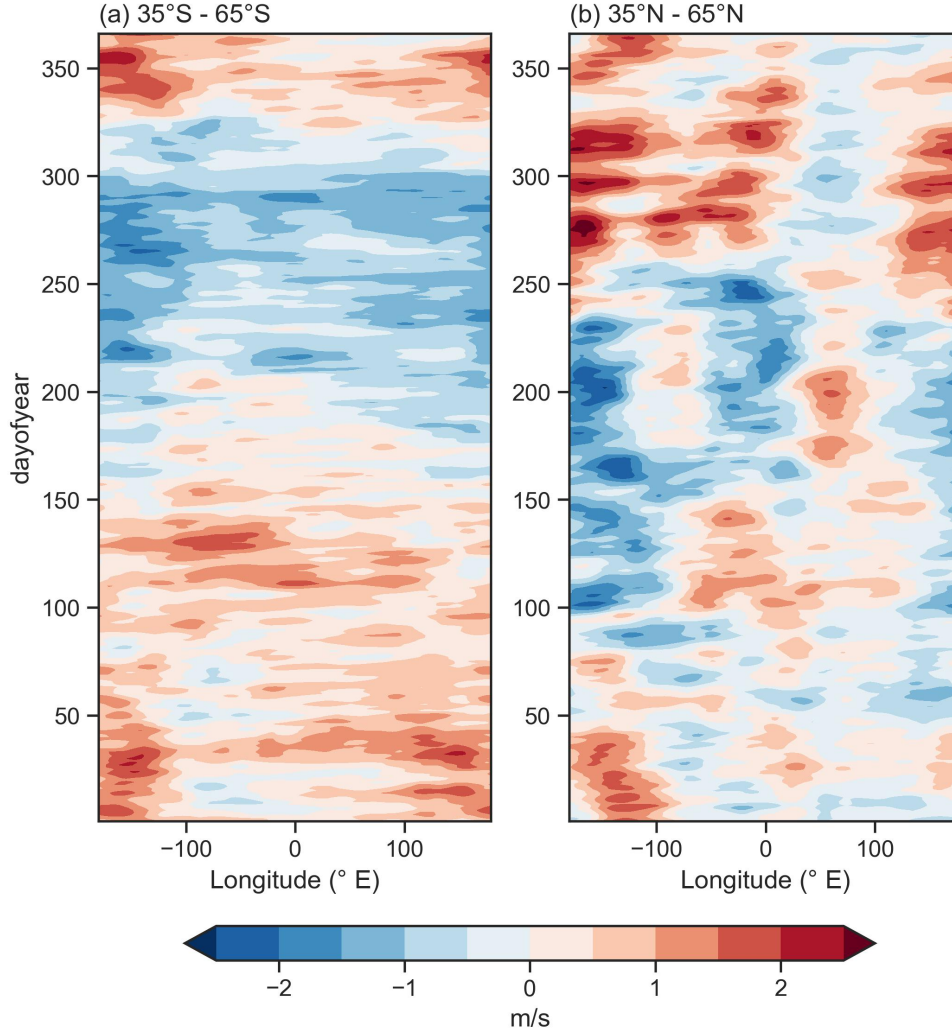


Figure B.1:  $R$  anomalies for Southern and Northern hemispheres. Anomalies for day-of-year mean at each longitude are calculated with respect to mean  $R$  fields for the year for NH and SH respectively.

## B.2 Co-occurrence of High $R_{SEA}$ on SEA heatwave days

Co-occurrence of High  $R_{SEA}$  with SEA heatwave days (SEA HW) as defined in Chapter 3.

*Table B.1: Co-occurrence of High  $R$  and QRA on SEA heatwave days (SEA HW) and the associated conditional probabilities of a heatwave given high  $R$  or a QRA day. Days column shows the probability of SEA HW in the climatology. QRA-all considers wavenumbers 4 to 6.*

	Days (DJF)	$R_{SEA}$
SEA HW days $R_{SEA}$	458	67
SEA non-HW Days $R$	3062	285
<b>Total</b>	3520	352
$P(\text{SEA HW} \mid R \text{ or QRA})$	$P_{HW} = 0.13$	0.19

### B.3 RRWPs during 2014 Heatwaves

Figure B.2 show RRWPs for the 2014 SEA heatwave. The heatwave started on 28 January and lasted till 14 February. A series of RRWPs are seen over SEA. Downstream in the Pacific, blocking is persistently present for the duration of the heatwaves with Rossby waves upstream and downstream of the block.

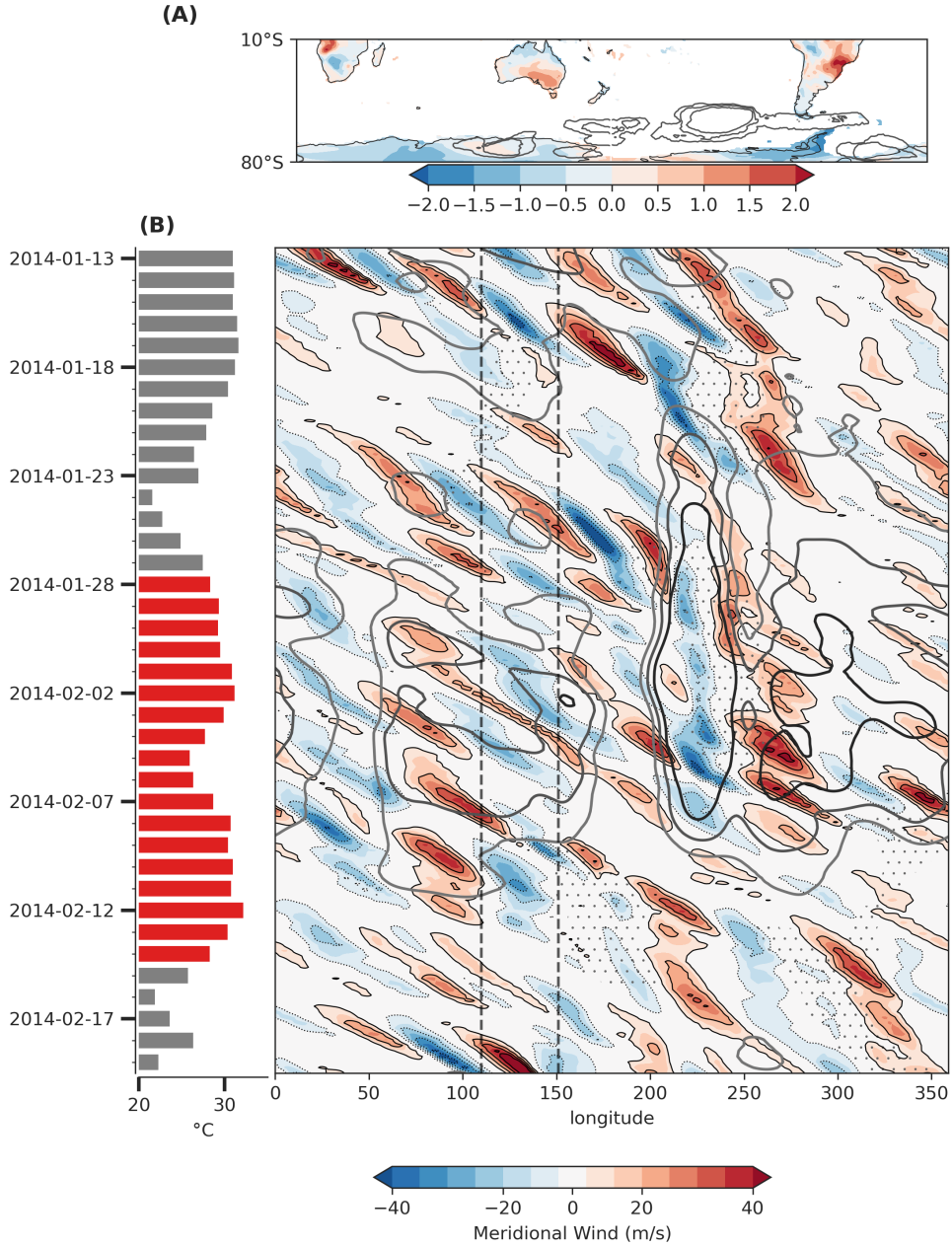


Figure B.2: Same as in Fig. 3.4 but for January 2014 SEA heatwave.

## B.4 Relationship between blocks and RRWPs in the south Pacific and the Indian Ocean

To further analyse the spatial distribution of RRWPs relative to blocks in the SH, we focus on two longitudinal subdomains that show a high blocking frequency in the DJF climatological mean: the South Pacific Ocean (230 – 310° E), and the Indian Ocean (0 – 90° E). We use time-lagged composite  $R$  anomalies with respect to the centroid of the blocks at the time of the maximum

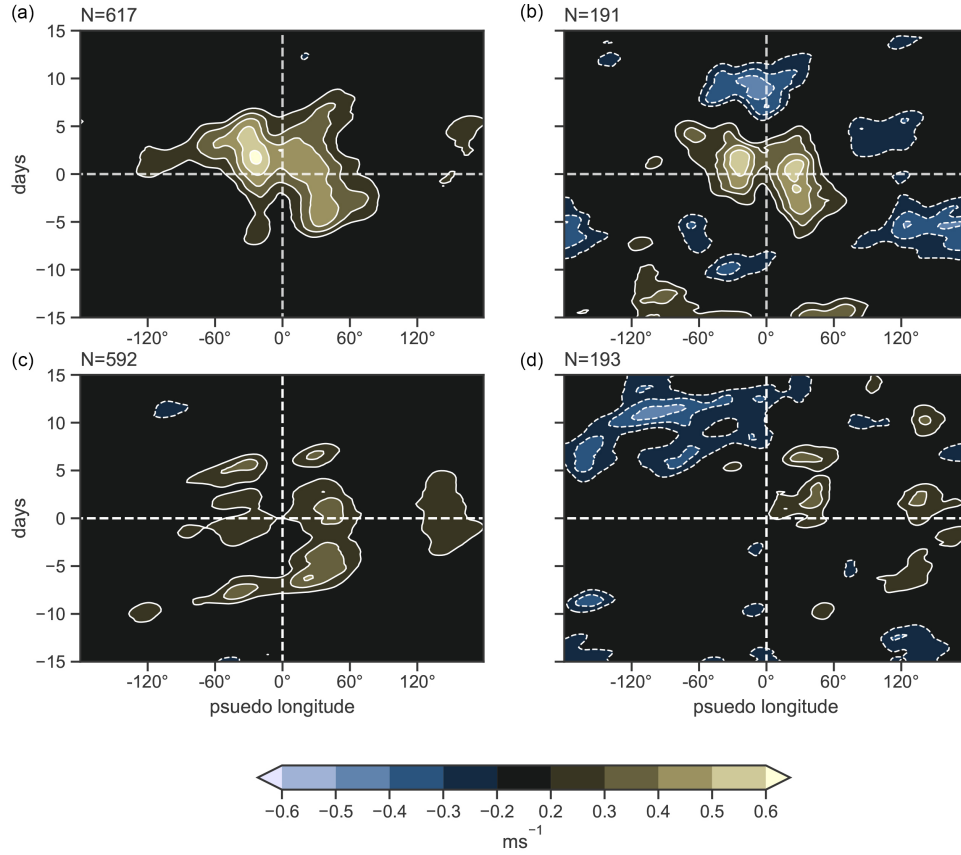


Figure B.3: Time-lagged Hovmöller composites of  $R$  anomalies centred on the mean longitude and time of maximum amplitude of blocks located in Pacific Ocean ( $181\text{--}300^\circ\text{E}$ ,  $30\text{--}80^\circ\text{S}$ ) in subplot (a) and (b), Indian Ocean ( $60\text{--}180^\circ\text{E}$ ,  $30\text{--}80^\circ\text{S}$ ) in subplot (c) and (d). Left column includes blocks for all seasons and right shows for DJF.  $N$  denotes number of blocks for each category.

blocking amplitude in the two domains similar to (see Fig. 12 in Röthlisberger et al., 2019). Here,  $R$  anomalies are calculated with respect to the day-of-year climatology.

In the Pacific Ocean, blocks coincide with positive  $R$  anomalies in a longitudinal band from  $60^\circ$  upstream to  $60^\circ$  downstream of the blocks (Fig. B.3 a, b) from 5 to 8 days before the time of maximum blocking amplitude; this resembles a butterfly pattern, similar to blocks in the NH (Fig. 12 in Röthlisberger et al., 2019). Similar to the NH,  $R$  anomalies in the Pacific Ocean are not high at the centroid of the block. This could be because the wavelength of the upper-level ridge associated with the block may be too wide to be captured by the  $R$ -metric because the  $R$ -metric only has contributions from  $k = 4$  and higher.  $R$  anomalies are consistent for DJF and blocks for all seasons in the Pacific. In contrast, in the Indian Ocean, seasonal variation is seen in  $R$  anomalies (Fig. B.3 c, d), where blocks located in DJF show  $R$  anomalies downstream of the centroid of the block only and possibly show weak association with RRWPs.



## Appendix C

# Additional Information for drivers of Recurrent Rossby Waves in the North Atlantic using Causal Networks

### C.1 Model Output DJF

Below, we show the model output of all the significant links for the main model ( $k=1$ ) shown in the results. Since we used 3-day time series, each time step denote a 3-day interval. Thus, R-NAt -1 implies link from R-NAt at a lag of 1 time step (3 days) to a variable. Below is a list of significant links for each variable displayed in Fig. 5.10:

Variable R-NAt has 3 link(s):

(R-NAt -1):  $pval = 0.00000$  —  $qval = 0.00000$  —  $val = 0.772$   
(R-NAt -2):  $pval = 0.00000$  —  $qval = 0.00000$  —  $val = -0.325$   
(Blocks-NAt -2):  $pval = 0.00236$  —  $qval = 0.00804$  —  $val = 0.089$

Variable Adv-Pac has 5 link(s):

(Adv-Pac -1):  $pval = 0.00000$  —  $qval = 0.00000$  —  $val = 0.914$   
(Adv-Pac -2):  $pval = 0.00000$  —  $qval = 0.00000$  —  $val = -0.782$   
(Adv-Pac -3):  $pval = 0.00000$  —  $qval = 0.00000$  —  $val = 0.655$   
(BU-Pac 0):  $pval = 0.00000$  —  $qval = 0.00000$  —  $val = 0.337$   
(BU-Pac -1):  $pval = 0.00000$  —  $qval = 0.00000$  —  $val = -0.144$

Variable BU-Pac has 7 link(s):

(BU-Pac -1): pval = 0.00000 — qval = 0.00000 — val = 0.576  
(Adv-Pac -1): pval = 0.00000 — qval = 0.00000 — val = 0.438  
(Adv-Pac 0): pval = 0.00000 — qval = 0.00000 — val = 0.337  
(Adv-Pac -2): pval = 0.00000 — qval = 0.00000 — val = -0.329  
(BU-Pac -2): pval = 0.00000 — qval = 0.00000 — val = -0.218  
(Adv-Pac -3): pval = 0.00000 — qval = 0.00000 — val = -0.199  
(BU-Pac -3): pval = 0.00000 — qval = 0.00001 — val = 0.141

Variable BU-NAt has 6 link(s):

(BU-NAt -1): pval = 0.00000 — qval = 0.00000 — val = 0.678  
(Blocks-NAt 0): pval = 0.00000 — qval = 0.00000 — val = -0.442  
(BU-NAt -2): pval = 0.00000 — qval = 0.00000 — val = -0.231  
(R-NAt -3): pval = 0.00001 — qval = 0.00006 — val = 0.127  
(R-NAt -1): pval = 0.00009 — qval = 0.00032 — val = -0.115  
(BU-Pac -2): pval = 0.00036 — qval = 0.00129 — val = -0.105

Variable Blocks-NAt has 7 link(s):

(Blocks-NAt -1): pval = 0.00000 — qval = 0.00000 — val = 0.476  
(BU-NAt 0): pval = 0.00000 — qval = 0.00000 — val = -0.442  
(Blocks-NAt -2): pval = 0.00000 — qval = 0.00000 — val = -0.197  
(BU-NAt -1): pval = 0.00000 — qval = 0.00000 — val = -0.175  
(R-NAt -1): pval = 0.00002 — qval = 0.00008 — val = 0.125  
(BU-NAt -2): pval = 0.00262 — qval = 0.00855 — val = 0.088  
(R-NAt -3): pval = 0.01574 — qval = 0.04918 — val = -0.071



## C.2 Model Output JJA

As in Appendix C.1 but for the CN for JJA shown in Fig. 5.14.

Variable R-NAt has 7 link(s):

(R-NAt -1): pval = 0.00000 — qval = 0.00000 — val = 0.780  
 (R-NAt -2): pval = 0.00000 — qval = 0.00000 — val = -0.352  
 (R-NAt -3): pval = 0.00022 — qval = 0.00161 — val = 0.108  
 (R-NAt -4): pval = 0.00029 — qval = 0.00196 — val = -0.106  
 (BU-NAt -3): pval = 0.00098 — qval = 0.00606 — val = 0.097  
 (Blocks-NAt -1): pval = 0.00138 — qval = 0.00787 — val = 0.094  
 (BU-EPac -1): pval = 0.00319 — qval = 0.01701 — val = 0.086

Variable BU-EPac has 4 link(s):

(BU-EPac -1): pval = 0.00000 — qval = 0.00000 — val = 0.605  
 (BU-EPac -2): pval = 0.00000 — qval = 0.00000 — val = -0.240  
 (BU-EPac -3): pval = 0.00011 — qval = 0.00091 — val = 0.113  
 (BU-NAt -2): pval = 0.00499 — qval = 0.02493 — val = 0.082

Variable BU-NAt has 3 link(s):

(BU-NAt -1): pval = 0.00000 — qval = 0.00000 — val = 0.652  
 (Blocks-NAt 0): pval = 0.00000 — qval = 0.00000 — val = -0.414  
 (BU-NAt -2): pval = 0.00000 — qval = 0.00000 — val = -0.197

Variable Blocks-NAt has 5 link(s):

(BU-NAt 0): pval = 0.00000 — qval = 0.00000 — val = -0.414  
 (Blocks-NAt -1): pval = 0.00000 — qval = 0.00000 — val = 0.358  
 (BU-NAt -1): pval = 0.00000 — qval = 0.00000 — val = -0.197  
 (Blocks-NAt -2): pval = 0.00000 — qval = 0.00001 — val = -0.140  
 (R-NAt -1): pval = 0.00783 — qval = 0.03684 — val = 0.078

## C.3 Sensitivity tests for DJF

Table C.1 shows the output of the main model showed in results for DJF. Table C.2 and Table C.3 show the outputs of the other two models used for the significant tests. The tables show only the significant drivers of R-NAt.

Table C.1: Drivers of R-NAt from the main model ( $k=1$ ) for DJF

<i>Actor</i>	<i>p</i>	<i>q</i>	<i>strength</i>
R-NAt, t=-3	0.00000	0.00000	0.772
R-NAt, t=-6	0.00000	0.00000	-0.325
Blocks-NAt, t=-6	0.00236	0.00804	0.089

Table C.2: Drivers of R-NAt from the model  $k=0$  for DJF

<i>Actor</i>	<i>pvalue</i>	<i>qvalue</i>	<i>strength</i>
R-NAt, t=-3	0.00000	0.00000	0.777
R-NAt, t=-6	0.00000	0.00000	-0.335
Blocks-NAt, t=-6	0.00078	0.00279	0.098
BU-NAt, t=-9	0.00323	0.01055	0.086

Table C.3: Drivers of R-NAt from the model  $k=1$  for DJF

<i>Actor</i>	<i>p - value</i>	<i>q - value</i>	<i>strength</i>
R-NAt, t=-3	0.00000	0.00000	0.774
R-NAt, t=-6	0.00000	0.00000	-0.316
Blocks-NAt, t=-6	0.00523	0.01510	0.082

## C.4 Sensitivity tests for JJA

Table C.4 shows the output of the main model showed in results for JJA. Table C.5 and Table C.6 show the outputs of the other two models used for the significant tests. The tables show only the significant drivers of R-NAt.

Table C.4: Drivers of R-NAt from the main model ( $k=1$ ) for JJA

<i>Actor</i>	<i>p – value</i>	<i>q – value</i>	<i>strength</i>
R-NAt, t=-3	0.00000	0.00000	0.780
R-NAt, t=-6	0.00000	0.00000	-0.352
R-NAt, t=-9	0.00022	0.00161	0.108
R-NAt, t=-12	0.00029	0.00196	-0.106
BU-NAt, t=-9	0.00098	0.00606	0.097
Blocks-NAt, t=-3	0.00138	0.00787	0.094
BU-EPac, t=-3	0.00319	0.01707	0.086

Table C.5: Drivers of R-NAt from the model  $k=0$  for JJA

<i>Actor</i>	<i>p – value</i>	<i>q – value</i>	<i>strength</i>
R-NAt, t=-3	0.00000	0.00000	0.777
R-NAt, t=-6	0.00000	0.00000	-0.352
BU-At, t=-9	0.00010	0.00074	0.114
R-NAt, t=-9	0.00133	0.00888	0.094
Blocks-NAt t=-3	0.00865	0.04312	-0.077
BU-EPac t=0	0.01954	0.01954	0.068
Blocks-NAt t=0	0.03866	0.03866	0.061

Table C.6: Drivers of R-NAt from the model  $k=2$  for JJA

<i>Actor</i>	<i>p – value</i>	<i>q – value</i>	<i>strength</i>
R-NAt, t=-3	0.00000	0.00000	0.782
R-NAt, t=-6	0.00000	0.00000	-0.357
BU-At, t=-9	0.00058	0.00399	0.101
R-NAt, t=-9	0.00060	0.00399	0.101
R-NAt, t=-4	0.00247	0.01518	-0.089
Blocks-NAt, t=-3	0.00711	0.03260	0.079
BU-EPac, t=-3	0.00734	0.03260	0.079



## Appendix D

# A novel method to identify sub-seasonal clustering episodes of extreme precipitation events and their contributions to large accumulation periods

This chapter contains the abstract of the article – "A novel method to identify sub-seasonal clustering episodes of extreme precipitation events and their contributions to large accumulation periods". It is published in the journal *Hydrology and earth system sciences* and citable as Kopp et al. (2021). It is authored by Jérôme Kopp, Pauline Rivoire, S. Mubashshir Ali, Yannick Barton, and Olivia Martius. I co-supervised the masters' thesis of Jérôme Kopp, and contributed in the discussion of the results and in reviewing the draft.

## D.1 Abstract

Temporal (serial) clustering of extreme precipitation events on sub-seasonal time scales is a type of compound event. It can cause large precipitation accumulations and lead to floods. We present a novel, count-based procedure to identify episodes of sub-seasonal clustering of extreme precipitation. We introduce two metrics to characterise the frequency of sub-seasonal clustering episodes and their relevance for large precipitation accumulations. The procedure does not require the investigated variable (here precipitation) to satisfy any specific statistical properties. Applying this procedure to daily precipitation from the ERA5 reanalysis data set, we identify regions where sub-seasonal clustering occurs frequently and contributes substantially to large precipitation accumulations. The regions are the east and northeast of the Asian continent (north of Yellow Sea, in the Chinese provinces of Hebei, Jilin and Liaoning; North and South Korea; Siberia and east of Mongolia), central Canada and south of California, Afghanistan, Pakistan, the southwest of the Iberian Peninsula, and the north of Argentina and south of Bolivia. Our method is robust with respect to the parameters used to define the extreme events (the percentile threshold and the run length) and the length of the sub-seasonal time window (here 2 – 4 weeks). This procedure could also be used to identify temporal clustering of other variables (e.g. heat waves) and can be applied on different time scales (sub-seasonal to decadal). The code is available at the listed GitHub repository.

## Appendix E

# Large-scale drivers of persistent extreme weather during early summer 2021 in Europe

This chapter contains the abstract of the article currently in review at the journal – Geophysical Research Letters. It is authored by Alexander Tuel, Daniel Steinfeld, S. Mubashshir Ali, Michael Sprenger, and Olivia Martius. I contributed in the analysis, the discussion of results, and in reviewing the draft.

## E.1 Abstract

The early summer of 2021 was a season of extremes across Europe. Heatwaves, droughts and wildfires hit Eastern Europe and the Baltic, while repeated extreme precipitation in Western Europe culminated in massive floods in mid-July. The large-scale circulation during this period was remarkably persistent, with an extremely meridionally amplified flow over Europe. Recurrent blocking over the Baltic and Rossby wave breaking in the North Atlantic led to frequent heavy precipitation in Western Europe and the Black Sea and to warm and dry conditions over Eastern Europe. These conditions persisted for a month as the blocks and wave breaking episodes strengthened one another, while three closely-spaced extratropical transitions of tropical cyclones in the eastern North Atlantic led to recurrent amplification of the jet. Seasonal anomalies thus emerge from the complex interactions of individual weather events, offering an interesting storyline for climate impact assessment and a formidable challenge for (sub-) seasonal prediction.



## Appendix F

# On the temporal clustering of European extreme precipitation events and its relationship to persistent and transient large-scale atmospheric drivers

This chapter contains the abstract of the article – ”On the temporal clustering of European extreme precipitation events and its relationship to persistent and transient large-scale atmospheric drivers”. It is under review at the time of writing the thesis (Barton et al., 2022). It is authored by Yannick Barton, Jonathan Koh, Pauline Rivoire, S. Mubashshir Ali, Jérôme Kopp, and Olivia Martius. I contributed in the discussion of the results and in reviewing the draft.

## F.1 Abstract

Extreme precipitation events that occur in close succession can have important societal and economic repercussions. Here we use 42 years of reanalysis data (ERA-5) to investigate the link between Euro-Atlantic large-scale pattern of weather and climate variability and the temporal clustering of extreme rainfall events over Europe. We implicitly model the seasonal rate of extreme occurrences as part of a Poisson General Additive Model (GAM) using cyclic regression cubic splines. The smoothed seasonal rate of extreme rainfall occurrences is used to (i) infer the frequency of significant temporal clustering and (ii) implicitly serves as the baseline rate when modeling the effects of atmospheric drivers on extreme rainfall clustering. We use GAMs to model the association between the temporal clustering of extreme rainfall events and seven predominant year-round weather regimes in the Euro-Atlantic sector as well as a measure of synoptic-scale transient recurrent Rossby wave packets. Significant 21-day clustering episodes are found in all grid-points over Europe; the proportion of extreme rainfall events that cluster in time range between 2% to 27%. The most relevant weather regime is the Atlantic Trough (corresponding to the NAO+ with a southward shift of the jet) explaining most of the significant increase in clustering probability over Europe. The Greenland Blocking regime explains most of the clustering over the Iberian Peninsula. The Scandinavian Blocking regime is associated with a significant increase in clustering probability over the western Mediterranean, with a northwards shift in the signal to central Europe in summer.

## Acknowledgements

I want to acknowledge the Swiss National Science Foundation grant number 178751 for making this research possible. I express my deepest gratitude to Prof. Olivia Romppainen-Martius for not only guiding me throughout the thesis but also showing immense empathy and support. Many thanks to Dr. Matthias Röthlisberger for mentoring me throughout this thesis. I thank you for being supportive right from my first day at the institute, and I really enjoyed discussions with you on large-scale dynamics.

My sincere gratitude goes to Prof. John Methven for advising me, hosting me at Reading, spending your valuable time, and for the stimulating discussions throughout my thesis. I would also like to thank Dr. Kai Kornhuber and Dr. Tess Parker for their collaborations. I would also like to acknowledge Dr. Rachel White for evaluating my thesis and Prof. Dr. Stefan Brönnimann for agreeing to chair my defense.

I want to thank all my wonderful colleagues at work for creating a supportive environment, the numerous fruitful discussions over the coffee, and the refreshing activities we did outside of work. Pauline and Noemi, many thanks for creating a wonderful office atmosphere. Special thanks to Alexandre for the stimulating discussions and to the IT-team, Ralf and Eric for making my job easier.

I want to thank all my teachers who nurtured me throughout my life. Tarique bhai, many thanks for guiding me and encouraging me to pursue a PhD. Special thanks to my parents and my brother for all the sacrifices you did for me and for always being by my side.

Lastly, I want to acknowledge the open-source Python packages (Xarray, Numpy, Matplotlib) and the open-access data sources (ERA-5 and ERA-I) that helped immensely in the study. Many thanks to the stackoverflow community for solving the numerous coding problems.



# Declaration

under Art. 28 Para. 2 RSL 05

Last, first name: Ali, Syed Mubashshir

Matriculation number: 18-125-906

Program: PhD. in Climate Sciences

Bachelor ☐ Master ☐ Dissertation ☒

Thesis title: Recurrent Rossby waves: drivers and links to persistent weather

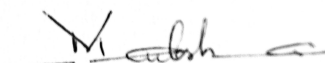
Thesis supervisors: Prof. Dr. Olivia Romppainen-Martius

Prof. Dr. John Methven

Dr. Matthias Röthlisberger

I hereby declare that this submission is my own work and that, to the best of my knowledge and belief, it contains no material previously published or written by another person, except where due acknowledgement has been made in the text. In accordance with academic rules and ethical conduct, I have fully cited and referenced all material and results that are not original to this work. I am well aware of the fact that, on the basis of Article 36 Paragraph 1 Letter o of the University Law of 5 September 1996, the Senate is entitled to deny the title awarded on the basis of this work if proven otherwise.

Bern, July 11, 2022



Signature